

---

*Investigative Analysis of Water Removal  
from Green-Shell Mussels*

---

Theo Martin Joseph Palmer  
Department of Chemical and Process Engineering  
University of Canterbury  
Christchurch, New Zealand



## Acknowledgements

I would firstly like to thank and thank David Aitchison and Robert Stack for instigating and allowing me the opportunity to undertake this project. David has spent large amounts of his time to help and support me throughout this work. He helped me diagnose issues with my experimental rigs as well as offering practical solutions to my theoretical problems. Your help has not gone unnoticed and is greatly appreciated.

Robert has been a great mentor and manager to me during my time at MacLab. Thank you for your patience during this work and allowing me the resources that I needed to complete this work. I would secondly like to thank the Board at MacLab for their financial and general support of Research and Development projects at MacLab. I would also like to give my parents a quick mention to acknowledge their never-ending support through my different levels of education, their support gives me the courage to try new things however difficult they may seem.

Lastly, I would like to thank Luke Schneider for taking me on as one of his students and putting up with my endless questions throughout this journey. It has been a long ride, but I got there in the end thanks to these key people.

## Abstract

An investigation was undertaken by Maclab to evaluate different methods of water removal from the process line. The areas that were chosen to be focused on were pre- and post-homogenization of the mussels and were required to not affect oil content. A centrifugal de-watering system was chosen for the pre-homogenization area. The pressure at which the pores between the mussels closed and water flow out of the bed reduced was found to be  $80 \text{ kPa} \pm 5 \text{ kPa}$ , which equated to a force of 13 kN. A centrifuge was designed based on the pressure at which the pores between the mussels closed and a load capacity of 15 kgs of mussels. The height, diameter, and angular velocity that best fit this problem were 0.58 m, 0.25 m, and  $20 \text{ rad s}^{-1}$  respectively. The designed centrifuge could not be constructed and tested due to budget constraints, this meant that the water removal rate had to be estimated. Using a water removal efficiency of 100% the water removal rate for this method was  $18.75 \text{ kg h}^{-1}$ . It was assumed that the designed centrifuge would not remove any of the valuable mussel oil from the whole mussels as the cellular structure of the mussel should be intact after centrifugation.

The application of a super absorbent polymer (SAP) underneath the liquid macerate during the freezing process was investigated as the post-homogenization process solution. For the SAP addition it was important that the SAP did not inhibit the freezing process in any way. A model was created to predict the temperature within the macerate over time. This model showed that the heat transfer rate through the bottom of the macerate was the slowest. This implied that the SAP needed to be added the bottom of the macerate. The new interfacial temperature profiles were re-measured, with the SAP on the bottom of the macerate. The results of this secondary experimentation showed that the addition of the SAP to the bottom of the macerate increased the time taken for the frozen front to reach the center by 14%. The water removal rate was found gravimetrically by weighing the SAP before and after the freezing process. It was calculated that the SAP method could remove  $66.92 \text{ kg h}^{-1}$  of water. External testing from Cawthron showed that there was no significant difference between the SAP and non-SAP treated macerate.

## Contents

Acknowledgements.....	ii
Abstract.....	iii
Chapter 1 Introduction .....	1
1.1 Background .....	1
1.2 Mussel Anatomy .....	2
1.3 Mussel Oil.....	3
1.3.1 Mussel Oil Classes .....	4
1.3.2 Study Site .....	6
1.4 Project.....	7
1.4.1 Aim .....	8
1.4.2 Constraints .....	8
Chapter 2 Alternate Water Removal Strategies .....	9
2.1 Pre-Homogenization Solutions .....	9
2.1.1 Pneumatic Systems .....	9
2.1.2 Centrifugation .....	10
2.1.3 Absorption.....	11
2.1.4 Pre-Homogenization Conclusions .....	12
2.2 Post Homogenization Solutions.....	13
2.2.1 Evaporation.....	13
2.2.2 Absorption.....	14
2.2.3 Osmosis .....	16
2.2.4 Liquid-liquid Extraction .....	17
2.2.5 Post-Homogenization Conclusions .....	17
2.3 Removal Methods Summary.....	18
Chapter 3 Theory .....	20
3.1 Centrifugation Model.....	20
3.1.1 Centrifuge Design.....	20
3.1.2 Shell Material Balance for Centrifuge .....	21
3.1.3 General Centrifuge Model .....	22
3.1.4 Dry Bed Centrifuge Model .....	25
3.1.5 Static Bed Background .....	26
3.1.6 Static Bed Model .....	26

3.2 Post-Homogenization Model .....	27
3.2.1 Post Homogenization Background.....	27
3.2.2 Convective Heat Transfer Background.....	28
3.2.3 Convective Heat Transfer Background.....	30
3.2.4 Steady-State Heat Transfer Model without Absorbent Pad .....	30
3.2.5 Steady-State Heat Transfer Model with Absorbent Pad.....	32
3.2.6 Dynamic Mathematical Heat Transfer Solution.....	33
3.2.7 Dynamic Mathematical Heat Transfer Solution (Bottom) .....	34
3.2.8 Frozen Front Propagation .....	35
Chapter 4 Materials and Methods.....	36
4.1 Pre-Homogenization Experimentation .....	36
4.1.1 Static Bed Experimental Procedure .....	38
4.2 Post-Homogenization Experimental Design .....	39
4.2.1 Transient Temperature of the Macerate .....	40
4.2.2 Fitting the Transient Model to Obtain $k$ .....	41
4.2.3 SAP Choice.....	41
4.2.4 Effect of the SAP on Cooling and Freezing.....	42
4.2.5 Water Removal by the SAP .....	42
4.2.6 Oil Removal by the SAP .....	43
Chapter 5 Experimental Results.....	44
5.1 Centrifuge Design.....	44
5.1.1 Maximum Pressure Drop (MAP) and Lumped Drag Coefficient Determination ( $CD'$ ) .....	44
5.1.2 Preliminary Results .....	44
5.1.3 Centrifuge Design Optimization.....	51
5.1.4 Angular Velocity Determination (Dry Bed) .....	54
5.2 Post-Homogenization SAP Results .....	55
5.2.1 Thermal Profile of the Macerate.....	56
5.2.2 Determination of the Macerate Thermal Conductivity Without SAP .....	58
5.2.3 Thermal Profile with an Absorbent Pad.....	61
5.2.4 Modelled Thermal Profile with an Absorbent Pad .....	64
Chapter 6 Discussion.....	67
6.1 Pre-Homogenization Results.....	67
6.1.1 Static Pressure Vessel Testing.....	67

6.1.2 Centrifugal Solutions .....	69
6.2 Post-Homogenization Results .....	70
6.2.1 Existing Thermal Profiles .....	70
6.2.2 Thermodynamic Modelling .....	71
6.2.3 Empirical Absorbent Pad Thermal Profiles .....	72
6.2.1 Mass Change of the Absorbent Pad .....	73
6.2.2 Absorbent Pad Thermal Modelling .....	73
Chapter 7 Conclusions and Recommendations .....	75
7.1 Summary .....	75
7.2 Pre-Homogenization .....	75
7.3 Post-Homogenization .....	77
7.4 Method Comparison .....	79
Chapter 8 Bibliography .....	81
Appendix .....	85
8.1 Static Pressure Vessel .....	85
8.1.1 Equipment List .....	85
8.1.2 Raw Data .....	85
8.1.3 Record Sheet Template .....	85
8.1.4 MATLAB Code Used in Centrifuge Design .....	85
8.1.5 Code Used Centrifuge Solutions .....	86
8.2 Absorbent Pad .....	88
8.2.1 Preliminary Testing (Capillary Action Significance) .....	88
8.2.2 Record Sheet Template .....	88
8.3 Auxiliary Probe Support Designs .....	88
8.4 Numerical Integration Method for Current Thermodynamic Layout .....	92
8.4.2 MATLAB Code Used to Solve Current Dimensioned Numerical Integration .....	92
8.4.3 MATLAB Code Used to Solve Padded Dimensioned Numerical Integration .....	100

This page has intentionally been left blank.

## Chapter 1 Introduction

This thesis is aimed at investigating the possible removal of water from the primary product stream within a mussel processing factory. The water removal area will be located after the shucking process and prior to the freeze-drying process. This processing factory specializes in the production of the creation of the green shelled mussel (GSM) powder that is then used for nutraceutical products. This GSM powder is also subsequently extracted to produce the inflammatory suppression supplement known as mussel oil. This GSM powder is the primary constituent of the main product stream at the processing facility known as MacLab.

### 1.1 Background

*Perna canaliculus*, also known as GSMs or green lipped mussels, have been industrially farmed since the late 1960's. These shellfish feed off smaller micro-organisms such as phytoplankton and zooplankton. Due to their filter feeding nature, GSMs are highly susceptible to environmental effects. This dependency on the environment means that different seasons and growing areas will produce a different quantity and quality of mussels. Aquaculture production areas are spread across New Zealand with most of the farms being in either Marlborough (71%) or Coromandel (19%) (Fig. 1).

Major Aquaculture Areas in New Zealand

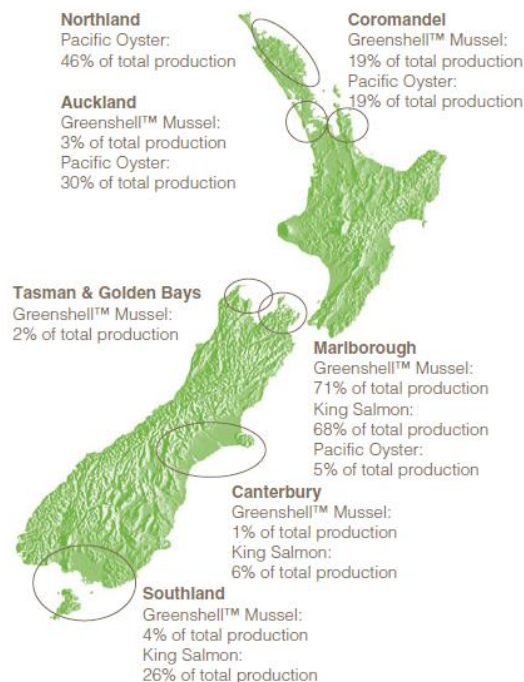


Figure 1 Location and Distribution of Green Shell Mussel Farms in NZ (Aquaculture New Zealand, 2010)

GSMs have a high long-chain polyunsaturated fatty acid (LC-PUFA) content, which is one of the major draws to mussel farming due to the health benefits associated with LC-PUFAs. GSM farms also produce mussels as food, in which the mussels come in the form of; half shell; crumbed; marinated; live; and canned. Another option is to dry the mussels and sell the powder as a dietary supplement. Mussel farming is a multi-million-dollar industry and has the ability to be farmed on large scale, therefore was recognized as a sustainable source of nutrition (Miller, Pearce, & Bettjeman, 2014). LC-PUFAs include some of the omega-3 fatty acid group, which are known to be beneficial to human health, especially in the treatment of inflammatory conditions. The health benefits that come from the omega-3 fatty acid group will be mentioned in Section 1.2.

The lipid content of a GSM can vary based on the size of the mussel, food availability, sea temperatures at time of harvest, and water velocities and therefore the wind velocities as they affect the ocean currents to a degree. GSM meat can range anywhere between 10 to 50 g per mussel (Robert Stack, Personal Communication, 2018). The mussel powder portion of the GSM industry can take mussels of all sizes. Whereas the half shell, crumbed, and other food sections prefer to take the mussels that fall in the middle of the size distribution as this is what is preferred by the consumers.

Studies, such as that of Matthew Miller et al, have tried to relate the lipid content of the mussel meat to the wet mass of mussel meat through a so called “Condition Index” (Miller, Pearce, & Bettjeman, 2014). This particular study correlated a higher lipid content for female mussels compared to that of male mussels. Even though the males and females have the same anatomy as described in the section below.

## 1.2 Mussel Anatomy

The GSM anatomy (Fig. 22) consists of a mantle, which excretes compounds used in shell production; the abductor muscle, which is used to keep the mussel attached to the shell and gives the mussel the ability to control the shell’s opening; digestive glands; gonad; and foot, which is used to maneuver the mussel through the external environment. Previous studies indicate that the lipid content from highest to lowest is, gonad, digestive gland, mantle, heart, and foot (Miller, Pearce, & Bettjeman, 2014).

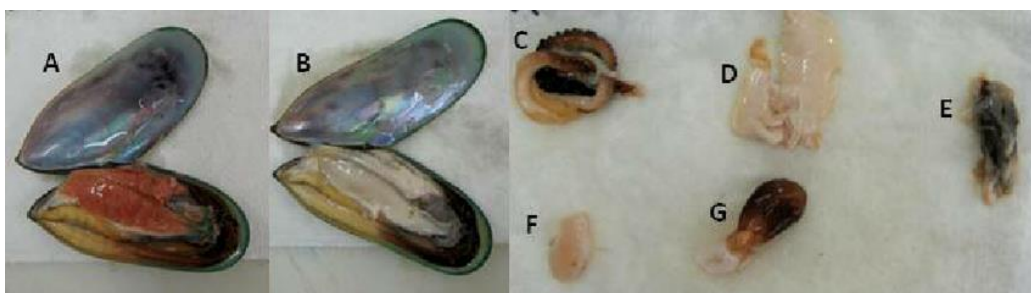


*Figure 2 GSM Anatomy: “(A) Female GSM with Orange Gonad; (B) Male GSM with Cream Colored Gonad; (C) Mantle; (D) Gonad; (E) Digestive Gland; (F) Posterior Adductor Muscle; (G) Heart and Foot” (Miller, Pearce, & Bettjeman, 2014)*

It has been noted by Miller et al, that the female GSM (exhibited by the bright orange gonad) contained a 0.5 % additional lipid content compared to that of male GSM (exhibited by a cream-colored gonad). This

lipid content needs to be extracted from the mussel and purified to produce the inflammatory suppression supplement known as mussel oil.

### 1.3 Mussel Oil

GSMs contain a unique lipid profile that, when concentrated, can have positive impacts on specific pathways in the human body. These extracted oils are packaged and sold, this product offers natural pain relief from inflammatory disorders (PharmacyDirect, 2018). The following section will give an understanding of the constituents of mussel oil and their effects.

There are two fatty acids, eicosapentaenoic acid (EPA) and docosahexaenoic acid (DHA), that are recognized as being key contributors to the health benefits associated with mussel oil (a collection of the neutral lipids). These two fatty acids are believed to have significant positive effects on the human lipoprotein content in the blood and act as a modifier for the high-density to low-density lipoprotein ratio (commonly denoted as HDL and LDL for high-density and low-density lipoprotein respectively) (Hermann Esterbauer, Quehenberger, & Koller, 2018). These two chemicals, EPA and DHA, are found in mussel oil and have been reported to modulate the 5-lipoxygenase metabolic pathway as well as the HDL to LDL ratio. The 5-lipoxygenase metabolic pathway is one of the major inflammatory pathways in the human body (Lyprinol, 2017). The second of these major metabolic pathways is the cyclooxygenase pathway. Both pathways produce unique bio-active compounds that contribute to medical conditions such as arthritis, asthma, and anaphylactic related conditions (Pallu Reddanna, et al., 1989). Mussel oil has been known to block the 5-lipoxygenase pathways therefore, inhibiting the production of Leukotrienes, which are specific to that of the 5-lipoxygenase pathway.

The mussel oil composition is verified by first extracting the total lipid content (TLC) from a homogenized solution of GSM meat, where homogenization is defined as the process of mincing the whole mussels. The TLC can be acquired by conducting a Bligh and Dyer type extraction (Breil, Vian, Zemb, Kunz, & Chemat, 2017) on the dried and powdered mussel, which is a solid-liquid-liquid type extraction. Once the TLC has been retrieved from the GSM powder the fatty acid profile (FAP) can be determined. This FAP informs the manufacturer as to the exact fatty acids composition (poly-, mono, and saturated fatty acids) that reside in the test solution and their proportionality (Table 1). Some of the different fatty acid classes that constitute mussel oil are described further in Section 1.3.1 .

*Table 1 Major Lipid Classes within Mussel Oil*

<b>Lipid Class</b>	<b>Major Constituent(s)</b>
Long Chain Fatty Acid	EPA/DHA
Short Chain Fatty Acid	SDA
Omega-3 Fatty Acid	EPA/DHA
Polyunsaturated Fatty Acid	EPA/DHA
Omega-6 Fatty Acid	GLA
Monosaturated Fatty Acid	Palmitoleic Acid
Saturated Fatty Acid	Palmitic Acid

### 1.3.1 Mussel Oil Classes

#### 1.3.1.1 Fatty Acids

The term fatty acid describes a carbon chain of any given length with a carboxyl group on the end of the carbon chain. The carbon chain that extends out from the carboxyl group on the figure below can be of any given length with multiple variations occurring in nature (Fig. 3).

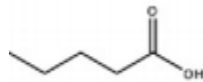


*Figure 3 Fatty Acid Complex (Hara, Kashihara, Ichimura, Tsujimoto, & Hirasawa, 2014)*

The terms commonly used to define fatty acids are:

- Free Fatty Acid (FFA): this is where the fatty acid is not bound to any other group, such as a glycerol molecule. A free fatty acid molecule consists purely of a carbon chain and carboxyl group.
- Long Chain Fatty Acids (LC-FA): Long chain fatty acids are fatty acids that contain a carbon chain greater than 19 carbons long. Where anything under 20 carbons long is defined as a Short Chain Fatty Acid (SC-FA).
- Polyunsaturated Fatty Acid (PUFA): this describes fatty acids that have more than one double bond in the carbon chain. This double bond linkage changes the geometry of the fatty acid molecule. The change in geometry depends on where the double bond linkages are located and the double bond density in the molecule. This is where terms such as omega-3, 6, and 9 come from. The omega-A term, commonly denoted as n-A, shows that the first double bond linkage is located at position A from the end of the carbon chain. Where the end of the carbon chain is located at the opposite end of the chain to the carboxyl group (Fig. 4).

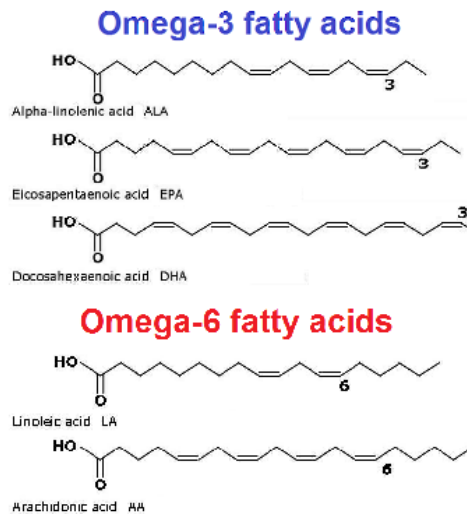


*Figure 4 Examples of Omega-3 and 6 PUFAs (Fat, 2017)*

The notation used to describe the carbon atom to double bond ratio is  $##:##$  n-#. For example, 22:4 n-3 informs the reader that there are 22 carbon atoms, with 4 double bonds in that chain, and that the first double bond is located at the 3<sup>rd</sup> carbon from the methyl end of the carbon chain. This is important due to the large variety of PUFAs and monosaturated fatty acids that are contained inside mussel oil. It is known that the LC-PUFAs, EPA (20:5 n-3), and DHA (22:6 n-3) are influential in inflammatory response control, as previously described above in Section 1.2 (Miller, Pearce, & Bettjeman, 2014).

- Monounsaturated Fatty Acid (MUFA): These acids are similar to polyunsaturated fatty acids, except for the fact that they contain only a single double bond in the carbon chain.
- Saturated Fatty Acids (SFA): Saturated fatty acids are straight carbon chains that consists purely of single bonded carbon atoms.

The fatty acids are prone to a hydrolysis from their glyceride carriers which can influence the proportionality of the fats within the mussel oil. Unsaturated fatty acids are also susceptible to light activated ionization, as well as thermal and oxidative degradation (Echarte, Zulet, & Astlasaran, 2001). Oil oxidation occurs in two steps; the first of which is called primary oxidation and results in the production of hydroperoxides. Secondary oxidation results in the breakdown of the aforementioned hydroperoxides to form aldehydes and carbonyl molecules (Choe & Min, 2006) (Miller M. , 2014). The valued portion of the mussels, EPA and DHA, are particularly susceptible to oxidation due to their double bond density as well as the conjugated double bond positions within the carbon chains (Spargue, Cooper, Tocher, & Betancor, 2018). Within MaLab's process, the temperature and light are regulated throughout the process. These two oxidation contributors are regulated by controlling the temperature of the mussels at all times and limiting the amount of natural sunlight that enters the factory, thus reducing the range of wavelengths that the mussels experiences as well as limiting exposure time, with most processing conducted in low ambient light or the dark. The three oxidation factors that are harder to regulate in the

process is the oxygen content of the macerate, water activity and presence of unsaturated fatty acids. There is an attempt to inhibit these oxidation pathways through the introduction of a stabilizing compound that is mixed into the macerate directly after homogenization.

### 1.3.1.2 Triglycerides

Triglycerides are made up of a glycerol molecule which is three carbons, each of which contain a hydroxyl group, combined with three free fatty acid molecules. The carboxylate group of the fatty acid is activated through a thiol linkage with acetylcoenzyme A (Acetyl-CoA) which is displaced by nucleophilic attack by one of the di- or tri-acyl glycerol form. Glycerol is polar and therefore, hydrophilic, and indefinitely miscible with water (Sigma-Aldrich, 2020).

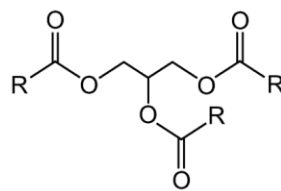
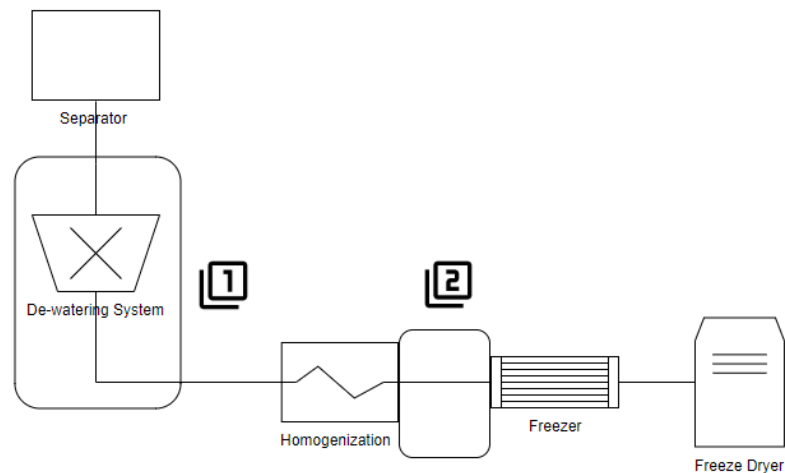


Figure 5 Generic Structure of a Triglyceride Molecule (Groot, Velikov, & Bakker, 2016)

### 1.3.2 Study Site

The study was conducted at the site (MacLab, Nelson, NZ) that is supporting the research. This factory brings in fresh mussels, shucks, macerates, freezes, and dries said fresh mussels. There is no chemical manipulation of the oil product. There are many ways to achieve the end state of dried mussels. Some of these include, freeze/vacuum, evaporative, and convective drying. Both evaporative and convective drying are based on bringing the product up to a temperature where the liquid will evaporate off the product. These methods risk a loss of the nutritive content of the mussels through the aforementioned oxidation pathways. Therefore, MacLab has chosen to dry the mussels by freeze drying, as this method reduces the risk of thermal oxidation and retains the nutritive content of the mussels.

The freeze-drying process is very time consuming due to the 24 to 48-hour runtime and consumes 2 kWh per kg of wet product (Cuddon, 2018). By lowering the water content of the mussel through pretreatment steps, this runtime can be reduced due to the lower water content of the initial frozen macerate in the freeze drier. The area of interest within the process flow is shown and described below (Fig. 6).



*Figure 6 Site Process Flow Overview with Marked Areas of Investigation.*

*(Area 1: Pre-Homogenization and Post De-Watering, where 10% of the Total Mass Resides as Water Droplets on the Mussel Surface)*

*(Area 2: Post Homogenization and Pre-Freezing, where the macerate is 80% Water)*

Separation removes any waste materials that may be in the raw product. In the GSM processing industry this waste comes in the form of, mussel shells, crabs, algae, other varieties of shellfish, and sea cucumbers.

There is an intermediate step between the separation and homogenization step where some surface water is removed from the whole mussel. The current de-watering process removes a percentage of the water that resides on the external surface of the mussel. On average 10% of the mussel's mass resides on the surface of the mussel as surface water. Removing additional surface water has been identified as being beneficial to the drying process.

This de-watering step is then followed up with a homogenization process that blends the individual particulates of mussel meat into a single slurry (macerate).

The macerate (containing, on average, 80% water) is then freeze-dried, milled, and delivered to another facility to remove the mussel oil. This investigation examines alternatives for additional water removal between the separation unit and the freeze drier. This investigation aims to identify processing steps that could be implemented into the current operation that could effectively reduce the water content of the GSMs and, therefore increase the solid content of the macerate that enters the freeze-dryers.

#### 1.4 Project

This project was taken on by Maclab to investigate new technology that have the potential to increase the solid content of the macerate prior to freeze-drying. The increase in the solid content could give a shorter dry-time and therefore increases the available throughput of the dryers, which can be translated

into a power saving of 0.02 kWh per freeze dryer per kg of water. Further calculation indicates that this would result in an annual saving of \$11,000.00 NZD on top of any increases in powder production.

#### 1.4.1 Aim

The goal of this research was to investigate and compare water removal methods prior to and post-homogenization. The chosen processing methods were compared based on their impact to the constraints, laid out in Section 1.4.2 , and how much water they removed from the product stream.

#### 1.4.2 Constraints

There are a few constraints that help to define the boundaries of this project. These constraints are described in the list below, where the solution must:

1. Be food safe as this product is destined for human consumption.
2. Not aerate the macerate in any way. The lipids within the macerate are highly susceptible to primary and secondary oxidation when the macerate is aerated as previously stated.
3. Be implemented after the shucking step and prior to the freeze-dryers.
4. Not add chemicals to the product as this will reduce the premium that is associated with an all-natural product.
5. Not adversely affect the mussel oil yield.
6. Not adversely affect other plant processes.
7. Have a small footprint as there is limited factory space available.
8. Must not heat the product above current operational levels.

These constraints were designed to help focus the research. After a review of possible de-watering alternatives (Chapter 2) two viable solutions were chosen for further evaluation:

Centrifugation of the raw mussels. This process would be situated between the current dewatering process and before the homogenization step (Figure 6, Area 1). Centrifugation of the whole mussels allowed the surface water to percolate through the pores between the mussels and met all the constraints stated above. The limiting factors for this method included the centrifugal force at which the pores between the mussels close, inhibiting percolation of the surface water through the mussel bed.

The second viable option chosen was to remove water from the macerate itself by absorption into an absorbent pad. This method could remove more than just the water component from the macerate. However the addition of an absorbent material will add an additional layer of insulation that may affect the time it takes to freeze the macerate thus violating the 6<sup>th</sup> constraint. The absorbent layer must be water specific as there is the possibility that the pad could remove some oil from the macerate. There may also be issues around removing the absorbent pad from the frozen surface of the macerate, post-freezing, as this pad must be removed before the freeze-drying process begins.

## Chapter 2 Alternate Water Removal Strategies

A literature review of differing drying methods was conducted. The following discussions identify various methods that could remove water from the process and considered any possible conflicts with the aforementioned constraints.

This section is broken up into two subsections. The first subsection discusses methods applicable to whole mussels prior to maceration. The second section covers different methods of water separation from a liquid phase stream, post-maceration. The water removal techniques in both sections will be discussed with respect to the previously stated constraints and any design or implementation considerations that apply.

### 2.1 Pre-Homogenization Solutions

There are many methods for removing fluids from the surface of particulate materials. The removal methods can vary in nature depending on the state of the particulate from which the fluid is removed. Methods of water removal from a surface are investigated in the following section.

#### 2.1.1 Pneumatic Systems

The use of an air-blade or air jet wiper to blow the fluid from the surface of the object. This can be in the form of a high-pressure gas phase fluid stream that pushes the surface fluid off the particulate material. This is used in bottling and canning industries to remove any residual fluid droplets from the bottle cleaning process.

This type of fluid removal is also common in the hygiene sector, with many of the hand-dryers in bathrooms containing this type of functionality. Current industrial practice, such as the Dyson air blade hand dryers, consist purely of this air jet wiping type system. These Dyson air blade type systems work very well on areas that contain droplets of fluid on the surface with a dry time of 10 s for two human hands. The speeds that these Dyson air blades achieve is approximately  $191 \text{ ms}^{-1}$  (Dyson, 2018). This air speed produces a thin sheet of air that is approximately 0.55 mm wide, which is the same width as the aperture (Dyson, 2018).

The limits of this drying method are that:

- The velocity of the air stream cannot be so large that it moves the smallest mussels off or down the belt. This would be detrimental as product would be lost off the belt, resulting in a lower conversion from green weight (mussel plus shell) to meat, ultimately breaching the 5<sup>th</sup> constraint.
- The air steam must not heat the product above the current level. This would conflict with the 8<sup>th</sup> constraint.

Additional considerations for an air blade system include:

- The air speed, as this parameter affects the force that the surface residing water molecules will experience. A greater the force is achieved through a greater air speed, which should provide a greater water removal. Although, as previously discussed, there is a velocity at which the air will move the mussels off the conveyor belt. Thus, making the air speed a limiting factor.
- Compression of the air and the relational temperature change. To achieve a higher velocity the air needs to pass through a compressor at some point within the system. Air that undergoes adiabatic compression experiences a change in temperature as the volume of the gas is changed, as described by the ideal gas law.
- Heat transfer between the air and the mussel. The heat transfer between the mussel and the air would need to be modeled, as the mussels cannot be heated during this new process. Otherwise the 8<sup>th</sup> constraint is infringed upon.
- Most air blade systems are designed with one air blade. This could lead to minimal efficiencies in water removal as the air blade would only be removing surface water from 50% of the surface as well as having a short exposure time. This could be mitigated by flipping the mussel or increasing the number of air blades.

### 2.1.2 Centrifugation

Utilizing physical effects, such as centrifugal force, to try and separate the fluid clinging to the outside of the mussel body. Centrifugation processes are well known and defined, in terms of separating solids of a different density, which is significantly different from what will be attempted to be achieved with this method. There was no reference of this type of method being used for removing surface water from the surface of a compressible solid, such as raw GSM mussels.

Some of the influencing factors that would be applicable to this separation method would be the:

- Speed of rotation or vibration, as this would change the forces applied to the mussels and associated surface water. The surface water must flow between the mussel interstices and the centrifuge bed, creating a drag force on the mussels. It was assumed that a greater speed, and thusly the greater the applied force to the water droplets, will result in more removed water. The speed of rotation, however, is limited by the fact that the mussels are compressible and relatively delicate. All the forces acting to deform the mussels will contribute to a reduced pore size. This reduced pore size will reduce the flowrate of the surface water through the pores and will ultimately end up inhibiting flow through the pores altogether.  
The force applied to the mussel depends on the speed of rotation as well as the radial distance of the mussel from the center of rotation. If the force applied to the mussels is too large there could be the possibility damaging the cells and the fats leaking out. If this method were to be chosen there would need to be tests conducted to make sure that the water coming off the mussels did not contain any fats, in accordance with constraint number 5.
- Surface tension of the water located on the surface of the mussel. The surface tension of the water droplets located on the surface of the mussel is one of the factors that affect how the water

moves off the mussel. Depending on the salt content of the water that is being removed, the surface tension properties will change. The way in which the properties change will depend on the salts that are present and their concentrations (Gao, 2011).

- Surface roughness of the mussels as these factors would affect the droplets ability to move over the product surface and contribute to the adhesion of the droplet to the mussel surface. It would be expected that there is an average surface roughness value over the outside of the mussel, although the organs located inside the mantle, such as the foot, are assumed to have significantly different surface roughness values compared to that of the mussel exterior. This difference in surface roughness values could be due to the function of the specific organ that is under inspection.

There are very few limiting factors, in terms of the constraints set, as centrifugation would not: add any chemicals; heat the product; or adversely affect downstream processing methods. In terms of the factors affecting the water removal, such as the surface tension and the surface roughness, they can be assumed to give an average value over the varying mussels. Investigating how these factors vary across the different growing regions and mussel sizes would take the focus of this report away from determining the feasibility of water removal via this method.

The centrifugation processing method fits nicely within the constraints and could be a viable option for investigation, as it does not violate any of the constraints stated above in Section 1.4.2 . The only constraint that could be infringed upon is the 5<sup>th</sup> constraint. If the force applied to the mussel is too great, then the mussel will start to break down thus causing a loss of the fatty portion of the mussel.

### 2.1.3 Absorption

Using absorbent materials to wick water from the whole mussel. Super absorbent materials (SAPs) are super absorbent polymers that can attract, absorb, and immobilize fluids. These SAPs could be used prior to maceration as the mussels could be rolled across the SAP, drawing the surface moisture off the mussels as they traverse the SAP belt. Implementation would need to be well thought out if the SAPs were to be used prior to maceration. If the SAPs were employed using a sheet style, similar to Sirane's product, *Dri-Fresh* (Sirane, Dri-Fresh, 2018), then this sheet would need to be changed regularly in order to protect the main product stream from microbial contamination. This means that there would need to be a limit for how long the sheet can stay in contact with the product and there would need to be a microbial study carried out to define the contact time.

Another factor to consider would be the effectiveness of using an SAP type solution. The flow rate of the mussels varies hour to hour depending on the number of mussels in stock, the conditions of the farms, and order size. With this variable flow rate and a limited contact time some of the absorbent pad will be unused, thus losing some efficiencies.

The following absorption mechanics and other physical phenomena also need to be considered:

- Contact time. The water takes time to absorb to the SAP and will absorb to different SAPs quicker depending on the functional groups that immobilize the water molecules (Zhang, Xu, Cao, & Zhang, 2015). If the contact time needed to fully utilize all of the absorbent material was greater than the contact time needed for bacterial replication then this method of water removal could impact the constraints set out above in Section 1.4.2 , more specifically the 1<sup>st</sup> constraint.
- Then there is also the factor of diffusion through the absorbent material. As the absorbent's contact surface becomes saturated, the water must diffuse through the absorbent in order to reach vacant absorption sites. There are a number of factors that influence the diffusion of the water through a porous material, some of which include: temperature, as the temperature has an effect on the kinetic energy of the water molecules, thus impacting the rate of diffusion; porosity of the material, a greater pore size in the material will result in a greater diffusion rate as the fluid can travel through these pores with less resistance; and the hydrophilicity of the material will also influence diffusion as a more hydrophilic material will draw the water through the pores in the material, thus increasing the rate of diffusion. In terms of the constraints set in this investigation, there would be no infringements made in respect to this physical phenomenon.
- Ability for absorbent-absorbate contact. Some of the absorbent materials offered by companies, such as *Sirane*, have the absorbent material encased inside a perforated plastic sleeve to prevent absorbent-product contact. For the water to reach the absorbent material, it must first pass through the perforations in the plastic layer. Depending on how the absorbate is meant to cross this plastic layer will define how the absorbate contacts the absorbent surface. If the water cannot pass through the perforations easily, then the absorption of the water will be limited to the rate at which the water can cross the plastic boundary. The plastic sleeves are used to separate the product from the absorbent in cases where the absorbent has the potential to lose structural integrity after saturation. *Sirane* also offers product-absorbent alternatives that are food safe, although these alternatives tend to be structurally weaker than their sleeved counterparts. To increase the number of absorption sites the absorbents are made from cross-linking (cross-linking is optional) polymer chains, such as that of sodium polyacrylate.

Overall absorption using an SAP could be a viable option for water removal, although the investigation into this water removal technique would need to be centered around the time needed for absorption and the time needed for microbial replication. There are other, smaller, complications that could take the focus away from the point just mentioned. These smaller issues would include the transport of the water to the SAP if there was an interfacial layer present; product flow variability and the effect this has on the unused portion of the SAP; and the effect of differing functional groups on the absorption capacity.

#### 2.1.4 Pre-Homogenization Conclusions

Of these potential solutions, the solution that best fits the constraint space is the use of centrifugation. This is a method for removing water from the surface of the mussel and will provide a sanitary separation method that has no possibility of adding chemicals to the product.

Centrifugation does not add any potential contamination to the mussels and there are no heating effects; the mussels are in the same condition prior to centrifugation, less some surface water. However, mussels are a deformable material and the angular velocity of the centrifuge could deform the mussel bed to the point where mussel oil is lost. This deformation of the mussel bed could also block the flow channels for the surface water, or potentially shred the mussel meat through the holes in the centrifuge basket. Therefore, modeling the centrifugal forces on the bed of mussels and determining how the permeability of the mussel bed varies with this force are necessary to specify the centrifuge to be used. These equations and background information will be discussed further in Section 3.1.2 .

## 2.2 Post Homogenization Solutions

When researching post homogenization drying methods, the macerate can be thought of as a viscous homogenate of water, protein, and liquid lipids. The following processes are based on removing water from a liquid product stream:

### 2.2.1 Evaporation

Evaporators can come in many different forms some of which include, falling film, short tube, thin film, and multiple effect evaporators. Evaporators are designed to change the phase of the fluid being removed. The existing freeze-drying process is evaporative in nature but designed to keep the temperature lower than the boiling of water under standard atmospheric conditions. Some important factors to consider, in terms of the project at hand, are:

- Boiling point temperature of water at standard atmospheric conditions. Water has a boiling point of 100 °C at standard atmospheric conditions. At this temperature, the mussel macerate will cook affecting the oil yield that is received from this product. This would not be a viable option as it directly impacts the 5<sup>th</sup> constraint set out above, in Section 1.4.2 .  
Lowering the pressure to a vacuum would change this more into the realm of the existing vacuum drying. Vacuum drying works on the principal that lowering the system pressure reduces the vapor pressure and the temperature required to vaporize the water.
- Microbial growth. Nandini et al. (Nimbkar & Rajvanshi, 2013) showed a sterilization temperature of 65 °C inactivated non-spore forming bacteria. This problem is avoided in the frozen state during freeze-drying.
- Thermal degradation of the mussel oil content. With an increased processing temperature, the risks of degrading the mussel oil content of the mussels also increases. Javier et al. (Moros, Roth, Garrigues, & Guardia, 2009) have shown that temperatures above 100 °C will reduce the unsaturated oil content of edible oils. Although this was dependent on the type of oil being tested and the duration of the temperature. This line of study shows that the degradation profile is specific to that of the oil's origin, therefore there would need to be an investigation into how the mussel oil composition changes at an increased temperature. Mussel oil is high in PUFAs, such as DHA and EPA, some believe (Personal communication, 2018) that it is the GSMs unique

combination of different oil types that makes it so effective as an anti-inflammatory supplement. This belief would further complicate the amount of testing required to investigate evaporation as a viable water removal technique.

- Adverse effects on downstream processing methods. After the homogenization of the mussels there is a freezing process that brings the product down to -20 °C. If there was a heating process prior to this current freezing process, then the temperature of the incoming product would be increased. This increase in inlet temperature would also increase the heat load on the freezer unit. This would adversely affect the downstream processing methods, therefore impacting the 6<sup>th</sup> constraint.

Evaporation as a water removal technique would require the assurance of no impacts on the 1<sup>st</sup>, 5<sup>th</sup> and 6<sup>th</sup> constraints stated above, in Section 1.4.2 . The impacts on the 1<sup>st</sup> and 5<sup>th</sup> constraints require testing to be proven, whereas impacts on the 6<sup>th</sup> constraint is a definite as long as the temperature used for evaporation is above that of the current product temperature at the freezer inlet. This means that standard evaporation (evaporators that operate at 100 °C and 1 kPa) cannot be used, a low-pressure version would be required. If a low-pressure option were chosen the result would be akin to that of the current freeze-dryers that are located on site, thus making the addition redundant.

### 2.2.2 Absorption

As previously discussed in Section 2.1.3 above, absorbent materials are used in many industries for various reasons, they are generally used to immobilize a specific liquid phase material. This immobilization is caused by the absorbent material binding with the liquid molecules, the binding affinity of the absorbent depends on the functional groups that are attached to the backbone structure. After the mussels have been macerated, the semi-solid solution produced contains both non-polar and polar components. The macerate contains mussel oil, which is composed of non-polar organic molecules, and water, which is polar. Therefore, the selection of the absorbent material is important. Other important factors to consider if this solution were to be chosen for further investigation would be:

- Absorbents physical form. For this solution to be viable the physical form of the absorbent would need to be chosen correctly. Absorbent materials can come in many different forms some of which include, powders, sheets, and granules. The most well-known products that are constructed from absorbent materials, are diapers and fruit packing. These two common products are, usually, made from crosslinked polymers and are commonly referred to as super absorbent polymers (SAPs). Although, their physical forms differ from one another. Diapers use a powder form of SAP, whereas fruit packing generally uses a sheet. The form of the SAP is important because the SAP needs to be removed from the macerate before the freezing-drying process. If the SAP cannot be removed from the macerate then this would negate any net moisture reduction benefits and it would infringe on the 1<sup>st</sup> and 4<sup>th</sup> constraints set out in Section 1.4.2 . However, a practical solution could be found with one of the many suppliers that provide SAP sheets for food processing needs. One example of such a product is the Dri-Fresh line from Sirane. The *Dri-Fresh*

range from Sirane are SAPs that are specifically used for removing unsightly fluid from fruit/meat produce containers (Sirane, Dri-Fresh, 2018).

- Effects on downstream processing. The SAP could be applied to the macerate just prior to the macerate entering the freezer, thus removing water while the macerate freezes. This methodology could impact the constraints set out above, as adding an absorbent sheet to the macerate will insulate the macerate and may slow the freezing of the macerate. Thus, the effect of the addition of the SAP to the freezing process needs to be investigated. An understanding of the impact to, the freezing time of the macerate, the thermal conductivity and the heat capacity of the SAP layer will be critical to this method's success. Furthermore, the absorption time must fit the window of opportunity before the macerate freezes. The inverse of the thermal conductivity is known as the thermal resistivity. In this case the thermal resistivity would be used to find the rate limiting material within the system. If the rate limiting material was found to be the SAP then this would indicate that the addition of the SAP would impede the freezing of the macerate, violating the 6<sup>th</sup> constraint.
- Ease of removal. Another effect on downstream processing that needs to be considered is the ease of removal of the SAP sheet. As previously stated, the physical form of the SAP is important for the separation of the SAP and the macerate, which is why a sheet was decided as the best option. The SAP could either be placed on top of or beneath the macerate layer, both options have their own attributes and shortfalls. Having the absorbent sheet located on the top of the macerate will provide the easiest removal, as the sheet can be peeled off the top of the macerate post-freezing. Whereas if the absorbent sheet is located beneath the macerate, the operator that is stacking the slabs will have to separate the macerate/absorbent layer/plastic liner layer from the tray and then remove the plastic liner layer and the absorbent layer and then re-apply the plastic liner layer to the tray, then re-apply the frozen macerate slab. The benefit of having the absorbent layer located beneath the macerate is this should promote fluid transport to the absorbent. This fluid transport promotion is due to the gravitational forces that would be acting on the macerate. This would be the opposite if the absorbent sheet were located on top of the macerate as the water would then be opposing the gravitational forces. Thus, making water transport between the macerate and absorbent material more difficult.
- Effects on the mussel oil content. With all the processes that are stated in this report, the most important constraint that needs to remain un-constricted is the 5<sup>th</sup> constraint. All the methods stated need to ensure that the ultimate mussel oil yield is unaffected by the additional processing step. There could be the possibility of the oil content of the macerate leaching into the absorbent layer. This could either be due to some affinity with the absorbent material or it could be as simple as a portion of the oil gets entrained in the water movement towards the absorbent.
- Absorption rate. The rate of absorption differs depending on the temperature, concentration gradient and affinity between the absorbent and absorbate. If this process is added to the process during the freezing of the macerate, then there will be a decreasing temperature gradient while the absorbent is in contact with the macerate. The absorption will also be limited by the time it takes to freeze the water in the macerate. Once the water is frozen there will be no chance of absorption as the water molecules are already immobilized. It is generally accepted that pure water, under atmospheric pressure, freezes at 0 °C. The addition of the salts, proteins, and other

organic material in the macerate changes the freezing point of the macerated solution. It is known that the freezing point of the macerate sits around  $-5^{\circ}\text{C}$ .

SAPs could be used to remove some water from the macerate if they meet the constraints. The SAP sheets could be placed on the macerate as it enters the freezing unit, therefore adding an operating step to incorporate dewatering into the freezing process. It is unclear if the use of SAPs will violate the 5<sup>th</sup> or 6<sup>th</sup> constraints. They could have an adverse effect on the freezing of the macerate and could affect the ultimate mussel oil yield. This processing method would have to be investigated further to answer these questions.

### 2.2.3 Osmosis

Osmosis describes the movement of molecules through a selective membrane. This movement of molecules is driven by either chemical potential (osmotic gradients) or pressure gradients. Where there is a high concentration of a membrane-permeable-molecule on one side of the membrane and a low concentration of said membrane-permeable-molecule on the other side of the membrane. The molecules will continue to flow across the membrane until the chemical potentials on both sides of the membrane are equal. In reverse osmosis systems there is pressure applied to the side that is to undergo water removal to drive the permeate (water, in this case) through the membrane. This pressure difference overcomes the chemical potential gradient, so that the permeate can pass through a semi-permeable membrane to the area of lower pressure and higher concentration. The following would need to be considered if this processing method were chosen for investigation:

- Plant size: One of the constraints for this research is that the solution must have a small footprint as there is not much free space in the factory. RO (Reverse Osmosis) plants are generally large due to the surface area required for mass transfer. As well as the surface area required for mass transfer, there are large pressures that need to be achieved to achieve mass transfer across the semi-permeable membrane. Thus, resulting in a large floor requirement for the pressure generating equipment.
- Plant cost: Osmotic processing plants are quite new in terms of industrial applications, thus making the processing equipment, such as semi-permeable membranes, expensive.
- Effect on mussel oil. It would need to be assured that there was no mussel oil crossing over the membrane during processing. Semi-permeable membranes are generally selective on which molecules can pass through. This selection comes in a few different forms, some of which include, size selectivity or the molecular affinity between the absorbent and absorbate.
- Processing operation: It is known that the current macerate solution contains many large particulates of cellular mass. Osmosis uses a well homogenized solution. It can be assumed that the current state of the macerate will result in the blockage of the semi-permeable membrane pores within seconds. Thus encroaching on the 6<sup>th</sup> constraint.
- Osmotic understanding: It would need to be understood how the osmotic effectiveness changes with varying temperature and concentrations.

This processing method would not work for this research project as the macerate still contains a significant amount of fibrous and cellular material and would foul the permeable membrane within minutes if not seconds. Luo et al. observed a decay in flux after four hours, when experimenting with dairy waste (Luo, Ding, Wan, Paullier, & Jaffrin, 2011). As well as the blocking of the membrane pores, the capital cost associated with and the footprint required for osmotic processing systems are very high, as the selective membranes and high-pressure pumps (used in reverse osmosis systems) are expensive and numerous.

#### 2.2.4 Liquid-liquid Extraction

Liquid-liquid extraction or similar type extractions use the solubility of a material in a solvent to draw it out from a solution. For this application, the mussel macerate would have to be submerged in a solvent that can bind to the water or the oil therefore, removing any water or oil from the mussel macerate. Some of the factors that would need to be considered for the viability of this processing method would be:

- Residual chemicals post-stripping. There must be no residual solvent left in the mussel macerate as this would change the chemical composition of the mussels and therefore, violate the 4<sup>th</sup> constraint. The research conducted on stripping solvents concluded that there are no intrinsically safe polar solvents that are water soluble, thus a vigorous health and safety review of the process would be required. The solvent would also have to be recycled to improve efficiencies, which would require another study to choose/develop the recycling method.
- Effect on downstream processing. Once the water has been removed from the macerate the remaining solution will need to be stripped of the solvent used to remove the water, otherwise the 4<sup>th</sup> constraint is impacted. Then the solution still needs to be frozen and freeze dried. If there is any solvent left in the macerate prior to freezing this will alter the freezing point of the macerate, thus impacting downstream processing and encroaching on the 6<sup>th</sup> constraint.
- Contact time. The contact time needed to remove the water, or the oil from the macerated solution would need to be investigated as this would decide the size of the device as well as any impacts on the 7<sup>th</sup> constraint. The contact time is also connected to the separation efficiency. This would indicate that there may be an efficiency/size trade-off.

In conclusion, this processing method does not appear to be a practical approach for water removal. The solvent would be difficult to remove and recover from the waste stream. Furthermore, any contaminating solvent in the residual product phase would violate the 4<sup>th</sup> constraint.

#### 2.2.5 Post-Homogenization Conclusions

The use of SAPs was deemed to be the only post-homogenization process that would fit within the process constraints and, additionally, have the best potential to remove the water from the macerated mussels. This option was chosen because: it has the potential to remove water from the macerated mussels in a passive manner; it has the capacity to not add any chemicals to the main product stream; and it requires little to no footprint or associated equipment, it only requires personnel to remove the absorbent sheet

at the end of the freezing process. Furthermore, the water that is freed upon maceration could also potentially be removed instead of only the surface water.

The major points for investigation when implementing this process were: the effect it has on the freezing process, in terms of the added insulation to the macerate; the time for absorption before the water is frozen and immobilized; the effect on the mussel oil yield; and the amount of water removal that is possible from this processing method.

Section 3.2.1 will cover the basic thermodynamic concepts behind this process and the rough methodology needed to solve the sets of equations discussed later in sections 3.2.4 and 3.2.5. The time for absorption, freezing time of the macerate, effect on mussel oil yield and possible water removal were determined experimentally.

### 2.3 Removal Methods Summary

The aim of the project is to investigate processing methods that have the potential to reduce the water content of the mussels prior to freeze-drying. The possible solutions were broken into two processing areas, pre- and post-homogenization of the mussels. Two potential solutions were chosen for further investigation. Within the pre-homogenization processing area, centrifugal de-watering was selected which required determining the optimal industrial centrifuge design. Whereas, in the post-homogenization processing area, SAP's were selected because of their potential to remove the water contained that is freed due to maceration. The SAP process requires an understanding of the heat transfer between the macerate and the freezer and any effects on the mussel oil yield.

The centrifugation process is a function of the centrifuge radius, rotation speed and mussel deformation rate as a function of both drag and centrifugal force within the mussel bed. As force is applied to a mussel it will deform, the greater the force, the greater the deformation. There was a force at which the deformed mussels prohibited water percolation through the bed, which is defined as the maximum applied pressure (MAP). To find this maximum applied pressure an experiment was conducted using a static pressure vessel. The centrifuge design considered two extremes 1) when the bed is full of water and 2) when the bed of mussels is dry.

Absorbent type processing was chosen as the post-homogenization processing method to be further investigated. This processing method was chosen based on using an absorbent sheet to wick moisture away from the macerated mussels. The first question to be addressed is the position (top or bottom) of the absorptive sheet relative to the mussel macerate. The positioning of the absorbent material is also key to the freezing of the macerate and ease of SAP removal post-freezing. The effect that the absorbent pad has on the freezing of the macerate will depend on the associated heat transfer between the macerate and the air in the freezer. Thus, a model for the heat transfer was proposed and is detailed in Section 3.2. This section describes the heat transfer through the top half of the macerate to the air as well as the heat transfer through the bottom half of the macerate, through the tray and to the air. Once these two heat flows were modeled an informed decision was made on whether the absorbent sheet should go on top of the macerate or the bottom. Then the absorbent material was tested to determine

the amount of water removed from the macerated mussels, and any effects on the mussel oil content were quantified.

Both solutions were compared based on their key attributes in relation to the aim. These key attributes were the amount of water removed from the product stream and any effects on the mussel oil content. This data allowed Maclab to determine the suitability of each solution.

## Chapter 3 Theory

Two approaches appeared worthy of further investigation from the investigation of alternatives in Chapter 2: 1) Pre-homogenization centrifugation (Section 3.1 ) and 2) Post-homogenization absorption (Section 3.2 ). In this chapter the engineering principles underlying these approaches is described, establishing both parameters that need to be empirically determined and how to determine these.

For pre-homogenization centrifugation, the critical issue is the maximum force that can be exerted on a mussel. There are two limiting cases to consider. The first is the dry bed of mussels, where the surface water has been removed but the centrifuge is still spinning. The second is the case where the bed of mussels contains water. In this section a mathematical model for the centrifuge and solution for steady-state operation at both these operational limits is developed. This model is then used to specify the industrial centrifuge design.

For post-homogenization absorption, the critical issue is the effect that the superabsorbent pad will have on the freezing of the macerate and the amount of water that can be absorbed before the water is immobilized due to freezing. This requires developing a temporal model for the cooling of the macerate. Secondary issues, like the position of the absorbent pad (above or below the macerate), how much mussel oil is lost to the pad, and ease with which the pad can be removed without loss of macerate will be addressed experimentally (Chapter 4).

### 3.1 Centrifugation Model

Centrifugation has been around for many years and is a well-defined process. Centrifugation is generally used in density differential separation, this can either be liquid-liquid or solid-liquid separation. In this circumstance the separation type is solid-liquid separation as the aim of the process is to remove the water that is situated on the surface of the whole mussel.

#### 3.1.1 Centrifuge Design

For this separation the liquid is the waste and the solids are retained as the product stream, which means a 'basket-type' centrifuge design in which the bowl consists of two parts, an inner perforated bowl (basket) to retain the mussels, and an outer solid bowl to trap the waste water. The motor spins the bowl at a constant speed, at which point, the water that is located on the surface of the mussel flows via centrifugal force outward through the inter-mussel pores in the bed and eventually through the perforations in the inner bowl where they are collected in the outer bowl (Figure 7) and drained off.

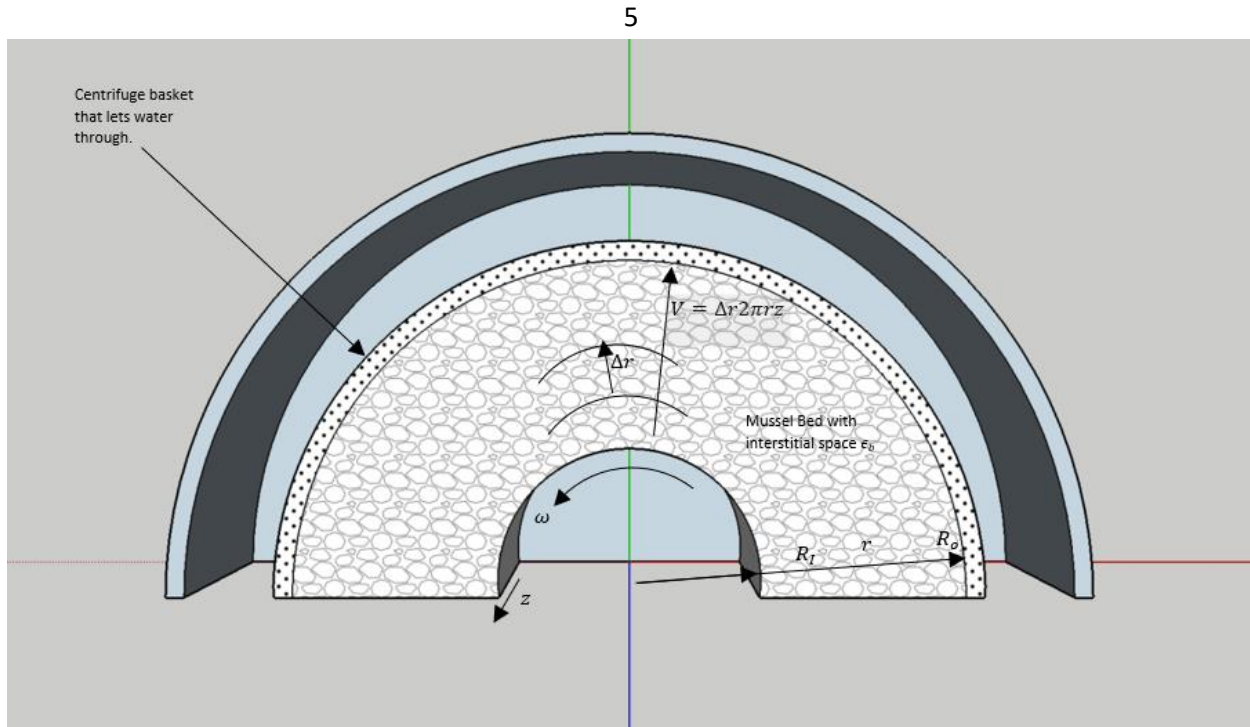


Figure 7 Centrifugal System

### 3.1.2 Shell Material Balance for Centrifuge

The variables that are involved in defining a centrifuge system are well known and relatively simple to understand. Due to the nature of the research at hand, the main constraining feature of the centrifuge will be the centrifugal force that is applied to the mussels. The applied centrifugal force influences how much water is removed from the surface of the mussels, the size of the percolation pores in the mussel bed and overall deformation of the mussels.

For this research project, it is unclear as to which centrifugal force would acquire the highest water removal from the mussels without deforming the bed of mussels. Therefore, the first piece of information that was needed is the MAP as this was translated into a force through a minor manipulation ( $P = \frac{F}{A}$ ). This MAP was empirically determined using a custom static pressure vessel as described below in Section 4.1.1. A static pressure vessel was chosen to investigate the MAP as this would allow for the percolation to be investigated as a function of pressure. Having a static pressure vessel would also allow for the bed height to be investigated in relation to the pressure and the water percolation rate, as it was expected that the bed compresses as the applied pressure is increased. The theory for the static bed section is laid out in Section 3.1.6.

Once the MAP had been found it was converted to a force as previously stated. This force was then used to design the centrifuge to the correct specifications to get the maximum water removal from the mussels at a given applied mussel mass. To understand how the centrifugal force relates to the design parameters of a centrifuge, a centrifugal model needed to be constructed that linked the centrifugal force to the

design parameters. The basic design parameters include inner bowl diameter, revolution speed of the inner bowl, and the height of the mussel bed.

### 3.1.3 General Centrifuge Model

The centrifuge model was based on a solid body within a perforated centrifuge basket that rotates horizontally about its axis of symmetry. The mussels do not act like a solid body when inside the centrifuge due to the combination of the void spaces between the mussels and the pliable nature of biological material. These void spaces are essential for water removal as the water travels through these channels, providing separation of the water from the surface of the mussels. These flow channels gradually reduce in size as the centrifugal force is increased therefore, the pressure, and thus the force, required to completely close the channels within the bed needed to be known, as it was used as a design parameter when designing the centrifuge.

Before the MAP was empirically determined, the pressure drop across the mussel bed was first related to the radial distance from the center of rotation. To find this relation, an understanding of how the system will be operated and a definition of the variables involved is required. The problem is best defined as a transient problem with a clear start and finish. The bed of mussels will be transitioning from a state where the bed is full of water to a situation where there is no water left in the bed. Both solutions were derived from a single momentum balance (Eq. 1).

$$\begin{aligned} \rho \left( \frac{\partial v_r}{\partial t} + v_r \frac{\partial v_r}{\partial r} + \frac{v_\theta}{r} \frac{\partial v_r}{\partial \theta} - \frac{v_\theta^2}{r} + v_z \frac{\partial v_r}{\partial z} \right) \\ = -\frac{\partial P}{\partial r} - \left[ \frac{1}{r} \frac{\partial}{\partial r} (r\tau_{rr}) + \frac{1}{r} \frac{\partial \tau_{r\theta}}{\partial \theta} - \frac{\tau_{\theta\theta}}{r} + \frac{\partial \tau_{rz}}{\partial z} \right] + \rho g z \end{aligned} \quad (1)$$

With respect to the mussel's reference frame, all the terms can be removed except for the pressure difference in relation to the radius  $\left(\frac{dP}{dr}\right)$ , the centrifugal force  $\left(\frac{v_\theta^2}{r}\right)$  and the drag force per unit volume  $\left(\frac{1}{r} \frac{\partial}{\partial r} (r\tau_{rr}) + \frac{1}{r} \frac{\partial \tau_{r\theta}}{\partial \theta} - \frac{\tau_{\theta\theta}}{r} + \frac{\partial \tau_{rz}}{\partial z}\right)$ . The path of the water through the bed is poorly defined. However, the Bernoulli derived equation for viscous drag equation used by Cameron et al (Cameron, Nikora, & Marusic, 2019) can be substituted for the force drag force per unit volume in Eq. 1. Where the drag force is proportional to the drag coefficient ( $C_D$ ), linear velocity squared ( $\vec{v}$ ), density ( $\rho$ ) and the average wetted surface area of the pores ( $SA_{pores}$ )(Eq. 2).

$$\frac{F_{Drag}}{vol} = \frac{\left(\frac{1}{2} C_D \rho \vec{v}_{ave}^2 SA_{pores}\right)}{2\pi r z \Delta r} \quad (2)$$

This leaves the following, condensed, wet bed equation (Eq. 3)

$$\frac{\rho v_\theta^2}{r} = -\frac{dP}{dr} + \frac{\left(\frac{1}{2} C_D \rho \vec{v}_{ave}^2 SA_{pores}\right)}{2\pi r z \Delta r} \quad (3)$$

The centrifugal force (Eq. 4) per unit volume is derived from the momentum balance in the radial direction, where the centrifugal force is proportional to the tangential velocity at point  $r$  ( $v_\theta$ ) and inversely proportional to the radius ( $r$ ).

$$\frac{F_{Centrifugal}}{vol} = \frac{\rho v_{\theta}^2}{r} \quad (4)$$

It should be noted here that the tangential velocity term ( $v_{\theta}$ ) in Eq. 5 is also a function of the radius as the centrifugal acceleration is proportional to the angular velocity ( $\omega$ ) and the radius ( $r$ ) (Eq. 5).

$$v_{\theta} = \omega r \quad (5)$$

Applying these two simplifications to the condensed general bed equation (Eq. 3) gives an intermediate equation that contains a clear set of variables (Eq. 6).

$$\rho \omega^2 r = -\frac{dP}{dr} + \frac{\left(\frac{1}{2} C_D \rho \vec{v}_{ave}^2 S A_{pores}\right)}{2\pi r z \Delta r} \quad (6)$$

The drag force section of this intermediate general equation (Eq. 6) can be developed further to simplify the equation. Where the centrifugal and the pressure components of the intermediate general equation is well defined, the drag force component contains two variables that are poorly defined yet will be geometrically constant. These two variables are the drag force coefficient ( $C_D$ ) and the surface area of the pores ( $S A_{pores}$ ). Where the surface area of the pores is a function of the tortuosity of the pores ( $k$ ); the number of pores ( $n$ ); the change in the radial direction; and the particle diameter ( $d_p$ ) as shown in the equation below (Eq. 7).

$$S A_{pores} = n d_p (1 + k) \Delta r \quad (7)$$

Where the number of pores can be written as a function of the number of pores per unit area ( $\gamma$ ) times by the area ( $2\pi r z$ ) (Eq. 8).

$$n = 2\pi r z \gamma \quad (8)$$

By substituting the pre-equation (Eq. 7) into the surface area of the pores equation (Eq. 8) gives an expanded version of the surface area equation (Eq. 9).

$$S A_{pores} = 2\pi r z \gamma d_p (1 + k) \Delta r \quad (9)$$

This developed surface area equation (Eq. 9) was then substituted into the intermediate general momentum balance equation (Eq. 6) and gives the final, non-simplified, general momentum balance equation (Eq. 10).

$$\rho \omega^2 r = -\frac{dP}{dr} + \frac{1}{2} C_D \rho \vec{v}_{ave}^2 \gamma d_p (1 + k) \quad (10)$$

This, non-simplified, general momentum balance contains complex variables that are derived from the mussel geometry and the flow of the fluid past these particulates. These particulate based terms ( $C_D$ ,  $\gamma$ ,  $d_p$  and  $(1 + k)$ ) were lumped into a single variable. This singular variable is referred to as the lumped drag coefficient ( $C'_d$ ) leaving Eq. 11 as the final general momentum balance.

$$\frac{dP}{dr} = \rho r \omega^2 + C'_d \rho (\vec{v}_{ave})^2 \quad (11)$$

This final general momentum balance was used to solve the various scenarios explored in this report with only a few further developments.

### 3.1.3.1 Mussel Reference Frame Momentum Derivation

When there is fluid flowing through the bed of mussels the pressure gradient across the bed is the summation of the drag and centrifugal forces which Eq. 11 depicts. From this general momentum balance the velocity term can be expanded to its more primitive components using Eq. 12.

$$\vec{v}_{ave} = \frac{V}{2\pi rz} \quad (12)$$

After substituting Eq. 12 into Eq. 11, the terms that are constant in the general momentum balance become more clear (Eq. 13). From this wet bed model, it can be seen that the constants are the apparent density of the mussels ( $\rho_a$ ), angular velocity ( $\omega$ ) and the bed height ( $z$ ). This leaves four variables in the equation, the radius ( $r$ ), volumetric flow rate through the bed ( $\vec{v}_{ave}$ ), pressure gradient ( $dP$ ) and the lumped drag coefficient ( $C'_D$ ).

$$\frac{dP}{dr} = \rho_a r \omega^2 + C'_D \rho_a \left( \frac{V}{2\pi rz} \right)^2 \quad (13)$$

Where the boundary conditions for this scenario are that; 1) there is no pressure gradient at the center point of the centrifuge ( $\Delta P = 0$  at  $r = 0$ ); and 2) the pressure gradient is non-zero at any distance,  $r$ , away from the center of the centrifuge ( $\Delta P \neq 0$  when  $r > 0$ ).

In order to solve Eq. 13 the lumped drag term and the volumetric flowrate through the bed had to be defined.

The solution to the lumped drag term definition issue was to simplify the general momentum equation so that a relation between the lumped drag coefficient and the fluid velocity could be found. This led to the development of the static bed experiments (Section 3.1.5 ).

The linear flowrate in the centrifuge changes as the radial distance from the center changes, which deviates from common conceptions. The volumetric flowrate of the water through the bed is only constant at steady state. At this steady state, the drag force of in the system will be equal to the centrifugal force within the system. This means that there must be a specific value of  $V$  that satisfies the balanced force equation and the steady state equation. The balanced force equation is derived relative to the fluid reference frame in the following section.

### 3.1.3.2 Fluid Reference Frame Momentum Derivation

Starting from the same generic momentum balance seen in the section above (Eq. 13), the pressure differential was nullified as the water is able to pass through the bed of mussels and out of the perforated basket. The only other aspects of the general momentum balance that needed to be changed were the sign that was attached to the drag force, so that the drag force cancels out the centrifugal force. The other variables that needed to be changed were the density terms. The density terms were changed so that they were depicting the correct reference frame, that of the water. Removing this non-applicable factor from the generic momentum balance gives the condensed fluid momentum balance (Eq. 14) .

$$0 = \rho_w r \omega^2 - C'_D \rho_w \left( \frac{V}{2\pi rz} \right)^2 \quad (14)$$

Substituting in equations for the linear velocity (Eq. 12) and the centrifugal force (Eq. 5) and rearranging the terms gives a relation for the volumetric in terms of the radius and angular velocity (Eq. 15).

$$V(r) = \frac{2\pi z(\omega r^2)}{\sqrt{\left(\frac{C'_D(r-1)}{2}\right)}} \quad (15)$$

At steady state there was a radial value at which the differential was constant. Differentiating Eq. 15 with respect to radius and solving for the radius when the differential is constant ( $\frac{dV}{dr} = 0$ ) gave the steady state radius. The differentiated form of equation 15, as differentiated by Matlab's symbolic solver (Eq. 16).

$$\frac{dV}{dr} = \frac{4\omega\pi r z}{\sqrt{\frac{C'_D(r-1)}{2}}} - \frac{C'_D\omega\pi r^2 z}{2\left(\frac{C'_D(r-1)}{2}\right)^{\frac{3}{2}}} \quad (16)$$

Setting the differential (Eq. 16) to zero and solving for the radius revealed the radius at which steady state is achieved. This steady state radius can then be used in equation 15 to find the steady state volumetric flow rate. Once this volumetric flow rate had been found it was used to solve the wet bed model for the force as a function of radius and angular velocity.

### 3.1.4 Dry Bed Centrifuge Model

The centrifuge model was solved for two scenarios. The first of which is the wet case (as seen in the section above) where there was some water within the bed, which indicated that there was drag and centrifugal forces acting on the bed. The second scenario was for a dry bed, which was when the centrifuge had removed all the water from the surface of the mussels.

In this dry bed scenario, there is no drag force acting on the bed anymore, greatly simplifying the solution. From the general momentum balance (Eq. 13), the only term that was removed was the drag force term leaving behind the pressure gradient and centrifugal terms. Along with this removal of the drag term the density term needs to reflect the situation as well (Eq. 17).

$$\rho_m \left( -\frac{v_\theta^2}{r} \right) = -\frac{dP}{dr} \quad (17)$$

With the knowledge that pressure is just force per unit area (Eq. 18) one can substitute this into the condensed dry bed momentum balance.

$$P = \frac{F}{A} = \frac{F}{2\pi r z} \quad (18)$$

After substitution and integration with respect to the inner radius ( $r_i$ ) and an arbitrary distance ( $r$ ), the final dry bed force equation can be deduced (Eq. 19).

$$F(r) = \pi r z \rho_m \omega^2 (r^2 - r_i^2) \quad (19)$$

The last thing that needed to be substituted into this equation set was the apparent density ( $\rho_a$ ). The apparent density of the mussel was related to the buoyant force acting on the mussel from the addition of the water, in this case there is no water and therefore, no buoyant force, so the apparent density is that of the mussel ( $\rho_m$ ).

With both the dry and wet bed scenarios it can be seen how much effect the drag force has on the centrifuge system and how the force changes with both angular velocity ( $\omega$ ) and the radial distance from the center of the centrifuge using the MAP gathered from the static bed experiments. It was also seen at which angular velocity and radius the force will be great enough to close the interstitial spaces between the mussels. Or in short at what point the centrifuge will prohibit water percolation.

### 3.1.5 Static Bed Background

With the pre-homogenization problem set, having to investigate how the centrifugal force varies in relation to the water movement through the inter-mussel pores prior to the centrifugal design, means that the centrifugal force and the water flow rate must be married together. There was a force at which the pores in the mussel bed closed completely and therefore prevented the separation of the water from the surface of the mussels. Mussels are best defined as non-spherical and semi-compressible particulates which makes modeling the bed exceedingly difficult.

A similar approach to the centrifuge theory was taken for the static bed model. A force balance was conducted on the system in order to find how the applied water pressure interacts with the linear velocity of the water through the bed.

### 3.1.6 Static Bed Model

Most equations that describe pressure drop over a packed bed reactor, like the Ergun equation, rely on the assumption that the packing is solid and therefore the void space between the particles are constant. It was assumed that the bed of mussels could be considered as non-deforming up until deformation occurs, at which time the mathematical model that was proposed will break down.

The average linear velocity through the static bed depends on the bed porosity and is affected by the drag force that is applied to the bed. It was assumed that the bed porosity was constant while the total force was below the deformation value. The same drag force equation seen in Section 3.1.3 was used as a starting point for the static bed model (Eq. 9), where a lumped drag coefficient term ( $C'_D$ ) was used to collect all of the unknown terms associated with the surface area of the bed pores ( $SA_{pores}$ ) under a single term. These unknown parameters, that were associated with the surface area of the bed pores ( $SA_{pores}$ ), were the: bed porosity; number of pores within the bed; wetted perimeter; and pore length. The only other factor that needed to be changed in equation 9 was the length term that arises from the surface area of the bed pores term ( $SA_{pores}$ ). This length term needed to be changed from a change in radial direction ( $\Delta r$ ) to change in height ( $\Delta z$ ) due to the construction of the static pressure vessel (Eq. 20).

$$F_{Drag} = C'_D \rho \vec{v}^2 \Delta z \quad (20)$$

The viscous work per wetted bed volume was then extrapolated from the Bernoulli's equation in the form of Eq. 21.

$$\Delta P + \rho_a g_c \Delta z = \dot{W} = F \times \vec{v} \quad (21)$$

This pressure relation to the work per unit bed volume (Eq. 21) was then equated to the sum of the forces through the simple knowledge that work is equal to force multiplied by distance. Therefore, the balanced equation came to be Eq. 22.

$$\Delta P + \rho_a g_c \Delta z = \frac{C'_D \rho_a \vec{v}^3}{\pi R^2} \quad (22)$$

Using this equation (Eq. 22) a correlation was drawn between the lumped drag coefficient and the velocity. This correlation was used to solve for the lumped drag coefficient, at the linear velocities in the centrifuge. Eq. 19 was then re-arranged to find the lumped drag coefficient ( $C'_D$ ) in terms of the linear velocity through the bed (Eq. 23).

$$\frac{\pi R^2 (\Delta P + \rho_a g_c \Delta z)}{\rho_a \vec{v}^3} = C'_D \quad (23)$$

This work term could also be re-worked using the MAP to find the max force that can be applied to the bed before deformation occurs.

## 3.2 Post-Homogenization Model

The other potential de-watering approach was to use an absorbent material to de-water the macerated mussel meat before freezing. However, an absorbent pad could increase the time taken to freeze the macerate because it adds an insulating layer between the macerate and the cold air of the freezer. The 6<sup>th</sup> constraint stated above in Section 1.4.2, expresses that the solution must not adversely affect the other plant processes. The absorbent material could be placed either on top of the macerate in the freezing tray, or between the macerate and the tray and left to absorb water while the macerated product traverses the tunnel freezer.

In addition, water will only transfer to the SAP layer in the liquid state, so it is critical to understand how long the liquid state is maintained at the surfaces of the freezing slab of the macerate. Therefore, the evaluation of the SAP and potential de-watering option requires that the heat transfer during the freezing process be better understood.

### 3.2.1 Post Homogenization Background

Macerate freezing was a process bottle neck at the factory. Adding a process step here that decreases the efficiency of the freezer would only increase the freezing times of the macerate, making the existing bottle neck worse. However, if enough water is removed it may prove to be a viable solution.

### *3.2.1.1 Mass Transfer Considerations*

The top layer option requires that the water works against the force of gravity, thus only having the chemical potential difference driving the water into the SAP. In the bottom layer solution gravity assists the water flow towards the SAP.

The first option is preferred where the SAP is added to the surface of the macerate. This option is preferred because the absorbent layer can be easily added to the top of the macerate and then is easily removed at the end of the freezing process. Whereas, if the second option is chosen then the removal of the absorbent layer becomes more difficult and labor intensive.

### *3.2.1.2 Heat Transfer Considerations*

The effectiveness of these two possible configurations, top or bottom of the macerate, also depended on which surface froze first, since ice cannot flow into the SAP. Therefore, an understanding of how the macerate froze and how the freezing process was affected by the addition of an SAP layer. The first option was to add an absorbent layer to the top of the macerate layer. This would impede the convective heat transfer between the top of the macerate and the air currents in the freezer, by introducing a resistive in between the air and the macerate surface. The second option, to add the absorbent layer on the bottom of the macerate, would leave the convective heat transfer between the surface of the macerate and the air currents, but it would introduce a new resistance layer between the metal tray and the macerate layers. Both options needed to be evaluated to see where the slowest heat transfer rate was.

### *3.2.1.3 Other Considerations*

The order of materials in the second option, from top to bottom, was macerate, absorbent layer, plastic lining, and metal tray. The second option requires personnel to separate the metal tray, plastic liner, and the absorbent material from the macerate and then re-apply the plastic layer and the macerate to the tray. Re-applying this plastic liner becomes unachievable, as the liner no longer adheres to the frozen surface of the macerate. It should be noted that the plastic liner is required to stay with the macerate slab until the freeze-drying process has been completed.

The heat transfer resistance is increased when a new layer is added to the system. Depending on the resistivity of the material that is added, this could significantly affect the heat transfer that is taking place. The current system needs to be simulated to determine the rate limiting resistance. This information will give grounds for an informed decision about where the absorbent material should go to least affect the freezing process.

## 3.2.2 Convective Heat Transfer Background

### *3.2.2.1 Coordinates and Assumptions of the Model*

The freezing of the macerate was modelled in terms of the cartesian coordinate system ( $x, y, z$  reference planes) (Fig. 8).

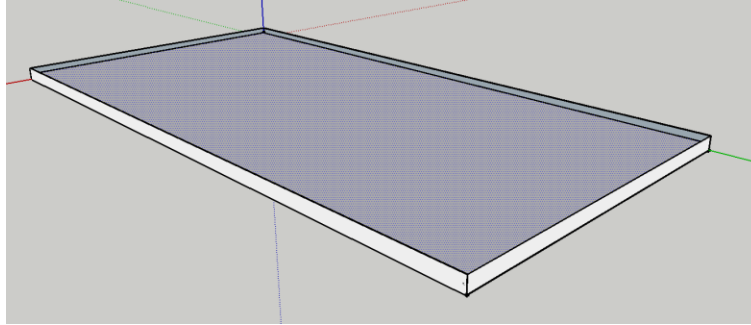


Figure 8 3D-Model of the Post-Homogenization System

Since the macerate layer was very thin in the z-direction, the model was simplified due to the changes in the x- and y-directions being much greater than that of the changes in the z direction. Therefore, the heat transfer flux was greatest over the z plane (Fig. 9) and was assumed negligible in the x and y directions. The one-dimensional model below (Figure 1) can be explained using conductive and convective heat transfer equations.

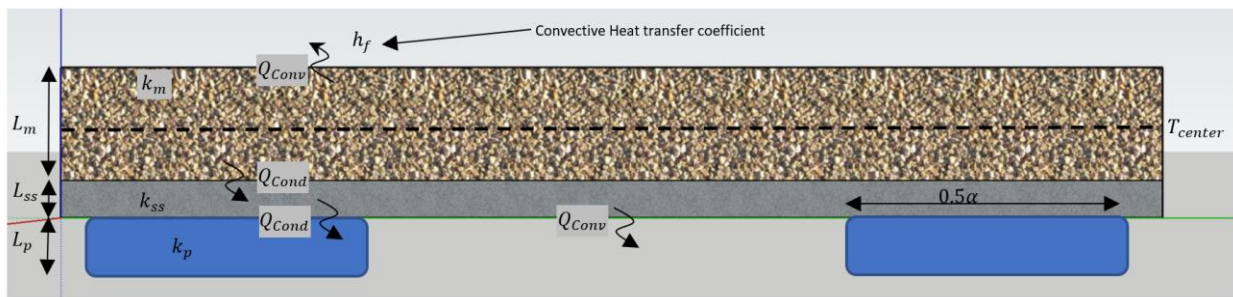


Figure 9 Model Setup with No Absorbent Layer

### 3.2.2.2 Steady-State Heat Transfer Resistance Model

For a wall that is composed of varying materials there are varying resistivities through each of the different materials. The equation that was used to describe heat flux ( $Q$ ) through a wall in terms of the temperature gradient ( $\Delta T$ ) and the resistivity ( $R$ ) can be seen below (Eq. 24):

$$Q = \frac{\Delta T}{R} \quad (24)$$

Where the resistivity seen above is analogous to the resistivity seen in electrical circuits. The overall resistance ( $R_o$ ) can be described by the resistivity of each of the materials that the wall is composed of.

$$\frac{1}{R_o} = \sum_n^i \frac{1}{R_i} \quad (25)$$

The resistivity of each material that makes up the wall is proportional to the thickness of the material ( $L$ ) and inversely proportional to the product of the thermal conductivity and the wall area as described in the equation below.

$$\frac{1}{R_{cond}} = \frac{k_i A}{L_i} \quad (26)$$

The problem space described above in Figure 9, shows a wall that is made from two different materials, mussel macerate and a metal tray. The initial problem was not dimensionally symmetrical due to the metal tray layer on one side and not the other. Conduction occurs through the bottom of the macerate and the through the metal tray which is then succeeded by convective transport through to the bulk media (air). This was then compared to the simple conduction through to the top of the macerate which was then followed by convective transport through to the bulk media (air). This problem space was later changed to accommodate an absorbent material on both the top of the macerate, and between the tray and macerate.

### 3.2.3 Convective Heat Transfer Background

The freezer was in a state of forced convection and the temperature was assumed to be constant in the bulk media (air). There were two places where convective heat transfer occurred. The first is on the top of the macerate slab to the air. The second was from the bottom of the metal tray to the air. The general convective heat transfer equation (Eq. 27) was similar to that of the conductive heat transfer.

$$Q = \frac{\Delta T}{R_{conv}} \quad (27)$$

Where the flux depends on the temperature gradient and the resistivity. For convection, the resistivity depends on the product of the boundary layer depth, the transfer coefficient ( $h_f$ ), and the contact area ( $A$ ).

$$\frac{1}{R_{conv}} = \frac{h_f A}{1} \quad (28)$$

### 3.2.4 Steady-State Heat Transfer Model without Absorbent Pad

The model needed to be split into two sections, the heat transfer from the macerate through to the top of the macerate (Eq. 29), and the heat transfer through the bottom of the macerate (Eq. 30). Where the heat transfer through the bottom of the macerate was written in terms of the overall resistivity before being broken into the heat transfer between the different layers.

$$Q_{Top} = \frac{\Delta T}{R_{oT}} \quad (29)$$

$$Q_{Bottom} = \frac{\Delta T}{R_{oB}} \quad (30)$$

The overall thermal resistivity through the bottom of the macerate was made up of the resistivity of the macerate ( $R_{mac}$ ), metal tray ( $R_{Tr}$ ), and the mixed resistivity term ( $R_M$ ) (Personal communication, 2018).

$$\frac{1}{R_{OB}} = \frac{1}{R_{mac}} + \frac{1}{R_{Tr}} + \frac{1}{R_m} \quad (31)$$

The mixed resistivity term is made up of a combination of conductive and convective heat transfer. A portion of the bottom of the metal tray sits on plastic belts and the rest of the tray is in contact with the air in the tunnel. This means that the resistivity over this surface needs to be modelled using the proportionality ( $\alpha$ ) of the occurring conductive and convective heat transfer, as described by the equation below.

$$\frac{1}{R_m} = \frac{\alpha}{R_{conv}} + \frac{(1-\alpha)}{R_{cond}} \quad (32)$$

The overall thermal resistivity through the top of the macerate was defined as the summation of the thermal resistance through the macerate ( $R_m$ ) and the convective thermal resistance between the top of the macerate and the air ( $R_A$ ).

$$\frac{1}{R_{OB}} = \frac{1}{R_m} + \frac{1}{R_A} \quad (33)$$

The resistivity terms of each material were broken down further so that the equation was in terms of the thermal conductivity. The thermal conductivity for most common materials, such as metals, air, plastic, and ceramic can be found using an online source. Whereas the thermal conductivity of the macerate had to be found through experimental testing as it was a mixture of mussel biomass and water.

At the equilibrium point within the macerate, which was defined as the point where the two differing temperature gradients meet in the macerate, the heat flux through the top of the macerate ( $Q_{Top}$ ) would be equal to the heat flux through the bottom of the macerate ( $Q_{Bottom}$ ). The heat transfer equilibrium equation (Eq. 34) shows the two equated fluxes and the expanded versions of the resistances.

$$\frac{\Delta T}{\left[ \frac{L_{mT}}{k_m A} + \frac{1}{h_f A} \right]} = \frac{\Delta T}{\left[ \frac{L_{mB}}{k_m A} + \frac{L_{SS}}{k_{SS} A} + \left( \alpha \frac{L_p}{k_p A} + \frac{(1-\alpha)}{h_f A} \right) \right]} \quad (34)$$

This heat transfer equilibrium equation contains 11 variables with the majority of them being unknown. A degree of freedom analysis was conducted (Table 2) to define some of the variables in the heat transfer equilibrium equation. The analytical method chosen showed that the system is poorly defined. With the help of a literature search and experimentation, to define some of the unknowns the system could be solved.

Table 2 Degree of Freedom Analysis (DOF)

Variable {TEXT}	Symbol {VAR}	Known [Y/N]	Lit. Search [Y/N]	Experimental [Y/N]	Citation {TEXT}
Thermal Conductivity <sub>Macerate</sub>	$k_m$	N	Y	N	(Sharqawy, 2012)
Thermal Conductivity <sub>Stainless Steel</sub>	$k_{SS}$	N	Y	N	(Sweet, Roth, & Moss, 1987)
Thermal Conductivity <sub>Plastic</sub>	$k_p$	N	Y	N	(Rides, et al., 2009)
Temperature Differential	$\Delta T$	Y	N	N	-
Depth of Macerate <sub>Top</sub>	$L_{mT}$	N	N	Y	-

Depth of Macerate <sub>Bottom</sub>	$L_{mB}$	N	N	Y	-
Overall Macerate Depth	$L_0$	Y	N	N	-
Plastic Thickness	$L_p$	Y	N	N	-
Heat Transfer Coefficient	$h_f$	N	Y	N	(Toolbox, Convective Heat Transfer, 2019)
Proportionality Constant	$\alpha$	Y	N	N	-
Cross Sectional Area	$A$	Y	N	N	-

Literature Search		
Totals:	Without	With
Unknowns	6	2
Number of Relations	1	1
Number of Equations	1	1
Summation	4	0

The thermal conductivity of the macerate was expected to change as the temperature within the macerate changed. To simplify the problem, it was assumed that the temperature range that will be used for this study (10 °C to -10°C) would not provide a significant change to the thermal conductivity. Another factor that was considered was the starting point for the thermal conductivity when fitting the model to the empirical data. It was assumed that the thermal conductivity would be similar to that of water, considering that the macerate contained around 80% water. The initial values for the thermal conductivity of the liquid and frozen macerate were chosen to be 0.578 and 2.18 W m<sup>-1</sup> K<sup>-1</sup> respectively (Toolbox, Water - Thermal Conductivity, 19).

The experimental procedure that was followed to obtain the equilibrium point within the macerate, is discussed in further detail in Section 4.2 . Once the equilibrium point within the macerate had been found, the equations stated above were modified to consider the presence of an absorbent pad on either or both of sides of the macerate.

### 3.2.5 Steady-State Heat Transfer Model with Absorbent Pad

The heat transfer model that includes the absorbent pad was remarkably similar to the model stated in Section 3.2.4 . There was an equilibrium point within the macerate which was defined as the last point that the macerate freezes. This equilibrium point should differ to that of the aforementioned heat transfer experimentation, with no absorbent pad, due to the different thermal fluxes within each model.

To account for the insulative properties of the absorbent pad either the top side or bottom side flux equation was modified, depending on where the pad was being placed. The resistivity term for the absorbent pad was added to the overall resistivity term ( $R_o$ ) therefore changing the balanced flux equation (Eq 34) to either Eq 35 or Eq 36 seen below, if the absorbent pad were added to the top or the bottom of the macerate respectively.

$$\frac{\Delta T}{\left[\frac{L_{mT}}{k_m A} + \frac{1}{h_f A}\right]} = \frac{\Delta T}{\left[\frac{L_{mB}}{k_m A} + \frac{L_{SS}}{k_{SS} A} + \left(\alpha \frac{L_p}{k_p A} + \frac{(1-\alpha)}{h_f A}\right) + \frac{L_{AB}}{k_{Ab} A}\right]} \quad (35)$$

$$\frac{\Delta T}{\left[\frac{L_{mT}}{k_m A} + \frac{1}{h_f A} + \frac{L_{AB}}{k_{Ab}}\right]} = \frac{\Delta T}{\left[\frac{L_{mB}}{k_m A} + \frac{L_{SS}}{k_{SS} A} + \left(\alpha \frac{L_P}{k_p A} + \frac{(1-\alpha)}{h_f A}\right)\right]} \quad (36)$$

With water being removed from the product, the thermal conductivity of the macerate will differ to the value seen in the experiments with no absorbent layer. As a first approximation it was assumed that the thermal conductivity of the macerate was constant. This equation set also assumes that the system is at steady state, whereas the system seen during processing was transient. This means that the model seen above should only be used to estimate the position of the thermal center within the macerate.

The thermal conductivity of the absorbent was assumed to be similar to that of the macerate, in the manner that the thermal conductivity of the absorbent was expected to change with respect to both water content and temperature.

### 3.2.6 Dynamic Mathematical Heat Transfer Solution

The steady-state model provides an estimate of the cooling effect on the macerate, but the problem of cooling and freezing the macerate layer is a transient problem. Since the slab freezes from the top/bottom edges inward, the effect on freezing time required a transient solution. In order to find the thermal conductivity of the macerate and therefore solve the steady state equation described in the previous section, a dynamic model of the freezing of the macerate was created. This dynamic model was created so that it could be fitted to the empirical data to find the thermal conductivity of the macerate. This dynamic model had to contain the thermal conductivity of the macerate as a variable. To start the dynamic model a shell energy balance was used (B & Chu, 1959) .

$$\begin{aligned} \rho C_p \left( \frac{\partial T}{\partial t} + v_x \frac{\partial T}{\partial x} + v_y \frac{\partial T}{\partial y} + v_z \frac{\partial T}{\partial z} \right) \\ = k \left[ \frac{\partial^2 T}{\partial x^2} + \frac{\partial^2 T}{\partial y^2} + \frac{\partial^2 T}{\partial z^2} \right] + 2\mu \left\{ \left( \frac{\partial v_x}{\partial x} \right)^2 + \left( \frac{\partial v_y}{\partial y} \right)^2 + \left( \frac{\partial v_z}{\partial z} \right)^2 \right\} \\ + \mu \left\{ \left( \frac{\partial v_x}{\partial y} + \frac{\partial v_y}{\partial x} \right)^2 + \left( \frac{\partial v_x}{\partial z} + \frac{\partial v_z}{\partial x} \right)^2 + \left( \frac{\partial v_y}{\partial z} + \frac{\partial v_z}{\partial y} \right)^2 \right\} + Generation \end{aligned} \quad (37)$$

The temperature change over time at any given  $x, y, z$  coordinate could be described by the sum of the flux in each of the three dimensions, intra or inter-dimensional mixing of the fluid and a generation term. To simplify the problem; it was assumed that there was no mixing within the macerate, therefore the intra and inter-dimensional mixing terms were nullified along with the velocities and velocity gradients; the  $x$  and  $y$  dimensions were significantly greater than the  $z$  dimension, therefore the fluxes in these dimensions were also neglected. It was important to keep the generation term within the equation as this was used to describe any heat generation or consumption associated with phase change. With these assumptions the simplified differential equation was written as,

$$\frac{\partial T}{\partial t} = \frac{k}{\rho C_p} \left( \frac{\partial^2 T}{\partial z^2} + Generation \right) \quad (38)$$

Using a central difference approach gives the following equations for the numerical solution:

$$T'(t) = \frac{k}{\rho C_p} (T''(z) + Gen) \quad (39)$$

$$T'_i(t) = \frac{k}{\rho C_p} \left( \frac{T(z_{i+1}) - 2T(z_i) + T(z_{i-1}))}{\Delta z^2} + Gen \right) \quad (40)$$

$$T(t_{i+1}) = T(t_i) + \Delta t T'_i(t) \quad (41)$$

The assumed boundary conditions (BC's) were:

- Symmetry BC: no heat was transferred across the thermal center of the macerate. This is to say that this model assumes the thermal flux about some thermal equilibrium point near the center of the slab is zero. Therefore, no heat can be transferred across this center boundary:

$$\frac{\partial T}{\partial z} = 0 @ z_{equilibrium} \text{ for all } t \quad (42)$$

- Flux BC at the interfacial surface: the conductive flux on the inside of the macerate must be equal to the convective flux entering the bulk media therefore,

$$q_{convection} = q_{conduction} \quad (43)$$

$$k \frac{\partial T}{\partial z} = h(T_{mac} - T_{Bulk}) @ \text{all interfacial areas for all } t$$

In conjunction with the BC's, there was also the initial condition that states that the starting temperature across the entirety of the macerate is 14°C,

$$T_{mac} = 14^\circ\text{C} @ t = 0 \quad (44)$$

All this information was enough to solve the numerical integration and produce a simulation of the current system.

The generation term that was mentioned, was used to describe the heat that was generated when the liquid macerate froze into a solid. This generation term was comprised of the ratio of the latent heat of fusion of water,  $\Delta H_{fus}$ , and the specific heat capacity of water,  $C_p$ .

$$Gen = \frac{\Delta H_{fus}}{C_p} \quad (45)$$

This generation term was only implemented once the simulated temperature had reached the freezing temperature of the macerate. This freezing temperature was estimated using the empirical data shown in Chapter 5. The modifications that were made to simulate the dynamic heat transfer through the bottom of the macerate are explained in the following section.

### 3.2.7 Dynamic Mathematical Heat Transfer Solution (Bottom)

The numerical solution as seen by the bottom of the macerate was written in a similar manner to the top solution, although the thermal conductivity needed to be written in terms of the overall thermal conductivity. This overall thermal conductivity ( $k_o$ ) considered the thermal conductivity of the stainless

steel, plastic chains that are in contact with the stainless-steel tray and absorbent when it was added to the system.

$$\frac{\partial T}{\partial t} = \frac{k_0}{\rho C_p} \frac{\partial^2 T}{\partial z^2} \quad (46)$$

Again, using the central difference approach the following equation set was given:

$$T'(t) = \frac{k_0}{\rho C_p} (T''(z) + Gen) \quad (47)$$

$$T'_i(t) = \frac{k_0}{\rho C_p} \left( \frac{T(z_{i+1}) - 2T(z_i) + T(z_{i-1}))}{\Delta z^2} + Gen \right) \quad (48)$$

$$T(t_{i+1}) = T(t_i) + \Delta t T'_i(t) \quad (49)$$

The dynamic mathematical model for the addition of the SAP used the same theory stated in this section, although the thermal conductivity of the SAP was incorporated into the overall thermal conductivity term ( $k_0$ ). The full *MATLAB* implementation for both the top and bottom simulations with and without the absorbent pad can be seen under Appendix 8.4 .

### 3.2.8 Frozen Front Propagation

The cooling of the liquid macerate needed to be accompanied by the propagation of the frozen front through the macerate. Once the liquid macerate had cooled to the freezing point the macerate began to freeze. The freezing of the macerate generated heat, which was associated with the phase change from liquid to solid and commonly referred to as the latent heat of fusion. This generation term as well as the change in thermal conductivity of the frozen macerate was added to the equation set in Section 3.2.7 after the freezing temperature had been met. The macerate was defined as frozen when the frozen fronts from the top and bottom of the macerate met.

## Chapter 4 Materials and Methods

As previously described, this investigation was broken up into two portions, pre- and post-homogenization. Modeling the pre-homogenization system (Section 3.1 ), centrifugation, showed that the lumped drag coefficient ( $C'_D$ ) had to be empirically determined before committing to a centrifuge design. The main key factor that needed to be experimentally investigated was, the pressure or drag force on the mussels at which percolation ceases. Optimizing the centrifuge design required that the lumped drag coefficient be determined as a function of the average bed velocity. This correlation was accomplished by modeling the flow of water through a static bed of mussels (Section 3.1.6 ).

### 4.1 Pre-Homogenization Experimentation

The apparatus design had to incorporate all the features that allow for sound experimental testing and produce reliable measurements of the required variables. One of the key design concepts that needed to be considered and discussed was the aspect ratio of the pressure cylinder.

The aspect ratio of the pressure cylinder was defined as the ratio of the Diameter of the cylinder ( $D$ ) to the depth of the bed ( $z$ ) (Eq. 50).

$$A_R = \frac{D}{z} \quad (50)$$

The aspect ratio of the pressure cylinder needed to be large so that the wall friction effects could be negated (Yang & Daido, 1993). To achieve this large aspect ratio the diameter of the cylinder needed to be at least three times greater than the depth of the bed ( $D \geq 3z$ ) (Zangar, 1953) . Before the aspect ratio could be defined the maximum bed-height had to be defined, as this bed height explicitly defined the diameter and thus the volume of the vessel. The maximum bed height was set at 0.15 m, giving a vessel diameter of 0.45 m.

The fixed bed apparatus (Figure 11) contained pressure sensors (P-101/102, Manufacturer: Wika, Model: 213.53.063) before and after the bed of mussels in order to obtain the pressure drop across the bed. The inlet was equipped with a pressure regulator (V-101, Manufacturer: Hansen, Model: 3/4"), so that the applied pressure to the bed could be manipulated. A 5L jug and timer was used to procure the volumetric flow of the fluid leaving the bed. The vessel was sealed to ensure against leaks and a flow disperser was added to the top of the bed to distribute the flow evenly across the bed (Figure 10).

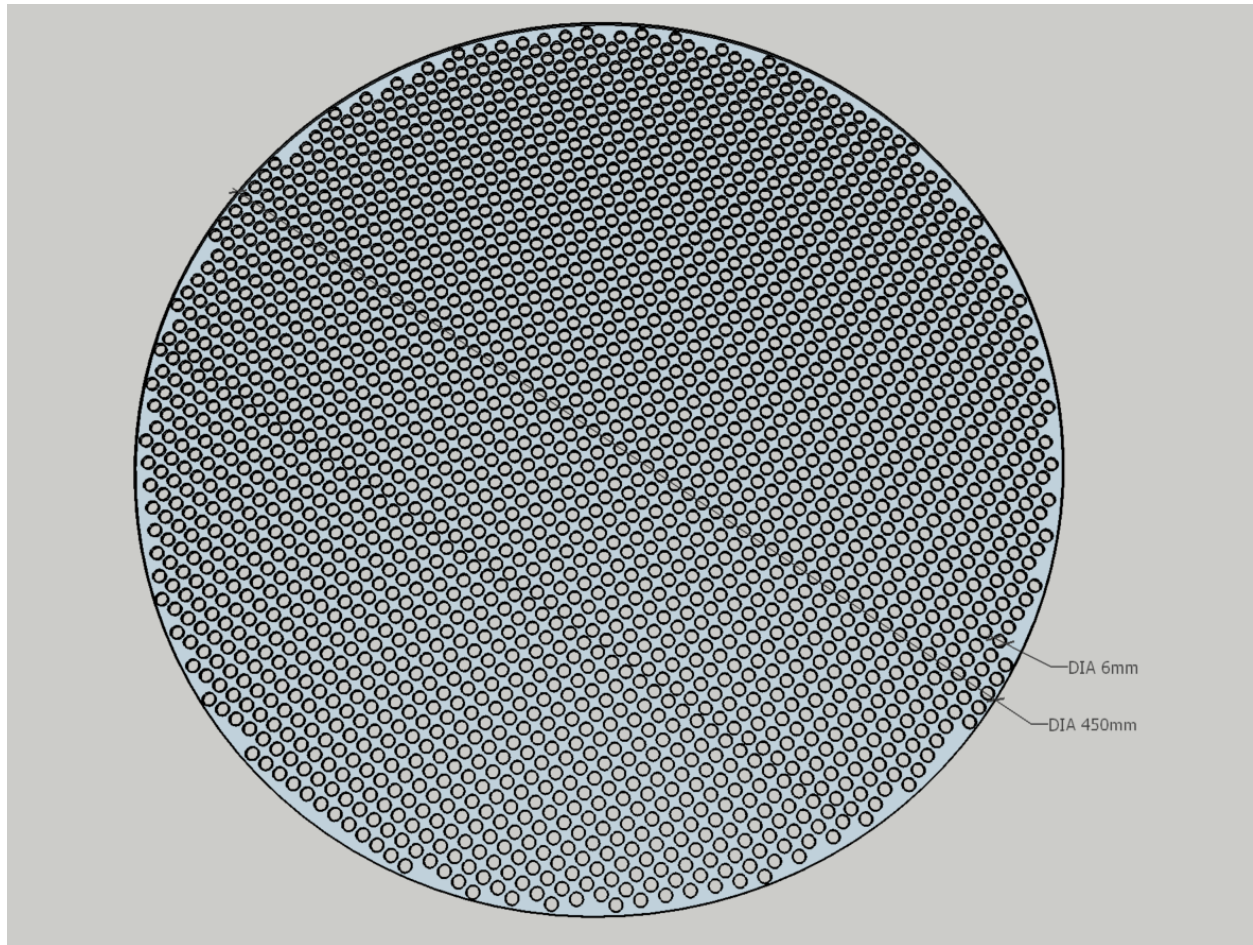


*Figure 10 Dispersion Plate Made from 3 mm Stainless Plate*

The container was constructed from clear Perspex (15 mm thick and custom built by Nelson Plastics Ltd), so that the change in height of the mussel bed could be seen. A valved bypass system, which allowed the vessel to be filled with water from the bottom of the vessel to the top (V-102/103) was included so that no air bubbles were trapped inside the bed at the start of the experiment. Any trapped air could cause a variation in the compressibility and thus, vary the experimental results. A line diagram of the experimental setup is shown in Fig. 11.

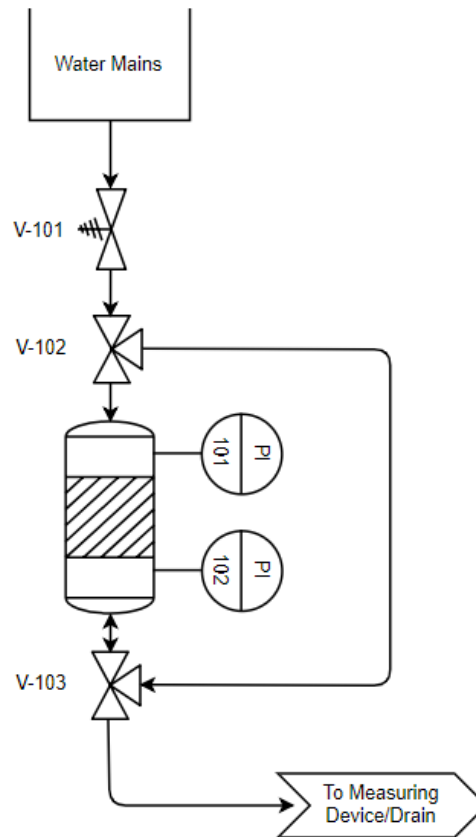


Figure 11 Basic Line Diagram of the Static Bed Apparatus

The pressures at the top and bottom of the bed, the flow rate at the exit, and the height of the mussel bed were measured on each run, once steady-state flow was established. The volumetric flow rate was adjusted by the pressure regulator between runs.

Due to budget constraints the system drawn out in Figure 11 was slightly different to that of the actual experimental setup. The differing points were that the pressure regulating device was a manually operated ball valve; and the water supply was taken directly from the factory supply. There were some issues with these changes that ultimately led to the catastrophic failure of the pressure vessel, which are discussed later in Section 6.1 .

#### 4.1.1 Static Bed Experimental Procedure

##### 4.1.1.1 Priming the System

Following the nomenclature on Figure 11 each experiment consisted of the following steps:

- 1) The bed was connected to the plant main water supply.
- 2) V-103 was positioned so that there was no flow going to the drain and V-102 positioned so that water filled the vessel from the bottom to the top.
- 3) A known mass of fresh deshelled mussels ( $m_M$ ) was loaded into the pressure vessel and the initial bed height ( $z_0$ ) was recorded.

- 4) The vessel was then filled from the bottom to the top. The filling operation was conducted with the top of the pressure vessel on loosely allowing the air to escape.
- 5) Once the vessel was full, the top was tightened to form a watertight seal.
- 6) The remaining air in V-102 was displaced with water by:
  - a. Removing V-102 from the plant main and filling the piping to the vessel and the valve itself with water from a jug.
  - b. Reconnecting V-102 to the mains and positioning V-102 and V-103 so that the water can flow direct to the drain, skipping the pressure vessel.
  - c. Water was then run until the piping above V-102 and V-102 was primed.
- 7) The position of the two three-way valves were then changed so that the water flows from the top of the vessel to the bottom and out to the measuring device.

At this point the static bed system was primed and ready for experimentation.

#### 4.1.1.2 *Experimental Run*

The applied pressure was adjusted to a fixed value between 0 and 110 kPa<sub>g</sub>, or until the maximum fluid velocity was met, in increments of 10 kPa. This pressure change was achieved by manipulating the pressure regulating valve (V-101). To allow the system to reach steady state, the apparatus was left to run for a minimum of one minute. After this, the flow rate was measured, and the apparatus was left for another minute. After the second minute had passed the flow rate was measured again. If the first and second flow rates were the same, the system was assumed to have reached steady state and the fluid velocity and pressure drop over the bed was recorded. If the two flow rate measurements did not agree, then the system was left for another minute and the flow rate was measured again, this process was repeated until the system had reached steady state. The data was recorded on the template shown in Section 8.1.3 of the Appendix.

## 4.2 Post-Homogenization Experimental Design

The post-homogenization alternative was to use a layer of superabsorbent polymer (SAP). The questions left to be resolved were: 1) which configuration (SAP on top or SAP on the bottom) provided the best absorption, and 2) how much the SAP layer affected the time to freeze. To accomplish this the freezing dynamics of the macerate needed to be recorded to find the conductivity and the freezing point of the macerate. An empirical estimate of the thermal conductivity for the macerate decreased the number of unknowns in the model, making it solvable. Finding the thermal center of the macerate also gave a current baseline from which to measure the impact of the SAP.

Empirical testing of the SAP was required to measure how much water was absorbed by the SAP before the onset of freezing and if any oil was entrained in the SAP during absorption.

These key factors were investigated using the following methodologies.

#### 4.2.1 Transient Temperature of the Macerate

Temperature measurements were taken using two *Multitrip Straight Probe Logger*. The probes themselves, had 30 mm of exposed probe, a probe diameter of 3 mm, and could store 7,935 data points at two second intervals (TempRecord, 2018). The smallest probe circumference was needed due to the thickness of the slurry being exceedingly small (12 mm) thus, enabling precise localization of the measurement at specific depths.

The issue of fixing the probe depth was overcome using a support to hold the probe at a fixed height within the macerate. Some of the factors that were considered when designing the probe support were:

- Thermal influence on the system. This was the effect that the support will have on the thermal flux through the macerate. E.g. if the support were made from metal or another thermally conductive material then the heat would readily leave the macerate through this conductor, therefore changing the thermodynamics of the system.
- Distance from the support to the probe. If the probe were far from the support, there would be less thermal interference to the readings due to the support.
- Important heights within the macerate. There were three important areas within the thermal system, which were the interface where the macerate and the tray meet; the interface between the top of the macerate and the air; and the center of the macerate. The two interface areas are important because they will give empirical data that was used to calculate the thermal conductivity of the macerate. The center point of the macerate is important as this empirically validates any claims on where the equilibrium point may be.

The final design that was chosen for the temperature probe support is shown in Figure 12 . Alternatives considered and discarded are shown in the Appendix section (Section 8.3 ). This design was chosen because it minimized the thermal interference from the support. There is no base plate, which means that the system is as close to the standard tray design as possible. There are negligible effects from vertical portion of the support as only 8 mm of the probe is supported, leaving 22 mm of the probe extended into the macerate. The horizontal portions of the support are located far away from the measuring area, mitigating the thermal effects of this structure.

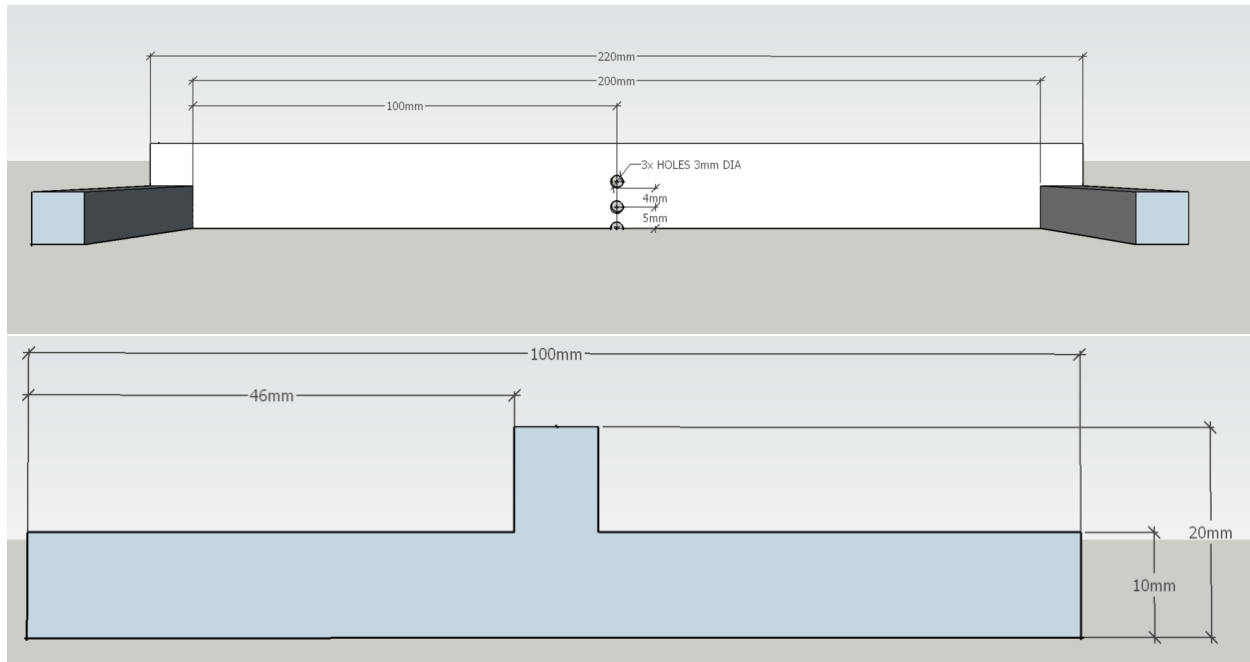


Figure 12 Probe Support Side View (Bottom) and Front View (Top)

This support was placed in the center of the tray to help keep the temperature probes fixed in place during the freezing process. Probes were placed at the top and bottom of the macerate layer

#### 4.2.2 Fitting the Transient Model to Obtain $k$

As the interfacial thermal profiles were measured over time the macerate conductivity was optimized such that the error between the model and empirical results were minimized. As the temperature change was small, a constant conductivity was assumed. The dynamic heat transfer model was fitted to the two known interfacial thermal profiles in order to find an empirical value for the thermal conductivity of the macerate. This in turn, made the steady-state equation solvable and mathematically exposed where the thermal center of the macerate lay. Initially, the cooling model was fitted to the empirical data, by changing the thermal conductivity of the liquid macerate in the model. Then the freezing model was fitted to the empirical freezing data via the same method. The initial guess was that the thermal conductivity of the macerate would be something similar to that of the conductivity of water.

#### 4.2.3 SAP Choice

Tests were conducted on some different products obtained from the *Sirane* (U.K) absorbent product line. One product contained a sodium acrylate SAP encased in a plastic sleeve where one side of the sleeve was perforated to allow for mass transfer; and another product was a food safe SAP bonded with a sturdy backbone material that can contact the macerate directly. In the end this food safe SAP that was bonded to a sturdy backbone (*Dri-Fresh*, In-Flex pad, (Sirane, Dri-Fresh Absorbent Meat Pads, 2020)) was chosen as it absorbed fluid much faster than the other sleeved option. Since the SAPs were supplied in 0.5x0.6m pads, this allowed for each tray to have half of the tray covered by the SAP and the other half of the tray worked as a control. Therefore, every SAP tested tray contained the SAP treated macerate as well as a

control sample. One of the detriments of testing in this manner is the possibility of the oil within the macerate diffusing to the low concentration areas of the macerate (areas close to the SAP), assuming that the SAP has an affinity towards the oil portion of the macerate. It had been assured that the SAP being used in this study had no affinity to oils or fats, it was designed with a specific affinity towards water (Sirane, Dri-Fresh, 2018).

#### 4.2.4 Effect of the SAP on Cooling and Freezing

Determination of the thermal center influenced the placement of the SAP layer. This layer needed to be placed so that it had the least impact on the freezing of the macerate. Since the macerate froze from the top and the bottom surfaces in towards the center, the position of any shift in the thermal center away from the SAP was an indication of increased heat transfer resistance by the SAP. Not only did the resistivity of the system change, but the thermal conductivity of the macerate, thermal center and the SAP was also expected to change with the addition of the SAP. It was hypothesized that the thermal conductivity of the macerate and the SAP would change as a function of water content as the water moved from the macerate to the SAP.

Therefore, trying to model all these changes accurately at any given point in time was deemed to be unfeasible, and an empirical measurement element was required. Instead of having a variable model for the thermal conductivity of the macerate and SAP, it was assumed that the SAP thermal conductivity was constant. The fitted mathematical model was the average change seen in both the macerate and the SAP. In order to adequately compare the non-SAP system to the SAP system, the deviations between the two systems needed to be understood.

The methodology used to solve the now unknown thermal conductivity of the macerate was very similar to the methodology used to find the initial thermal profiles at the interfacial points, with the only variations being the addition of the SAP in the model and the placement of the temperature probes. The probes were placed at the interfacial regions of the macerate.

Once the thermal conductivities were found the dynamic heat transfer models were used to predict where the thermal center of the macerate was. The dynamic heat transfer was plotted from the top and the bottom of the macerate to the thermal center, where these two plots first overlapped. This means that the model is only effective until the thermal center is reached by the frozen front.

#### 4.2.5 Water Removal by the SAP

Water entrainment by the SAP was determined gravimetrically. The SAP was weighed before contact with the liquid macerate and after removing it from the macerate after the freezing process. The difference was assumed to be water removed from the macerate. The weight was measured using an ATEC NHB-600M for the initial weight measurements and an ATEC NHB-3000M was used to measure the final weight of the SAP. Two separate scales had to be used to cover the increase in weight.

#### 4.2.6 Oil Removal by the SAP

The mussel oil content of the SAP was indirectly determined by testing the control portion of the macerate. This control portion had not directly contacted the SAP. The control and test portions of the macerate were dried and then sent to an external testing facility (Cawthron Institute). It was standard practice to test the FFA (Free Fatty Acid) and TFA (Total Fatty Acid) content of the dried macerate to give an indication of the oil present within the macerate.

## Chapter 5 Experimental Results

The flow of water through either of the bed types, static or centrifugal, had flow characteristics that were analogous to a Moody Diagram. Where the friction factor is given relative to the fluid flow within the bed. The lumped drag coefficient used in this report was expected to trend similar to a moody plot relative to the fluid velocity through the bed. It was expected that the lumped drag coefficient would show linearity when compared to the fluid velocity through the bed on a log-log plot. This trend was expected to be persistent until the flow pattern became turbulent at which time the pores within the bed were expected to start reducing as the bed became compressed. This reduction in pore size within the bed reduced the fluid velocity through the bed and was expected to continue until the pores no longer allowed water to pass through them, making the bed impermeable.

The fluid velocity reached a maximum just before the bed began to compress and restrict flow. This was why the maximum pressure drop (MAP) and lumped drag coefficient ( $C'_D$ ) needed to be determined before a centrifuge could be designed.

### 5.1 Centrifuge Design

#### 5.1.1 Maximum Pressure Drop (MAP) and Lumped Drag Coefficient Determination ( $C'_D$ )

The experimentation surrounding the pre-homogenization method was aimed at finding the pressure at which the pores within the mussel bed closed due to deformation. This MAP was then used as a design parameter for designing a centrifuge. It was expected that the fluid velocity through the bed would increase up until the bed starts to deform. At this deformation point, any further increases in applied pressure would result in a reduction of the fluid velocity. The fluid was assumed to continue to decrease until the bed becomes impermeable to water.

#### 5.1.2 Preliminary Results

The initial data collected showed a linear trend: as the pressure was increased the fluid velocity also increased (Figure 13). When the pressure reached 80 kPa the fluid velocity began to reduce quickly at each 10 kPa interval. There was some variability seen between the data points at each of the pressure increments. This variation came from a few different factors.

The first variation factor was the supply pressure. The water supply for this experiment came directly from the factory water supply. This led to some variation in the pressure measurement as well as the velocity measurement.

The other variation was in the measuring of the volumetric flowrate. The time to fill the measurement vessel was taken by hand which incurs human error in both the time measurement as well as the volume measurement. These factors resulted in both variations between experiments as well as variation between data points within the same experiment.

The data collected from these several experiments varied quite significantly. At the maximum there was a variation of  $9 \times 10^{-4} \text{ ms}^{-1}$  between experimental data sets, which was seen at the 70 kPa mark.

Some of the variance seen in the plot below (Figure 13) can be attributed to the use of varying grades (sizes) of mussels, which changed the flow characteristics. Some were due to the fluctuations in the water supply due to parallel plant demands on this supply. This is shown in Figure 13 as the difference between the blue and the green markers. The solid blue markers consist of uncontrolled mussel size and the green markers consist purely of grade D mussels.

The fluctuations in the water supply were mitigated by running the experiments while the majority of the water consuming machinery was not in use. While this lessened the impact of the supply fluctuations there were still a number of items that consume water throughout the day.

The measurement errors were mitigated by taking the volumetric flowrate reading three times and then averaging them. This meant that there was more time spent at each data point and the fluctuations from the supply would have had an increased effect.

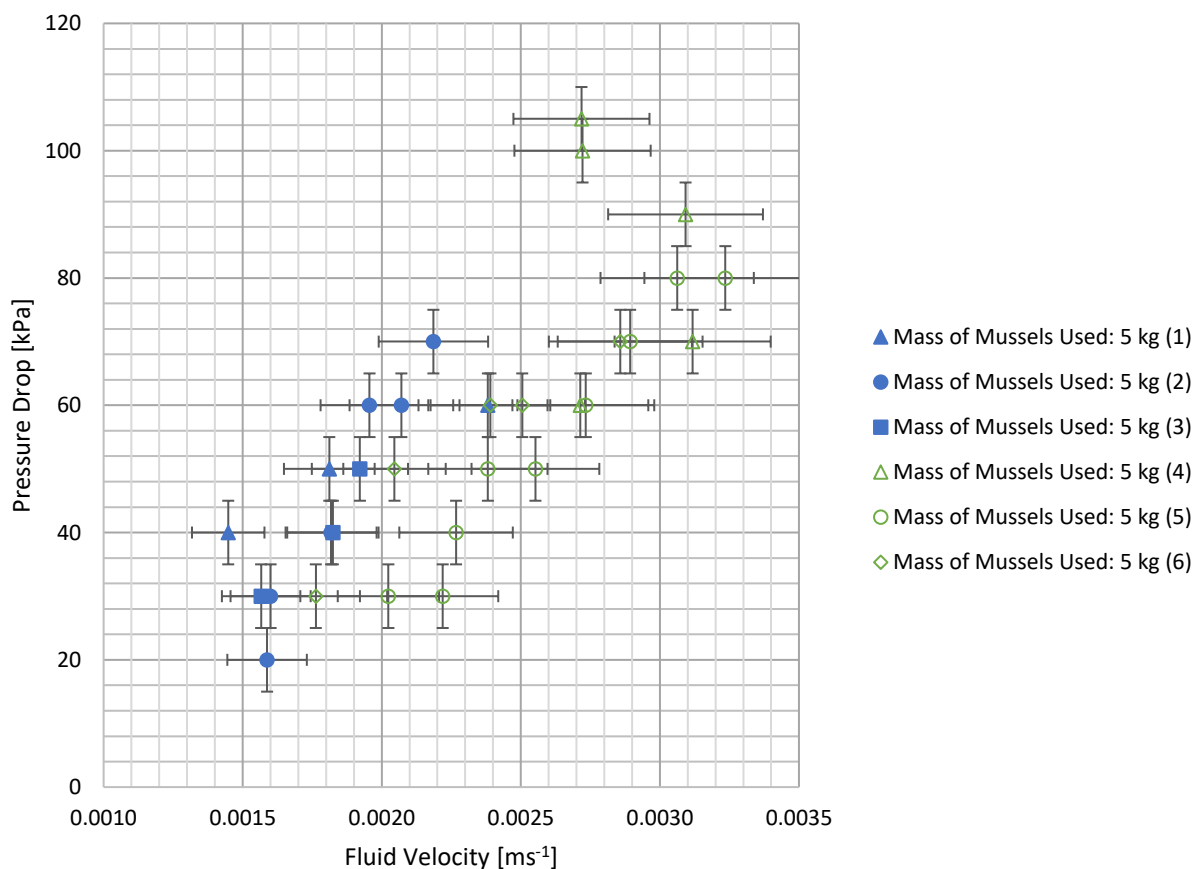


Figure 13 Static Bed Experimental Results

The trends best fit functions ranged from linear to exponential to power trends. This change in trend types between the differing data sets could be attributed to both the varying mussel grades used as well as the variation in water supply. The greatest pressure achieved in the vessel, prior to catastrophic failure, was 105 kPa. Unfortunately, this pressure was only achieved over one data set and not repeated due to structural failure of the test vessel.

### 5.1.2.1 Controlled Experiments

After the realization that the changing mussel size was impacting the consistency of the results the grade of mussels was kept as constant as possible, by selecting only grade D mussels. The smallest grade of mussels, grade D, was chosen to be run in the static pressure vessel over experiments 4, 5 and 6 (Figure 14). As seen on Figure 14 below, the repeatability of the experimental results increased, with the maximum variation between data points decreasing to  $5 \times 10^{-4} \text{ m s}^{-1}$ , which is approximately half of the variability seen in the uncontrolled data set.

Limiting the work to the grade D mussels and after plant operational hours, the experimental range was increased to higher pressures in order to find the MAP. The pressure at which the pores within the static bed start to close is  $80 \pm 5 \text{ kPa}$ . At this pressure, the water velocity stagnated at  $80 \pm 5 \text{ kPa}$  and started to decrease above this stagnation point, indicating that the increased pressure was causing the pores within the bed to close. These higher pressures were only achieved once before vessel failure occurred.

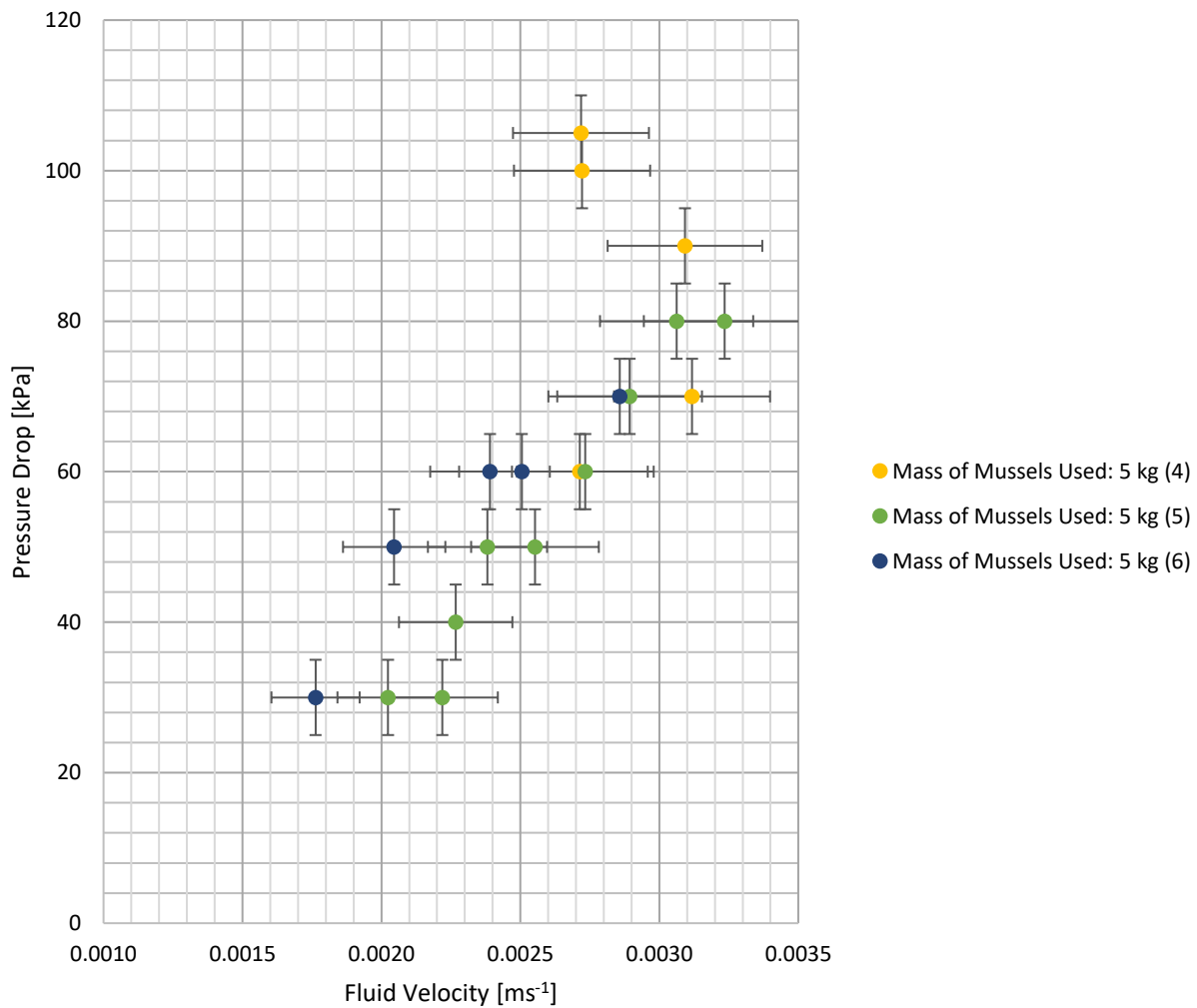


Figure 14 Reliable Static Bed Experimental Results

This data suggests that the MAP within a bed of mussels, all of grade D size, is approximated to  $80 \pm 5$  kPa. The MAP was then used as a design parameter for the centrifuge for the centrifugal and viscous calculations. The total force acting on the bed of mussels, which is the summation of the centrifugal and viscous drag forces, both need to summate to the MAP (80 kPa). Using the simple relation that is equal to force divided by area, this MAP can be converted to a maximum force. This maximum force value came out to be 12.72 kN. Before any other calculations can be completed the centrifuge must have defined dimensions, inner/outer and bed height. These three length dimensions will be denoted as the primary dimensions in the following section.

#### 5.1.2.2 Pressure Drop as a Function of Bed Velocity

It was initially assumed that the mussels would act as an incompressible medium through the lower pressure stages of the static bed experiments and would only transition to a compressible bed once the pressure was great enough to reduce the flow rate. This assumption was tested and proved to be incorrect by comparison with Carman's correlation for laminar gas flow through ridged porous media (Carman, 1956) that can be seen in the equation below (Eq. 51).

$$-\frac{\Delta P}{L} = 180 \frac{\mu v_b (1 - \epsilon_b)^2}{\Phi_s^2 2R_p^2 \epsilon_b^3} \quad (51)$$

The sphericity factor ( $\Phi_s$ ) and bed porosity ( $\epsilon_b$ ) were unknown for the mussels. The bed porosity was approximated by placing 30 mm worth of mussels into a measuring jug and then filling the jug with known quantities of water until the water level meets the top of the mussels. This gave a bed porosity of 42%.

The sphericity factor was determined by fitting the equation to a single empirical point (0.0018, 1000) and was found to be 0.0082. This shows that the mussels are not sphere like in nature. The resulting correlation deviates from the experimental data significantly (Figure 15). This would imply that the static bed was operating outside of the constraints of the Carman equation (Eq. 51). It is not clear if the deviation is due to the mussels compressing as soon as pressure is applied to the bed. With this compression at low pressure levels it is also assumed that the flow regime changes from laminar, at low pressure ( $\frac{\Delta P}{L} < 1500 \text{ kPa m}^{-1}$ ), to turbulent after pressure is applied.

Another factor that could have influenced deviation is the fact that the Carman equation (Eq. 51) was designed for particulate material in the micron range, whereas this project used particulates in the cm range.

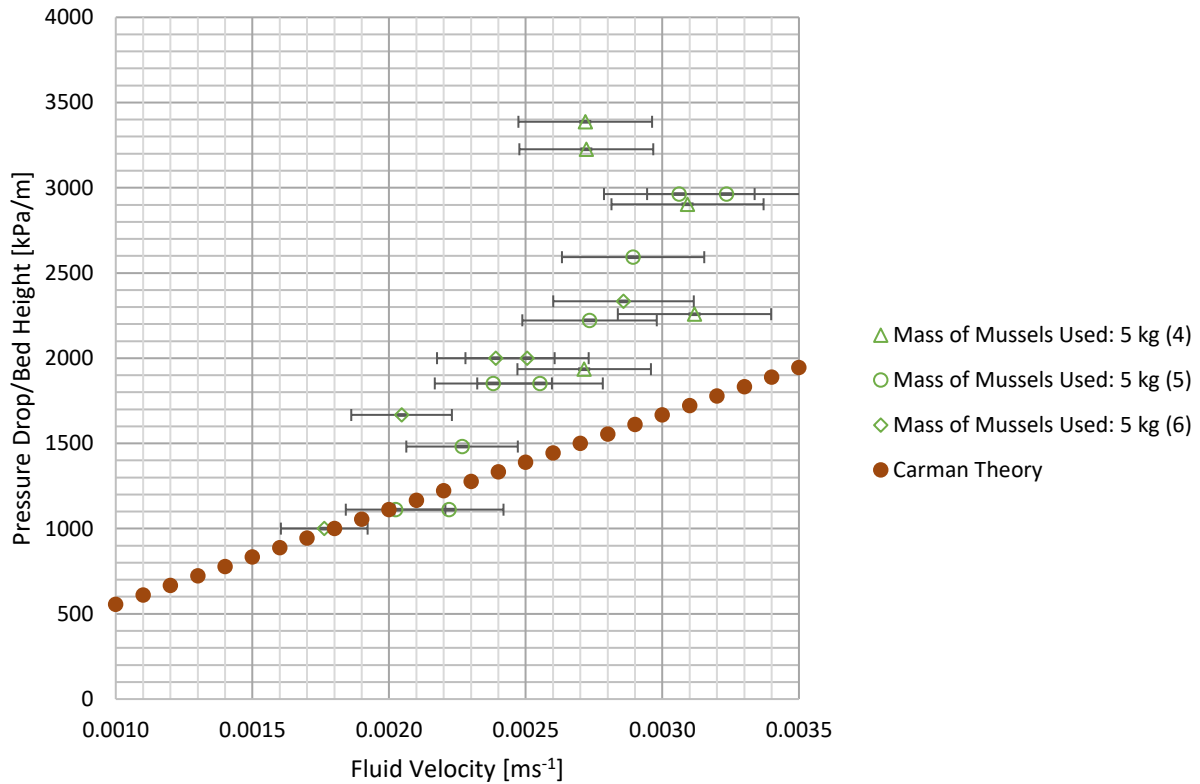


Figure 15 Incompressible Carman Correlation

Taking the averages of the three, more reliable, data sets (Figure 14) gave the empirical estimation for the pressure drop over a bed of grade D mussels up to the stagnation point or MAP. It should be noted that, at the higher pressures ( $P > 90 \text{ kPa}$ ) an average was unachievable due to the lack of data points in this area. Rather than displaying an average at pressures above 90 kPa the sole data points were used. Experiments 4 through 6 were run at an average bed height of  $29 \pm 2 \text{ mm}$ . The averaged data best fit a power trend with an  $R^2$  value of 0.9623, with the pressure drop being equal to  $2 \times 10^8 x^{2.5189}$  (Figure 16).

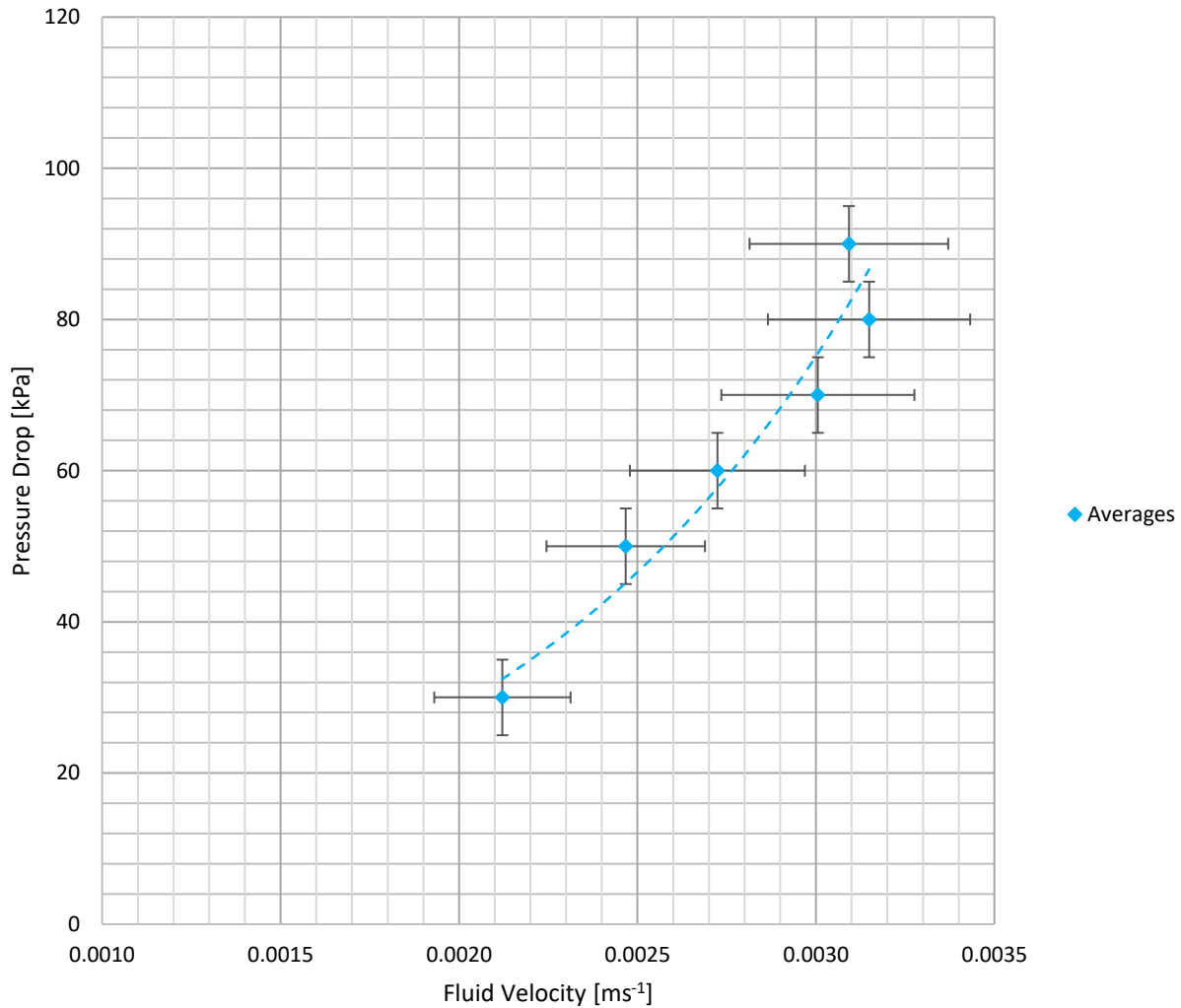


Figure 16 Average Trend of the Reliable Data Sets

### 5.1.2.3 Lumped Drag Coefficient as a Function of Bed Velocity

The lumped drag coefficient term ( $C'_D$ ) that is used in the wet bed mathematical model was found by correlating the fluid velocity to the lumped drag term (Eq. 23). The results can be seen on Table 3 Empirical Correlations below. The correlation was found using some third-party curve plotting software.

Table 3 Empirical Correlations

Viscosity Coefficient ( $C'_D$ )	$C'_D = 9.842 \times 10^5 \vec{v}_{ave}^{-1.06}$
----------------------------------	--

Using this empirical correlation along with the volumetric flow rate translation for the linear velocity, a solution to Eq. 16. Due to solving issues, the power was approximated to -1 as there was no obvious solution at -1.06. When approximating the power to -1 the new coefficient term was derived to be  $2.437 \times 10^6$  (A), giving the solvable equation (Eq. 52):

$$C'_D = A \vec{v}_{ave}^{-1} \quad (52)$$

#### 5.1.2.4 Steady-State Volumetric Flowrate

This solution is arguably close to the original solution, given that the error on the original solution was  $1.529 \times 10^6$  and 0.254 for the coefficient and the exponential, respectively. These error terms are high due to the lack of data that was present from the static bed experiments before catastrophic failure occurred in the vessel. By substituting Equation 52 in to Equation 14 and deriving an equation for the volumetric flow rate through the bed gives Eq. 53.

$$V = \pi r^2 z \left[ A \pm \sqrt{(A)^2 - 4\omega^2} \right] \quad (53)$$

By differentiating Eq. 53 with respect to radius (Eq. 54) and setting the differential to zero will allow for the steady state volumetric solution to be found.

$$\frac{dV}{dr} = 2\pi r z \left[ A \pm \sqrt{(A)^2 - 4\omega^2} \right] = 0 \quad (54)$$

Given that the volumetric flow rate has to be constant across the entire bed, the differentiated volumetric equation for the fluid balance has two separate solutions, one at the positive root and one at the negative root. Since the volumetric flow is constant across the entire bed, irrespective of the radius, the only way the differential can reach zero is if the square root term is equal to  $(2.437 \times 10^6)^2$ . This allows the two lumped drag coefficient terms to cancel out. These two terms cancel out when the angular velocity ( $\omega$ ) reaches zero. This leaves the final equation for the steady state volumetric equation to be at the negative root (Eq. 55).

$$V = \pi r^2 z \left[ A - \sqrt{(A)^2 - 4\omega^2} \right] \quad (55)$$

This final volumetric flow rate equation (Eq. 55) can then be substituted in for the volumetric flow rate in the linear fluid velocity equation (Eq. 12). This removes the volumetric term from the equation, giving the linear fluid velocity as a function of only the radius and angular velocity (Eq. 56).

$$\vec{v}_{ave} = \frac{1}{2} r \left[ A - \sqrt{(A)^2 - 4\omega^2} \right] \quad (56)$$

Using this new linear velocity equation (Eq. 56) in conjunction with the mussel orientated momentum balance (Eq. 11) gives a relation for the pressure change with respect to radius (Eq. 57)

#### 5.1.2.5 Maximum Force Calculation (Wet Bed)

$$\frac{dP}{dr} = \rho_a r \omega^2 + \frac{1}{2} A \rho_w r \left[ A - \sqrt{(A)^2 - 4\omega^2} \right] \quad (57)$$

Integrating this differential between the inner radius ( $r$ ) and the outer radius ( $R$ ) of the bed gives the pressure change over the bed (Eq. 58).

$$P = \frac{1}{2} \omega^2 \rho_a (R^2 - r^2) + \frac{1}{4} A \rho_w (R^2 - r^2) \left( A - \sqrt{A^2 - 4\omega^2} \right) \quad (58)$$

This pressure relation can then be translated to a force equation using the pressure equals force over area ( $2\pi r z$ ) relation. This gives the final equation that can be modelled in terms of the angular velocity and the radius (Eq. 59).

$$F = \pi R z \omega^2 \rho_a (R^2 - r^2) + \frac{1}{2} A \pi r z \rho_w (R^2 - r^2) \left( A - \sqrt{A^2 - 4\omega^2} \right) \quad (59)$$

Using this force equation over a number of omega values shows how the force changes within the wet bed as the radius and angular velocity increases (Figure 18). Before the forces within the centrifuge can be optimized the capacity must be investigated.

### 5.1.3 Centrifuge Design Optimization

#### 5.1.3.1 *Mass Optimization*

When designing the centrifuge there were a number of factors that needed to be considered such as the, inner radius, outer radius, height of the centrifuge, angular velocity of the centrifuge relative to the outer radius, time to spin up and stop the centrifuge and how long the centrifuge would be held at operating angular velocity.

The primary dimensions of the centrifuge needed to be defined first as they are key parameters for calculating the throughput of the centrifuge. The throughput of these centrifuges, ideally, needs to match the throughput of the factory. In conjunction with the mass flow required the radius of the centrifuge affects the pressure experienced by the bed of mussels and in turn affects the fluid flow through the bed. With this in mind the outer radius was chosen to be similar to that of the current shell separation centrifuges (0.25 m) as this would make it easier for implementation of the test rig. The inner radius was chosen to minimize the height of the centrifuge and maximize the capacity of the centrifuge (0.01 m).

The mass per unit per cycle required was found to be 15.63 kg. With this mass and cycle times a set of separators would be able to keep up with the factory throughput. Considering that the inner and outer radius has already been determined, the height of the centrifuge was the last parameter that could be manipulated for capacity optimization. A model (Figure 17) was used to predict the relationship between the mass of the centrifuge, the height of the centrifuge and the mass of mussels within the centrifuge. There is also a dashed line that indicates where the optimum mass intersects each bed height curve.

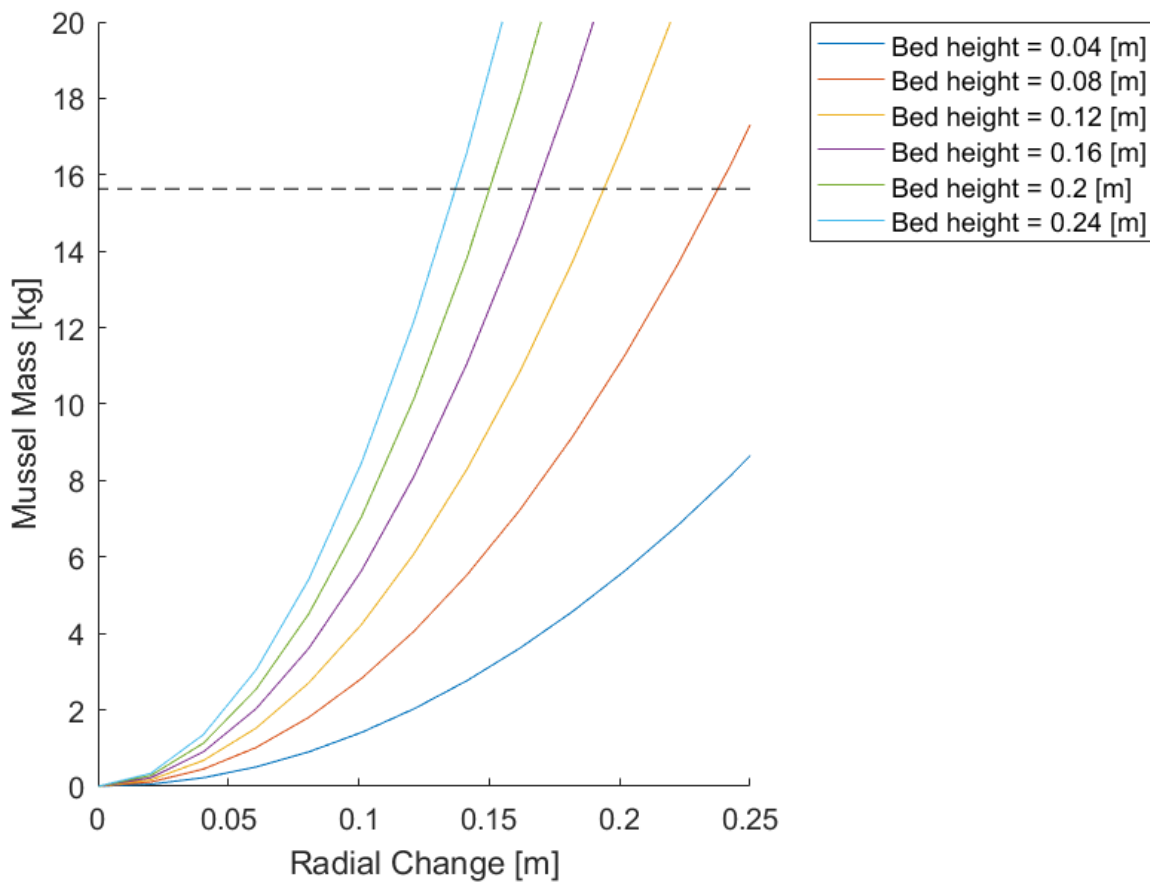


Figure 17 Mussel Mass as a Function of Bed Height

The solution of the line that intersects the optimum weight (15.63 kg) and radial change (0.06 m) is at a bed height 0.58 m. This provides a height to diameter ratio (H/D) of 0.1. Where centrifugal spray dryers use a H/D ratio of 1:1 when in a turbulent regime and up to 5:1 for laminar systems (McKetta & Cunningham, 1992). With these known parameters a purpose-built centrifuge can be constructed for the separation of the surface water from whole mussels. This centrifuge will operate at a pressure where the percolation is still possible while maximizing the applied force on the mussels and, in theory, maximizing the surface water removed. Where this pressure is determined by the angular velocity of the centrifuge. To find the angular velocity at which maximum percolation can be achieved the lumped drag coefficient term must be empirically derived.

#### 5.1.3.2 Angular Velocity Optimization (Wet Bed)

The final force equation that related the force to the radial distance (Eq. 59) was used to produce the wet bed solution over a range of angular velocities (Figure 18).

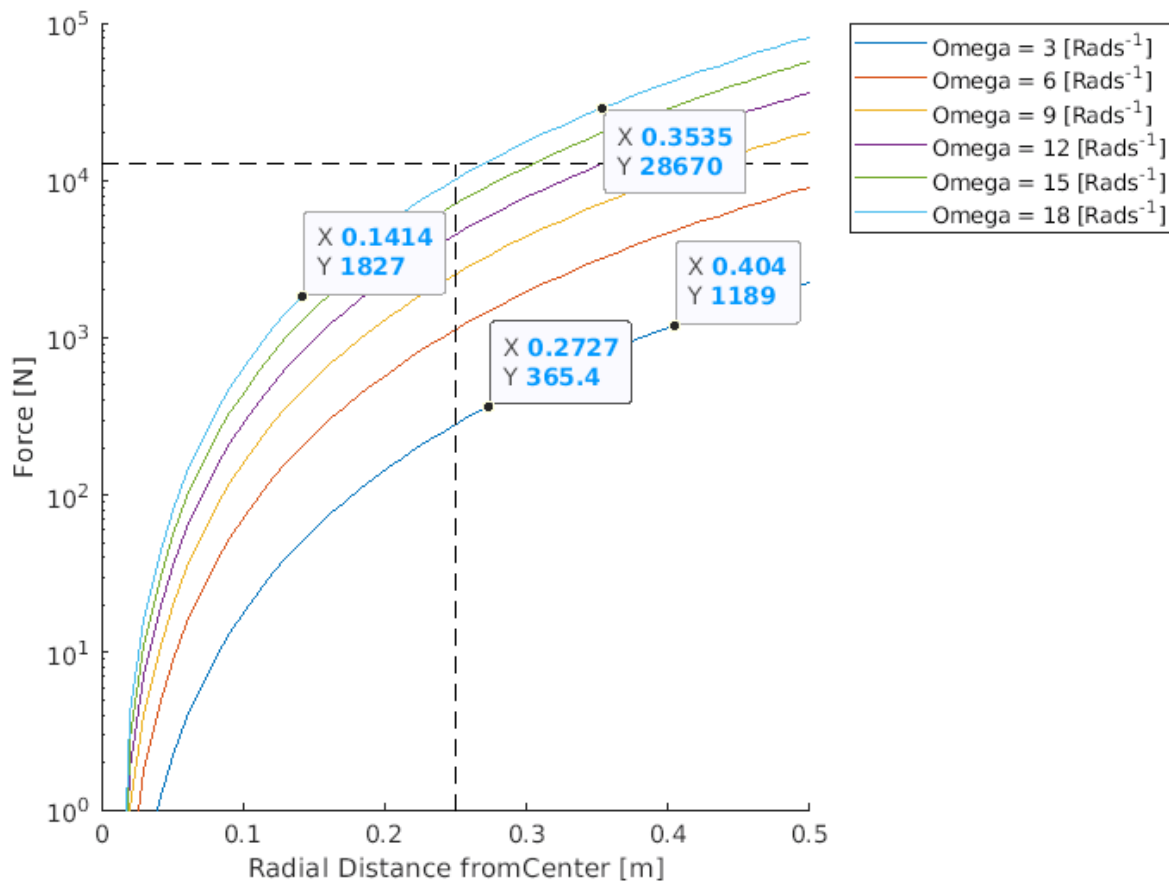


Figure 18 Wet Bed Solution

Using the wet bed model, the force within the mussel bed easily exceeds the maximum force of 12.7 kN at a relatively small angular velocity, 20 rad s<sup>-1</sup>, when using a maximum outer radius of 0.25 m. The wet bed plot (Figure 18) reads exactly the same as the dry bed solution (Figure 20) even though the force is comprised of two parts, in the case of the wet bed, compared to the single force dependency used to calculate the dry bed scenario.

One of the factors that largely influences this model is the use of the apparent density and in particular density of the water. The apparent density term considers the buoyant force that is acting on the mussels when submerged in a less dense solution, i.e. water. To justify that the wet bed solution is an extension of the dry bed solution, the limit as  $\rho_w \rightarrow 0$  was taken and compared to the force plot using the dry bed model (Figure 20). From a mathematical standpoint, it can be seen that as the density of the water tends to zero the drag term will be reduced to zero and the  $\rho_w$  term in the apparent density will also be removed (Eq. 59). This leaves only the centrifugal term as seen in the dry bed model. As the water density approaches 0 the wet bed force plot (Figure 19) is exactly the same as the dry bed plot (Figure 20).

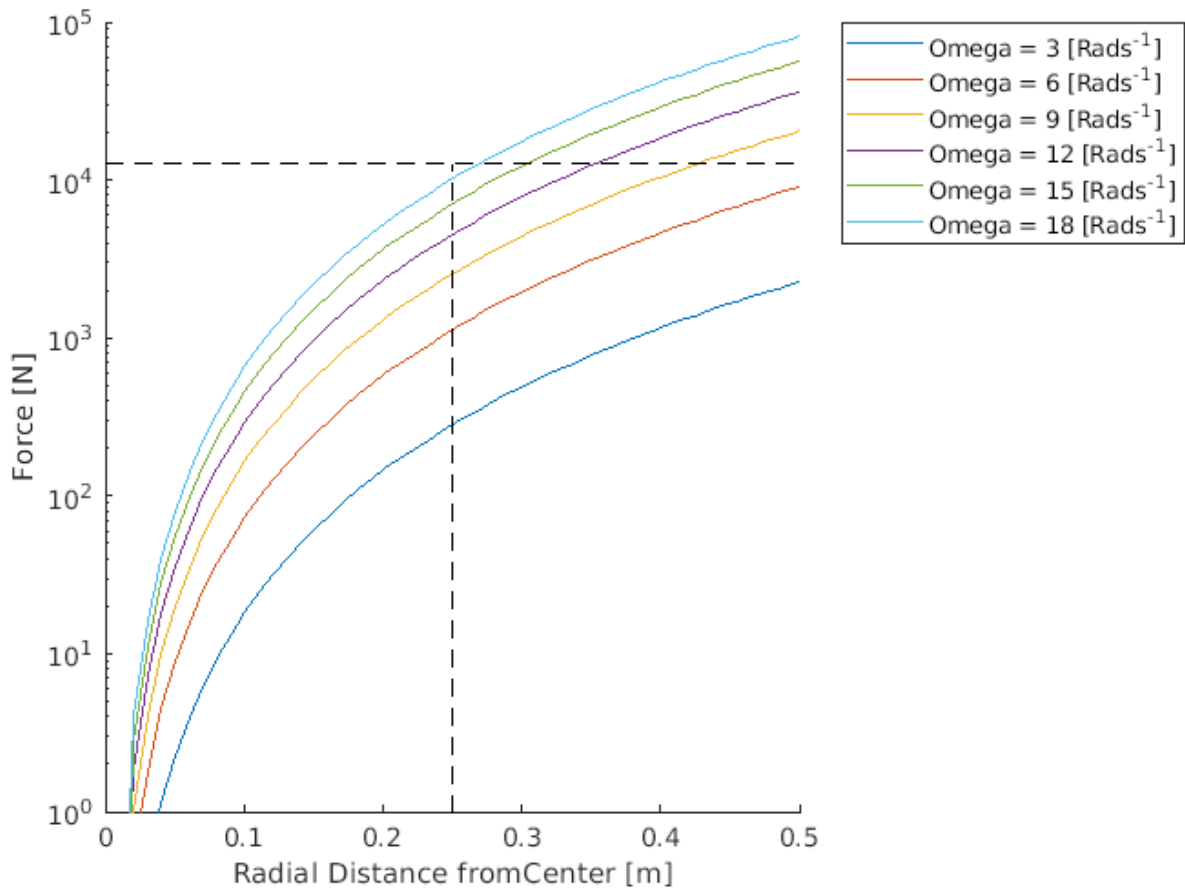


Figure 19 Wet Bed Scenario as  $\rho_w \rightarrow 0$

The main benefit of comparing both the wet bed and the dry bed scenarios is that the limiting scenario can be found and used for more accurate centrifuge design.

#### 5.1.4 Angular Velocity Determination (Dry Bed)

By solving the dry bed mathematical model (Eq. 19) while varying both the radius from the center and the angular velocity gives Figure 20. It can be seen from this figure that the optimum angular velocity at a distance of 0.25 m from the center is 20 rad s<sup>-1</sup>. The force increases exponentially as the bed of mussels gets thicker in the dry case.

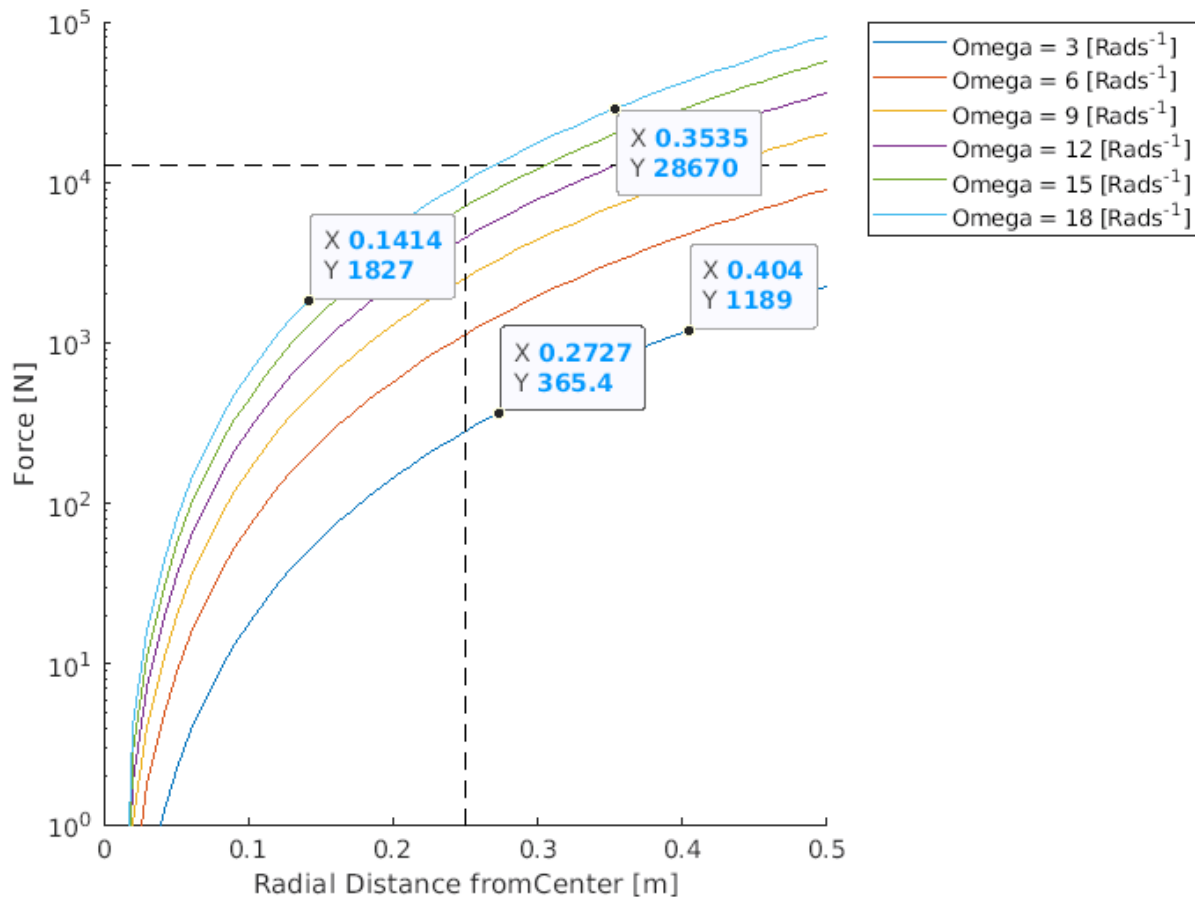


Figure 20 Dry Bed Solution

The smallest possible angular velocity was chosen for the design of the centrifuge because it was assumed a smaller angular velocity would take less time to achieve spin up and spin down, which would allow for a greater hold time and water removal. As well as being more efficient on a time scale it was also thought that having a less aggressive spin up and down cycle would have less wear on the parts.

The static bed experimentation and the mathematical modeling for the centrifuge allowed an insight into the force that the mussels receive across the radius of the proposed centrifuge. It looked as though the state of the bed, whether it be filled with water or not, the force experienced by the mussels along the depth of the bed is the same. This would imply that the limiting case is the wet bed scenario.

## 5.2 Post-Homogenization SAP Results

The post-homogenization solution involved the use of an SAP to wick away the water from the macerate. To properly understand the effects of the SAP on the macerate, the thermal and mass implications of the addition of an SAP layer was the first factor that needed to be investigated.

In order to be able to solve the steady-state thermal equilibrium equation, the thermal conductivity of the macerate had to be empirically determined by fitting the non-steady-state model of the system

(Section 3.2 ) to empirical time-temperature data collected during the freezing process. This process was conducted for the control (absence of the SAP layer) to fit an average thermal conductivity and then repeated with the SAP on the top and bottom positions. The thermal center of the slab also needs to be verified to ensure an accurate fit of the model since heat conduction occurs in two directions with separate boundary conditions.

There are two stages to the freezing process. In the first stage the macerate goes from a uniform room temperature (nominally 25°C) to the onset of freezing at the outer edges. Once the first layer of ice forms, the second stage is characterized by the growth of the ice layer from the top and the bottom of the macerate towards the middle. Therefore, both the thermal conductivity of the liquid and frozen macerate needs to be empirically determined.

The second factor that had to be evaluated was the mass of water removed and analysis of possible impact on oil yield. The mass change of the SAP over the freezer tunnel was recorded and attributed to the water removed. The SAP treated macerate was also compared to a control sample to check for variation in the oil yield.

#### 5.2.1 Thermal Profile of the Macerate

The thermal profile of the top and bottom of the macerate over time spent in the tunnel freezer were measured and the average profile from the various experiments is shown on Figure 21. Figure 21 contains three regions, the first is the initial cooling of the liquid macerate (from 0 to 750 s). This is followed by the freezing of the macerate (from 751 to 900 s). The transition between these two critical regions is brief and appears to consist of slight subcooling of the macerate below the freezing temperature followed by a quick recovery once freezing commences. Once the macerate freezes to the thermal center, the entire slab begins to cool more quickly to the temperature maintained in the tunnel freezer (−20°C). This is the third process region ( $\geq 1500$  s).

On average the two surface temperature profiles were remarkably similar, with the two only differing by a maximum of 1 °C at any time point. This 1 °C discrepancy could very well be caused by inaccuracies in the testing method, such as the error associated with the human component of the testing method. Some of these errors could have been from slightly different placement areas of the top and bottom temperature probes and the variations in thickness at these different points. This will be more critically analyzed in the Discussion section.

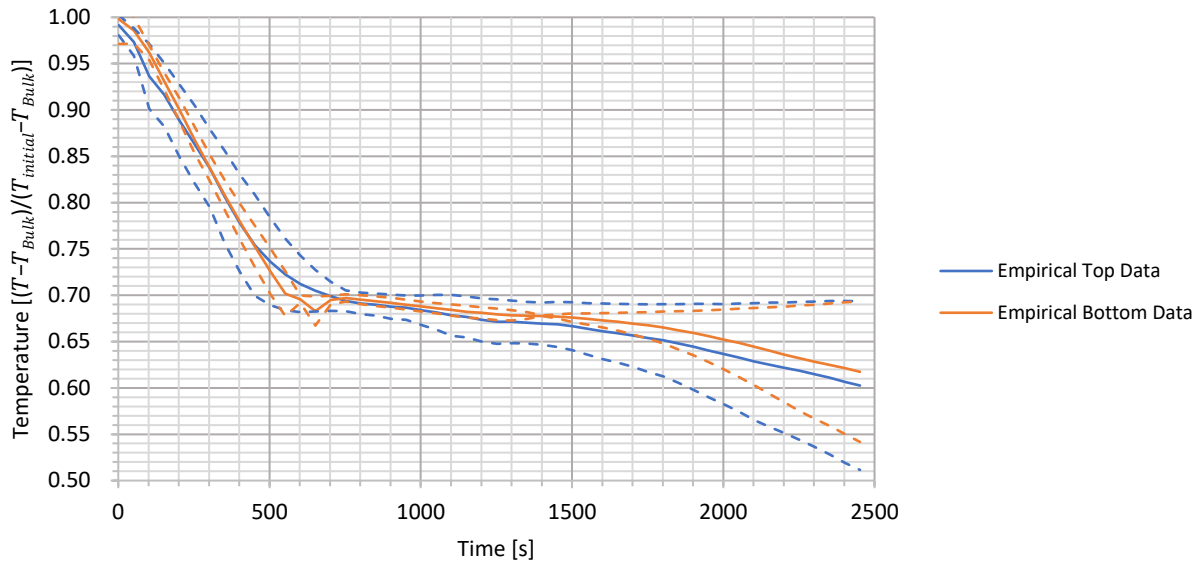


Figure 21 Average Macerate Temperature Profile from the Three Experiments Run Without an SAP Layer

There are some variations observed in the transition region between 500 and 900 s on the bottom temperature profile, which are shown in more detail below (Figure 22). The discrepancies seen in Figure 21 are characterized by a series of sudden increases (1.7 °C) in the measured temperature back closer to the top surface after excursions below the temperature observed. On average these temperature fluctuations on the bottom surface averaged 1.62 °C between 500 and 900 s after entry into the tunnel freezer. This temperature increase started, consistently between -3.7 and -4.3 °C and lasted between 30 and 50 s. It is believed that this variation is caused by the onset of macerate freezing where the heat of fusion released by molecules just starting to freeze near the probe, or it is an indication of subcooling with subsequent heat of fusion returning the temperature to the melting point. This subcooling and sequent temperature rise only appears on the bottom surface of the macerate layer, not the top surface. The amount of subcooling and timing of this subcooling varied from run-to-run, suggesting that the metal tray was inhibiting freeze nucleation in some way. Since this region denotes the transition to a clearly different heat transfer regime and is so close to the melting point of water, it is believed that this provides a measurement of the true melting point of the macerate, -4.15°C. It also means that there was a transition from heat capacity-limited cooling to heat of fusion-limited cooling models. The error associated with the average empirical data sets (Figure 21) was found by calculating the standard deviation over the replicated data sets taken. It is interesting to note that most of the deviation occurred at the end of the freezing cycle.

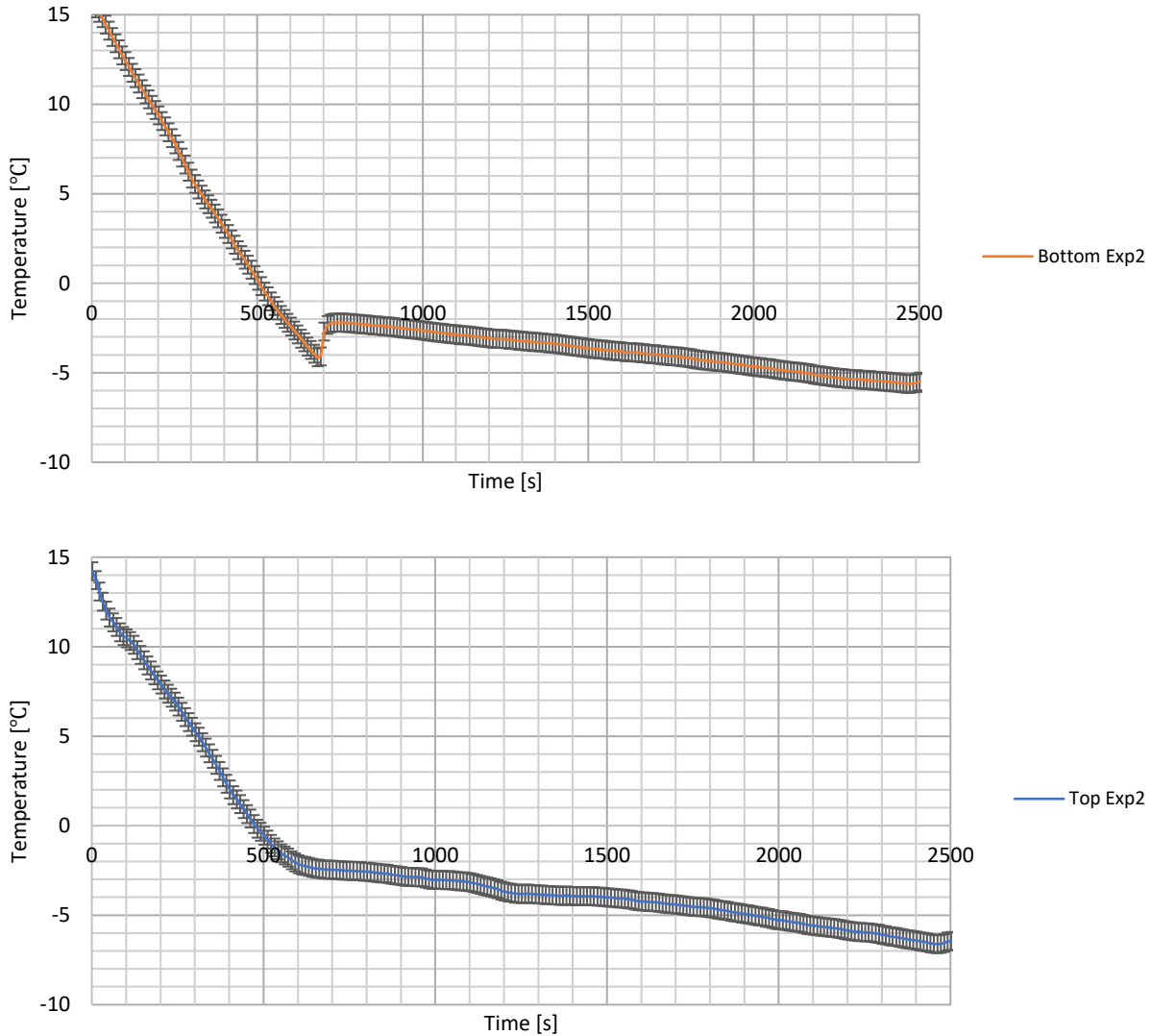


Figure 22 Thermal Profile at the Top and Bottom of the Macerate During the Second Experiment

### 5.2.2 Determination of the Macerate Thermal Conductivity Without SAP

Using the heat resistance model (Eq. 34) an initial guess for the thermal center can be determined assuming that the thermal conductivity of the macerate is a constant. This estimate is based on estimates for the conductive terms at the macerate boundaries. However, the macerate thermal conductivity needs to be determined by solving the full transient model of the system (Eq. 48). The numerical integration of the full transient model had to be solved first in order to find an estimate for the thermal conductivity of the macerate by fitting the model to the empirical data, since the thermal properties of the macerate are undefined. As previously stated, the thermal properties of the macerate were estimated using the thermal properties of water as an initial guess.

The numerical integration of the current situation was broken up into three portions, initial cooling of the liquid macerate, freezing of the macerate, and propagation of the frozen front through the macerate. The

code that was used to produce the simulation below (Figure 23) can be seen in Section 8.4.2 . Where the thermal properties of water were multiplied by a correction factor to make the mathematical integration match the empirical data. The model simulation (Figure 23), using modified thermal conductivities for the liquid and frozen macerate (2.312 and 0.218 W m<sup>-1</sup> k<sup>-1</sup> respectively), fits well within the error bars for most of the simulation (Figure 23) except in the critical transition region (500 to 700 s). The temperature of these plots was scaled using the initial temperature and the bulk freezer temperature (− 40°C) so that a fair comparison can be achieved between the data sets obtained in summer and winter. This will be further discussed in Section 5.2.3 .

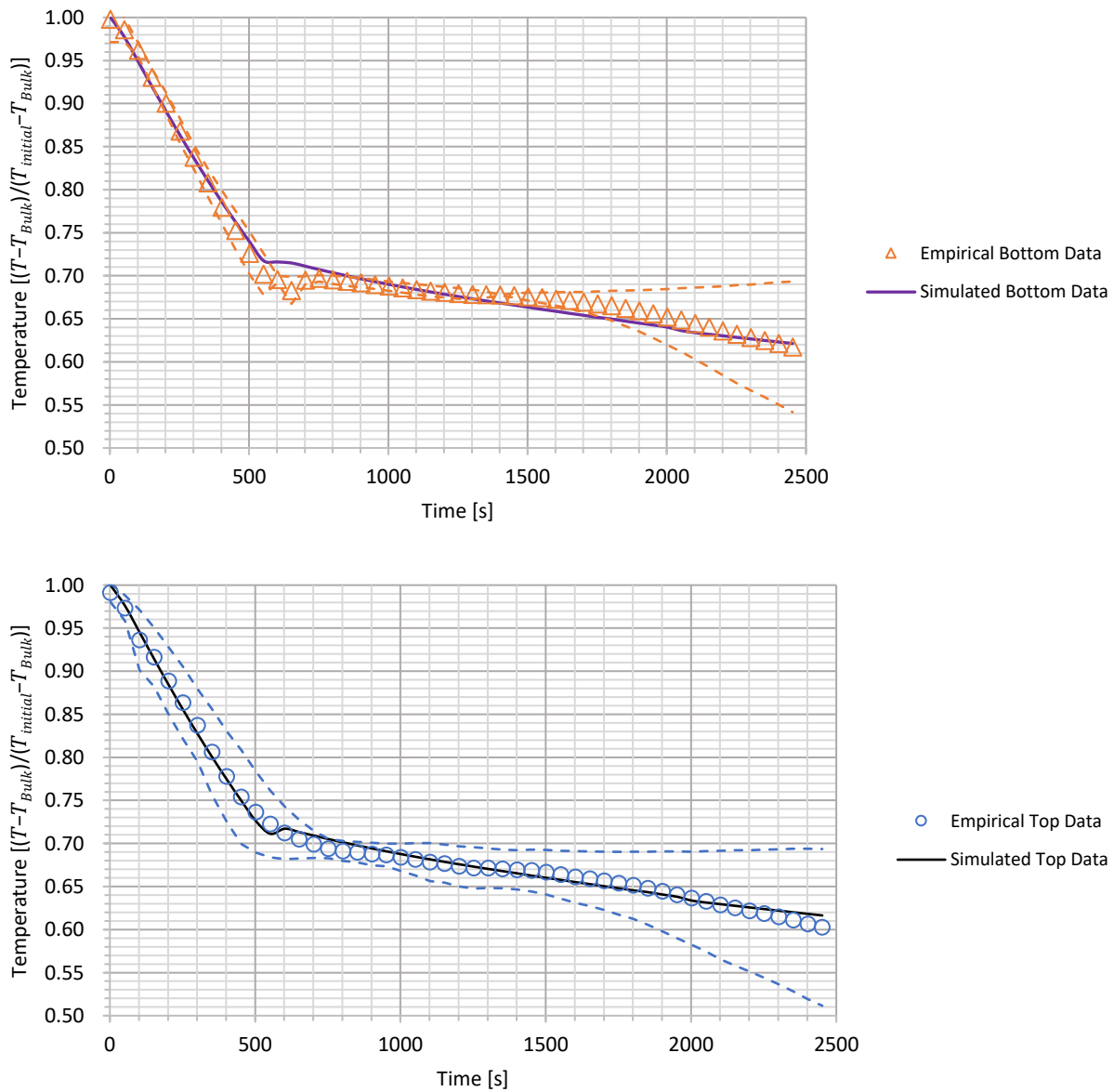


Figure 23 Modelled Data Compared Against Experimental Data

Using the aforementioned modified  $k$  value of  $2.312 \text{ W m}^{-1} \text{ K}^{-1}$  for the thermal conductivity of the liquid macerate made the mathematical simulation fit the empirical data relatively well. The gradients of the empirical and mathematical data can be seen in the following table and the empirical data matched the simulated data with a maximum deviation of  $0.04 \text{ }^\circ\text{C}$  seen between the top data sets. The simulated data then deviates from the empirical data, with the maximum deviation between the bottom data sets ( $1.5 \text{ }^\circ\text{C}$ ), during the freezing of the macerate. After the transition from macerate freezing to cooling of the frozen mass, the simulation for the top data fit the empirical top data with the same level of deviation as the bottom set ( $1 \text{ }^\circ\text{C}$ ). The gradients of the simulated data and empirical data as they move away from the transitional areas is displayed below on Table 4. This table helps to show the accuracy of the simulated data as it moves towards and away from the transitional area. Where the simulated gradients for the top and bottom fit the empirical data, a maximum deviation of  $\pm 0.38$  over the initial cooling phase (0 to 500 s) and  $\pm 0.69$  over the freezing phase (1000 to 2500 s).

Table 4 Gradient Analysis

**Gradients (0-500 s)**

Data Name	Gradient	Uncertainty
Top (Emp.)	-5.10E-04	1.09E-02
Top (Sim.)	-5.48E-04	-
Bottom (Emp.)	-5.44E-04	8.01E-03
Bottom (Sim.)	-5.21E-04	-

**Gradients (1000-2500 s)**

Data Name	Gradient	Uncertainty
Top (Emp.)	-5.60E-05	4.37E-02
Top (Sim.)	-4.91E-05	-
Bottom (Emp.)	-4.87E-05	2.44E-02
Bottom (Sim.)	-4.74E-05	-

No corrections in these models are made for the heat capacities, densities, or latent heat of fusion components. These were assumed to be the same as that of water. The simulated freezing of the macerate was governed largely by the freezing point of the macerate.

The empirical data shows that the freezing point of the macerate resides somewhere between  $-3.7$  and  $-4.3^\circ\text{C}$ . A variety of values were experimented with, as an adjustable parameter within the model, across this freezing point range. The value of  $-4.15^\circ\text{C}$  gave the best fit to the empirical data, suggesting that the components of the macerate (protein, oil and small molecules present in the cells of the mussel meat) caused significant freezing point depression.

The simulation for the propagation of the frozen front did not fit the empirical data as well at the cooling portion. With the simulated data deviating as much as  $1.3 \text{ }^\circ\text{C}$  from the empirical data. This could have been due to the model not accounting for the cooling of the ice.

The thin spikes in the temperature seen around 1500 s can be attributed to the freezing of deeper layers within the macerate (Figure 33). If the simulated freezing of these deeper layers were less abrupt, then the simulated data may have followed the empirical data, more precisely.

The simulated propagation of the frozen front through the depths of the macerate can be seen in Figure 24 . This figure is indicative of the time at which the macerate freezes at any given depth relative to the mathematical equations used to simulate the heat transfer through the top and the bottom of the macerate. The simulation for the heat transfer through the top and bottom of the macerate shows that the thermal center of the macerate is approximately 5 mm above the bottom of the tray and occurs at approximately 1800 s. This result for the thermal center of the macerate correlates to the solved solution from Eq. 34, in which the thermal center of the macerate was found to be 5 mm above the bottom of the macerate as well.

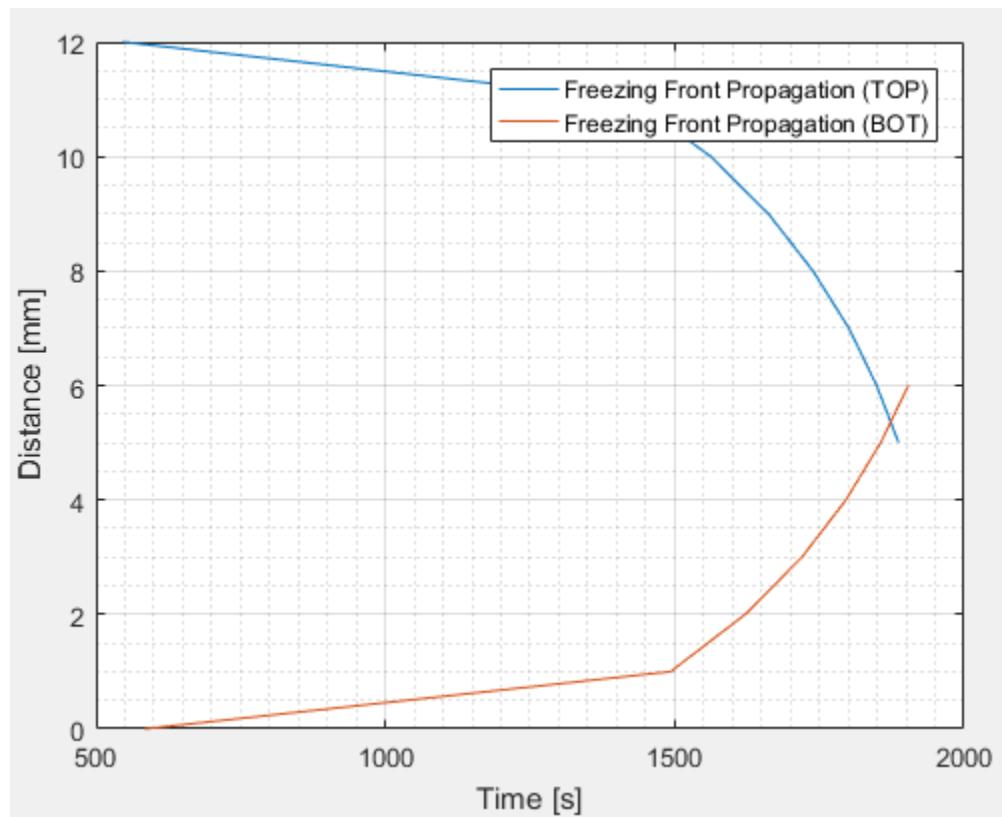


Figure 24 Propagation of the Frozen Front Through the Macerate

The data retrieved, from both the balanced heat transfer equation and the simulated heat transfer through the macerate, shows that the heat transfer through the top of the macerate is dominant when compared to the heat transfer through the bottom of the macerate. Therefore, from a heat transfer perspective, it would be best to place the absorbent pad on the bottom of the macerate in order to reduce any insulative effects on the freezing process.

The results for the thermal profile and the mathematical models with the addition of the absorbent pad will be discussed in the following section.

### 5.2.3 Thermal Profile with an Absorbent Pad

The addition of the absorbent pad on the bottom of the macerate had significant implications to the thermal profile seen within the macerate. As seen in Figure 25 below, the addition of the absorbent pad

had significant detrimental effects to the heat transfer profile through the bottom of the macerate. The average temperature of the macerate after 2500 s was 4 °C warmer with the addition of the absorbent pad as well as having the, presumed, freezing inflection point delayed by 350 s. The freezing point seen with the addition of the absorbent pad occurs 14% later than without the absorbent pad. The exit temperature increase was seen despite the entry temperature of the macerate being 5 °C lower than the initial, non-absorbent pad experiments.

The entry temperature of the absorbent pad experiments was higher due to a change in external factors when the tests were conducted. The cooling units prior to the tunnel freezer tend to work more effectively during the winter season as well as the product generally being cooler throughout the winter season, resulting in the drop in the entry temperature of the macerate seen in Figure 25 below. The temperature of the macerate was scaled against the inlet temperature and the bulk temperature. This data was manipulated in this way so that the thermal profiles could be compared fairly. The SAP data, Figure 25, was taken in winter where the tunnel freezer can operate more efficiently due to external factors. Whereas, the empirical top and bottom data (Figure 25) were taken during the summer months, therefore making the inlet temperature greater than that of the SAP data. Even with the added benefit of having a cooler inlet temperature the SAP data still performed significantly worse in all areas, when compared to the non-SAP data. A scaling method was used to compare the data because of the change in standard operating temperature of each data set. The three data sets were taken during different seasons, which noticeably impacts the standard operating temperature of the macerate.

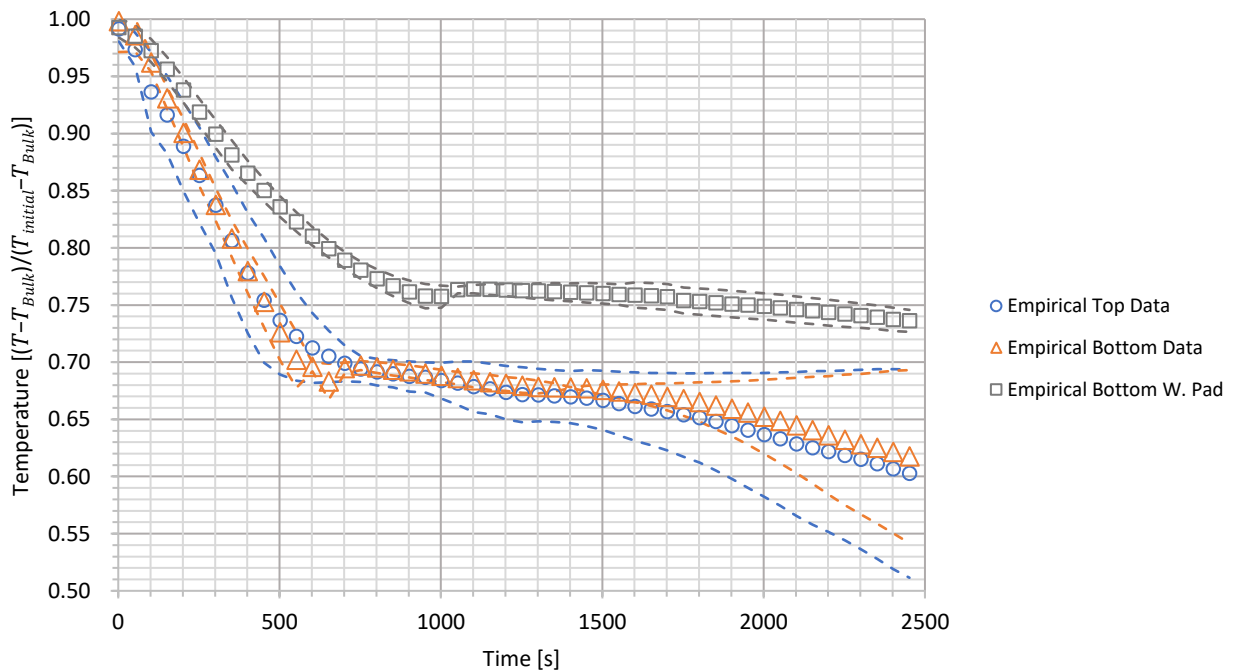


Figure 25 Empirical Data Including Absorbent Pad

Table 5 Gradient Analysis with SAP

**Gradients 0-500 s**

Data Name	Gradient	Uncertainty
-----------	----------	-------------

<i>Top (Emp.)</i>	-5.10E-04	1.09E-02
<i>Top (Sim.)</i>	-5.48E-04	-
<i>Bottom (Emp.)</i>	-5.44E-04	8.01E-03
<i>Bottom (Sim.)</i>	-5.21E-04	-
<i>Bottom (SAP Emp.)</i>	-3.13E-04	1.09E-02
<i>Bottom (SAP Sim.)</i>	-3.00E-04	-

**Gradients 1000-2500 s**

<i>Data Name</i>	Gradient	Uncertainty
<i>Top (Emp.)</i>	-5.60E-05	4.37E-02
<i>Top (Sim.)</i>	-4.91E-05	-
<i>Bottom (Emp.)</i>	-4.87E-05	2.44E-02
<i>Bottom (Sim.)</i>	-4.74E-05	-
<i>Bottom (SAP Emp.)</i>	-1.46E-05	9.35E-03
<i>Bottom (SAP Sim.)</i>	-2.40E-05	-

Of the experiments taken there was one set of data, Exp 2, that significantly differed from the other data sets (Figure 26). The Exp 2 data set showed an initial cooling gradient of -0.0311 which was similar to that seen in the section above (Table 4) and showed a significantly quicker cooling rate post-freezing. This particular experiment, Exp 2, was conducted on a day where there was no other product running through the tunnel freezer and this lack of thermal loading meant that the tunnel was operating at -45 °C rather than the regular -25 °C. Exp 2 was discounted when calculating the averages seen above in Figure 25 due to the irregularities in the operating conditions.

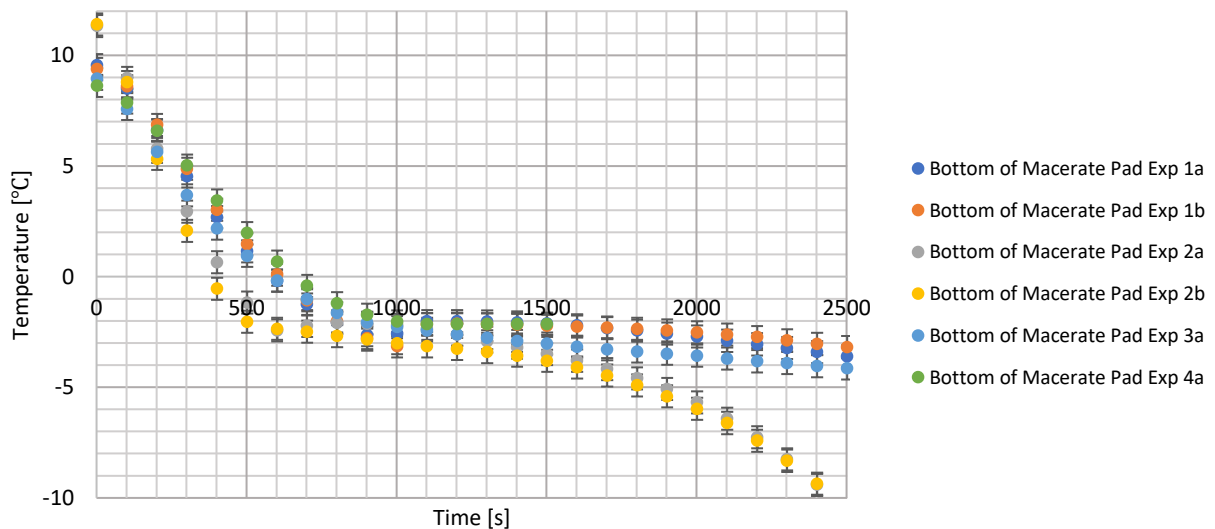


Figure 26 Empirical Data Sets with Absorbent Pad

For the post-homogenization section of the report there were two factors that needed to be considered, the impact of the absorbent pad on the freezing of the macerate and the amount and composition of the fluid uptake of the absorbent pad. Where the addition of the absorbent pad can be seen to significantly affect the tunnel freezer operation, it does not take the procedural difficulties associated with the

absorbent pad removal from the macerate post-freezer into account. The mass change and composition of the absorbent pad will be discussed in the following section.

#### 5.2.4 Modelled Thermal Profile with an Absorbent Pad

The modified mathematical model of the thermal profile through the bottom of the macerate with the addition of the absorbent pad can be seen on the figure below (Figure 27). The mathematical model fits the empirical data surprisingly well with the greatest deviation, of 1 °C, occurring around the aforementioned freezing point of the macerate.

The liquid and frozen thermal conductivities were modified to 2.312 and 0.218 W m<sup>-1</sup> k<sup>-1</sup> respectively, which is half of that used for the liquid conductivity in the previous section (Section 5.2.2 ). This trend of decreasing thermal conductivities for both the liquid macerate correlates with reports by Sharqawy (Sharqawy, 2012) and Caldwell (Caldwell, 1973). Where both of the aforementioned reports divulge a slightly decreasing trend in thermal conductivity with an increasing salinity.

Another factor that would have attributed to the change in thermal conductivity of the macerate would have been the increase in biological content. When trying to research the possible effects of the biological content on the thermal properties of a solution there is little that relates to the thermal properties of shellfish, let alone how variations in concentrations affect the thermal properties.

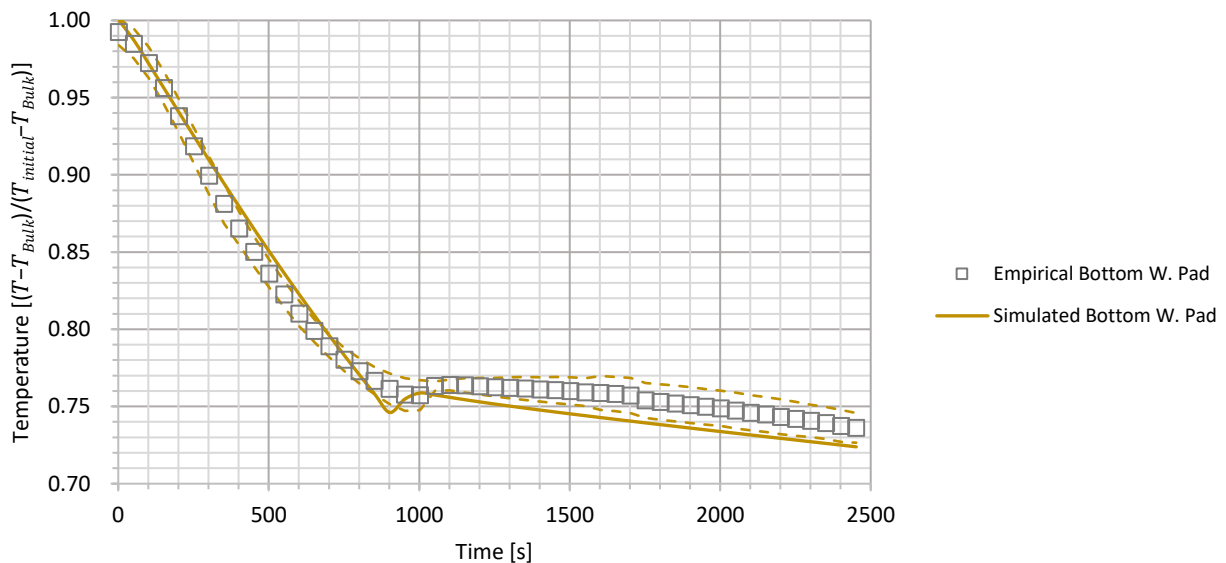


Figure 27 Empirical and Mathematical Temperature Profiles

It can be seen on this graph (Figure 28) and the figure above (Figure 27) that the freezing of the modeled curve stated occurring at around 1000 s, which equates to 40% of the total time spent in the freezer. The freezing of the bottom of the macerate starts occurring approximately 400 s later with the addition of the absorbent pad, 24% of the total time spent in the freezer. The addition of the absorbent pad to the bottom of the macerate increases the time taken to start freezing the macerate by two thirds, which equates to 16% of the total time spend in the tunnel freezer.

The new thermal center of the macerate was located at the bottom of the macerate as depicted in the modeled data below (Figure 28). This plot shows that only the first 2 mm of the macerate at the bottom of the tray begins to freeze before the macerate is removed from the tunnel freezer. It also shows that the new thermal center of the macerate would be located at approximately 0.75 mm above the bottom of the tray. This follows the solver trend that indicates that the thermal center of the macerate can be found at the bottom of the tray when the absorbent pad is applied.

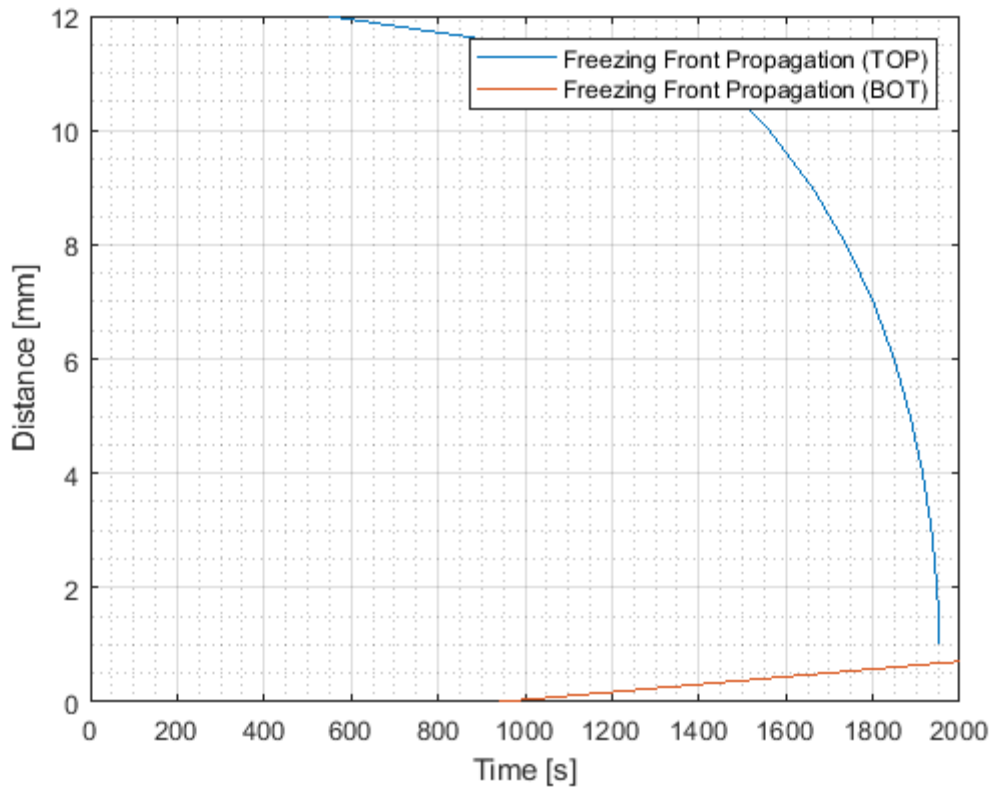


Figure 28 Propagation of the Freezing Front Through the Macerate with Absorbent Pad

#### 5.2.4.1 Mass Change of the Absorbent Pad

The mass change in the absorbent pad over the tunnel freezer was measured, on average, to be  $584 \pm 0.5$  g. This  $584 \pm 0.5$  g is equivalent to 9.7% of the total macerate mass being removed. Where half of each tray was covered with the absorbent pad, in an industrial setting the size of the absorbent pad would be doubled, offering close to 20% water removal. The portion of the tray that had the absorbent pad was noticeably softer to the touch than that of the non-padded area of the tray. This could be indicative of the insulative effects of the pad, as previously discussed, or due to a higher organic content. Although this delay in freezing would result in a longer period of time for absorption to occur.

Another influential factor that could have affected the amount of fluid absorbed was the time of removal. As previously mentioned, the removal of the absorbent pad from the partially frozen macerate was an involved procedure. It would take 10-15 minutes to remove the absorbent pad from the macerate, depending on how frozen the macerate edges were. During the removal process the center of the padded

area was in a semi-solid form, where it was not frozen solid but was not a liquid either. The removal of the absorbent pad from these semi-solid areas was the easiest as the pad would peel away from the macerate fully intact. Whereas the macerate would bind to the absorbent pad, on the frozen fringes, making removal more time consuming and difficult.

The composition of the absorbent pad was measured indirectly through fatty analysis of the macerate, rather than analysis of the pad itself.

The compositional analysis of the macerate slab found that there was, on average, a 0.3 and 0.2 g per 100 g variation in the total fat and free fatty acid (FFA) content, respectively. Where the difference seen between the test and the control was 0.1 g per 100 g decrease in the control free fatty acid content compared to that of the macerate with the absorbent pad. It should be noted that the control is defined as the area of the tray that did not contain any absorbent pad during the experimentation with the tunnel freezer.

The macerate can vary by  $\pm 1$  g per 100 g over the tray. This uncertainty associated with the consistency of the macerates composition could be a result of a lack of thorough mixing within the system. With the acknowledgement that there is a  $\pm 1$  g per 100 g uncertainty associated with the composition, the data collected is evidence that there has been no significant amount of fats entrained into the absorbent pad, whether this is the total fats or the more important FFA content. The FFA content is arguably more important than the total fat content as EPA and DHA are part of this FFA content.

In summary, prior to the addition of the absorbent pad, the thermal center of the macerate was located slightly below the center at 5 mm above the bottom of the macerate. After the addition of the absorbent pad to the bottom of the macerate the thermal center dropped to the bottom of the tray, essentially showing that the addition of the absorbent pad insulated the bottom of the macerate. This insulative effect was quantified and would increase the time taken for the bottom of the macerate to start freezing by 67%. The mathematical model was checked against the empirical data collected as well as through solving the balanced flux equation.

The absorbent pad was able to immobilize, on average, 584 g of fluid. This equates to about 19% of the total mass on top of the absorbent pad and a mass flow rate of  $66.92 \text{ kg h}^{-1}$  of water being removed. The compositional analysis of the absorbent pad was found through testing of the macerate. Due to binding issues of the water and the ability to break down the backbone that was holding the immobilized fluid. There was no substantial change in the macerate composition when comparing the portion of the tray that had the absorbent pad and the portion of the tray that had no absorbent pad.

Removal of the absorbent pad itself was difficult and time consuming relative to the time spent in the tunnel freezer. The time taken to remove the absorbent should be regarded as a source of error in the testing method as the macerate was not completely frozen after traversing the tunnel freezer. Therefore, while the absorbent pad was being removed from the macerate there is the very real possibility that this gave extra time for absorption of fluid into the absorbent pad. These and other factors that may have influenced the results of these tests are discussed in further detail in the following chapter.

## Chapter 6 Discussion

The pre and post homogenization solutions both supplied surprising solutions in terms of the fluid removal as well as with respect to the constraints. The post-homogenization method was far more efficient at removing water ( $66.92 \text{ kg h}^{-1}$ ) compared to that of the pre-homogenization solution ( $14.06 \text{ kg h}^{-1}$ ). Even though the water removal rate for the pre-homogenization solution was just an estimate based on the surface water available and an estimated removal efficiency (75%). Even with an estimated removal efficiency of 100% the water removal rate for the pre-homogenization ( $18.75 \text{ kg h}^{-1}$ ) method is still significantly less than that of the post-homogenization method.

Comparatively, the pre-homogenization solution is significantly easier to implement and operate than the post-homogenization solution. The issues with the post-homogenization solution is that the application and removal of the absorbent pad would need to be automated in order to fit in with the current process. If the process is manually carried out, there would need to be a fulltime employee for both the application and removal of the absorbent sheet, which would mitigate the cost benefits that come with the addition of the absorbent pads. The addition of a centrifuge type design would fit almost seamlessly into the process as it currently stands. There would need to be a level of automation implemented to have the process running smoothly, but the engineering and logic behind it would be relatively simply compared to the automation needed for the absorbent pad solution. The reason the automation for the absorbent pad removal would be so difficult is because the pad gets frozen to the macerate, making it difficult to delineate where the pad starts, and the macerate stops. Whereas a set of centrifuges could be set up in parallel so that there is a continuous feed to the downstream equipment.

### 6.1 Pre-Homogenization Results

The pre-homogenization solution was remarkably interesting to solve from a mathematical and physical perspective. The importance of weak points within manufacturing methods was made apparent when the static pressure vessel cracked. There were also many different iterations of the mathematical model from differing perspectives and the only method that gave a non-imaginary solution was the momentum balance starting point.

#### 6.1.1 Static Pressure Vessel Testing

There were only a handful of experiments run on the static pressure vessel, which made it difficult to collect collaborating results. There were many influential factors that were not initially thought of such as the size of the mussels which had significant impacts on the bed dynamics. With hindsight it can be seen that the size of the mussels changes the porosity of the bed, cross-sectional area of the flow channels, and possibly the number of pores. It is not certain if the varying mussel size also has an impact on the rigidity of the bed as a whole.

One of the most influential factors when running the equipment was the surges in the water supply. Due to budget constraints the static pressure vessel was connected to the factory water supply. The factory water supply supplied inconsistent pressures during the day but was more consistent during the early morning (5 am – 7am). This period of inconsistency correlated with the time at which the freeze-dryers were being unloaded in the factory, which makes sense because the water supply is used when defrosting

the freeze-dryers. This provided a small window of opportunity for experimentation at reasonable consistent supply pressures. On the day of structural failure within the static pressure vessel there was a large surge in the feed supply that ruptured the vessel wall. It is not clear what caused the surge but it is thought that the factory switches to mains pressure when the on-site water tanks empty changing the factory water pressure from 120 kPa to 500 kPa (Rinnai, 2016) within a matter of seconds.

It would have been better to take more measurements from the static pressure vessel, although after the 6<sup>th</sup> run on the vessel there was a pressure spike that caused catastrophic structural failure in the vessel wall. The pressure vessel was designed for a maximum pressure of 300 kPa. It is thought that the structural failure was due to the way that the vessel was fabricated (rolled from a single sheet and then glued together). This may have caused some structural weaknesses that were not accounted for in the design calculations. This notion was reinforced by the fact that the failure occurred along the glued edge and not the in the middle of the acrylic sheet.

The log-log plot of the lumped drag coefficient term ( $C'_D$ ) against linear velocity (Figure 29) has a similar trend to the laminar flow region of a moody diagram (Figure 30). Even though a moody plot is generally used for calculating the flow regimes through pipes of varying surface roughness's, it can still be compared analogously with the static bed experiments.

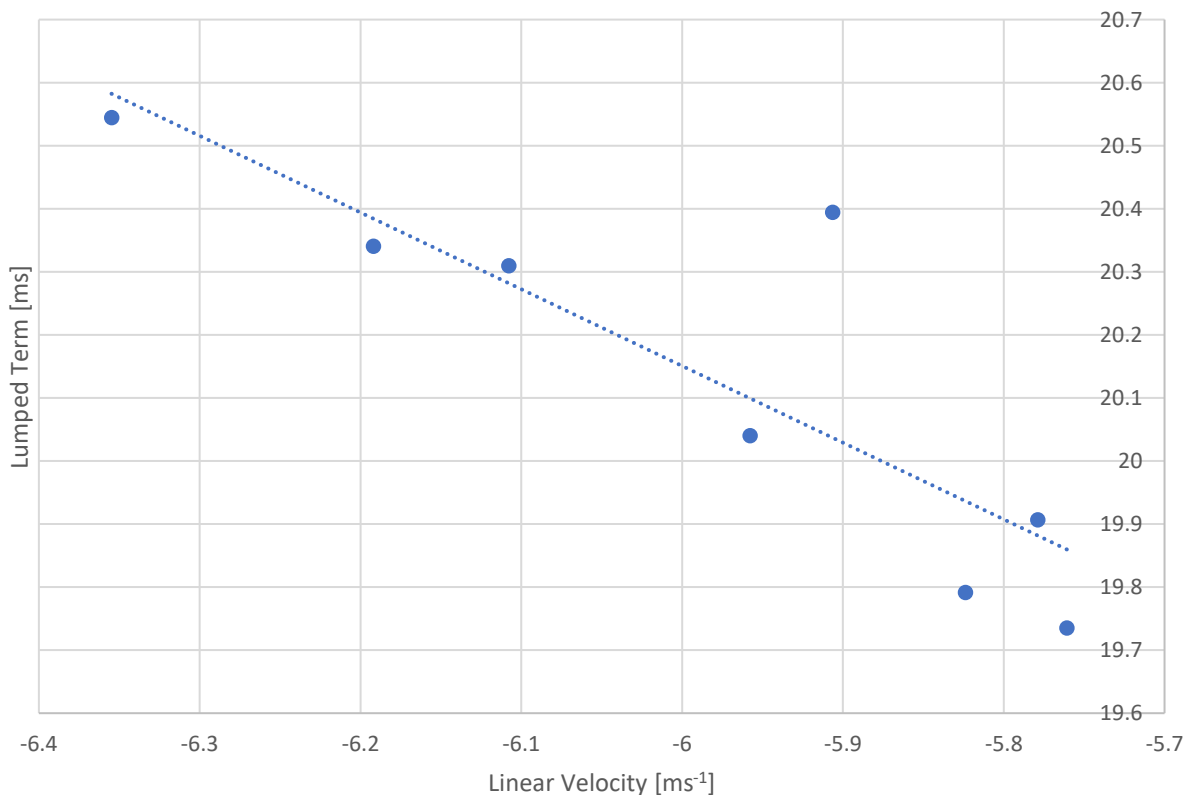


Figure 29 Log-log Lumped Drag Term Correlation

The static bed can be considered as a tube full of smaller tubes, where each of the tubes share (on average) a similar diameter, fluid velocity, and length. Mathematically speaking, the Darcy friction factor is also

inversely proportional to the Reynolds number ( $f_{Laminar} = \frac{64}{Re}$ ) in the laminar flow region. Where the Reynolds number is proportional to fluid speed ( $Re = \frac{\rho v L}{\mu}$ ). This ultimately makes the Darcy friction factor inversely proportional to the fluid velocity where  $f \propto v^{-1}$ , which is the same trend seen in the static bed experiments (Figure 29). As the lumped drag term plot increases in velocity the trend deviates from linearity which would indicate that the system is transitioning from a laminar to a turbulent flow type regime.

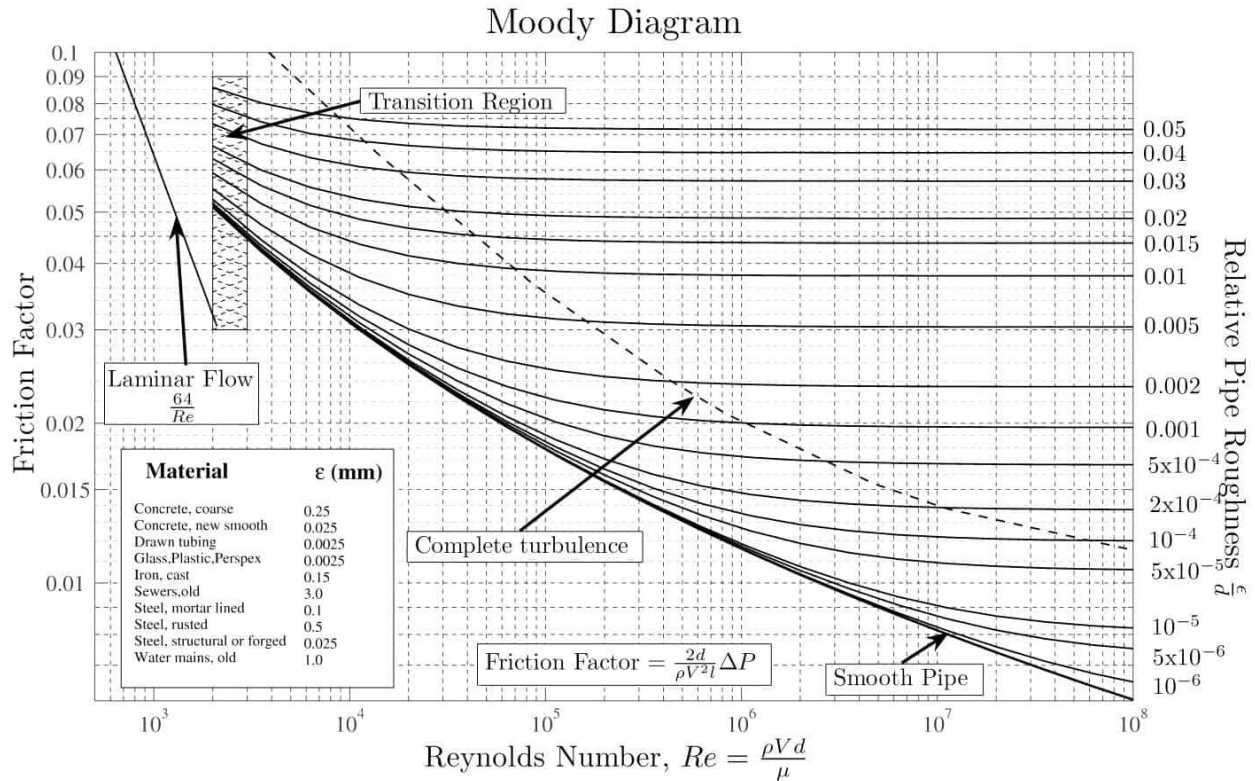


Figure 30 Moody Diagram (/su\_accordion, 2020)

Since the lumped drag coefficient term ( $C'_D$ ) mimics the trend of the Darcy friction factor gives some confidence to the validity of the experimentation methods used.

### 6.1.2 Centrifugal Solutions

When comparing the wet bed and the dry bed scenarios it was initially thought there would be a large discrepancy between the two plots (Figure 18 and Figure 20) due to the added drag force to the equation. This was not the case, as it turned out, the buoyancy factor that was incorporated into the centrifugal term as the apparent density lowered the centrifugal force impact proportionally to what was added by the drag force, effectively nullifying the impact of the drag term.

Even though the centrifugal design section doesn't provide any information on how much water this centrifuge could remove from the surface of the mussel it allows for an extension of this research where someone can build the proposed centrifuge and see how well the theory fits reality. For this study, an approximation was made for the theoretical water loss in the centrifuge using the mass of mussel in the

design (15.63 kg). Considering that mussels have 10% of their mass as surface water, if the centrifuge is able to remove 75% of this fluid then the removal rate would be  $14.06 \text{ kg h}^{-1}$ . With the highest possible removal rate of  $18.75 \text{ kg h}^{-1}$  when using a removal efficiency of 100%. The theoretical maximum water removal rate does not consider the possibility of water leaching out from the inside of the cells due to the size of the applied forces.

It is unknown if the centrifuge removes any of the valuable components of the mussel and this would be a part of the aforementioned extension of this study. Other than the unknown constituents of the expelled fluid the centrifugal solution satisfies all of the constraints laid out in Section 1.4.2 .

## 6.2 Post-Homogenization Results

There were many interesting factors that affected both the empirical data and the simulations for both the current setup and with the addition of the absorbent pad. Each step, whether it was taking measurements or simulating and fitting the model to the data, had its own unique challenges and outcomes that never seemed to fit what was initially thought.

### 6.2.1 Existing Thermal Profiles

The thermal profiles of the top and bottom of the macerate can be seen to differ in terms of the shape and the sharpness. It is thought that this could be due to measuring slightly below the surface of the macerate and therefore producing a softer curve, which can be demonstrated by the modelled data. It was also suggested that the temperature probes could be failing as their designed operating temperature was  $5^\circ\text{C}$  outside of the specified range. Although, if this were the case then it would be expected that both probes would display the same trend or would display an error of some kind, such as the temperature increasing/decreasing to impossible values. Both probes, used to measure the top and bottom temperature profiles, were the same and exposed to the same operating conditions. The temperature probe malfunction theory was disproven by placing one of the probes in a polystyrene box and using both probes to measure the surface temperature of the macerate. Both probes displayed the same trends, which disproved the possibility of the temperature influencing the componentry of the probes.

Another factor that could influence this sharp curve seen at the bottom surface of the macerate, is super cooling of the liquid below the freezing point, at which point the freezing is initiated at the bottom and not the top of the macerate. The reason that the freezing is initiated instantaneously at the bottom of the macerate and not the top is due to vibrations from the plastic chains running along the tracks giving the bottom of the macerate enough energy to change state. Whereas the top of the macerate is a lot more stable and therefore goes through a slow freezing process. Although this is purely speculation on the possible causes of this particular phenomena.

There were considerable inaccuracies when measuring the depth of the probe in the macerate. Even though there was a specifically designed brace to hold the probe at the required depth and the tray was levelled using a ruler to ensure a flat surface. The most important factor that contributed to inaccuracies regarding probe depth was the state of the tray. All the stainless-steel trays in circulation have a slight concaved nature that deviates  $\pm 3 \text{ mm}$  at the apex that is located in the center of the trays. This deviation alone contributes to significant errors when measuring the depth of the probes within the macerate. This

change in concavity would also change the depth of the macerate at the measuring point by the same  $\pm 3$  mm which also adds uncertainty to the heat transfer through the macerate.

### 6.2.2 Thermodynamic Modelling

There were many difficulties when modelling the heat transfer through the macerate, the majority of these were due to the assumption that the macerate had similar thermal properties to water. This assumption was made because the macerate consists of approximately 80% water. It was initially assumed that the macerate's thermal conductivity ( $k$ ), latent heat of fusion ( $\Delta H_{fus}$ ), freezing temperature ( $F_T$ ), density ( $\rho$ ) were all similar to that of water. Using a multiplier, or correction factor, an empirical value for the thermal conductivity of the macerate was found in terms of water's thermal properties. There also could have been correction factors added to the heat capacity and latent heat of fusion to help the mathematical data match the empirical data more precisely. Through modifying the heat capacity and latent heat of fusion of the macerate, the characteristics of inflection points seen were changed at around 600 and 1400 s in Figure 23.

The code that was written to model the heat transfer through the macerate had to be written into three equation sets. These three sets were written to describe the initial cooling of the liquid macerate, freezing of the macerate that incorporated the generation term associated with the phase change, and the propagation of the frozen front within the macerate. Joining these three sets together provides three areas of discontinuities within the plots at the associated transition regions. Integrating through these transition areas can be difficult as oscillations can begin here. To reduce the chances of oscillations in the code, the step size through the distance ( $z$ ) and time ( $t$ ) needs to be sufficiently small, but not so small that it crashes the program. One of the work arounds to help join the transition areas together was the introduction of a freezing time variable and a duration array. This was designed to manage the transition of the code between the equation sets required at any particular time and position. This was achieved through a series of nested If loops within the For loops that cycled through the time and distance dimensions. First the duration array was checked to see if that particular distance value had achieved freezing temperatures if this distance had previously achieved freezing temperatures. If this distance had not yet achieved freezing temperatures, then the liquid cooling equation set is engaged. Whereas, if the freezing temperatures have been met at that depth, then the code would check to see if it had cycled through the freezing equation set the required number of times (as allocated by the freezing time variable) and would decide if the generation term was still required or if the frozen area had finished freezing and begun propagating. This is a crude way of controlling the transitional areas while reducing the chances of oscillations occurring at these areas. Although this method does not consider the mass of material that is undergoing a change of phase. Where it would be better to add another factor that calculated the heat transfer relative to the mass that was undergoing phase change. This epsilon value would also vary along the freezing boundary with heat being projected both away from the freezing area.

One factor that should be considered when deciding the accuracy of the experiments conducted is the variability in thermal properties within the macerate itself. The thermal properties of the macerate depend on the salt content and biological content of the mussels. It has been shown in some studies (Miller, Pearce, & Bettjeman, 2014) that the gender of the mussels impacts the oil content of the mussels, which means that the biological make up of mussels is dependent on male-female ratio of the raw feed. It should also be noted that the thermodynamic properties, freezing temperature, heat capacity and the

latent heat of fusion, vary with the salt content as shown by the study from Leys et al. (Leys, Losada-Perez, Glorieux, & Thoen, 2017). By not incorporating these properties as variables in the mathematical model it makes room for inaccuracies within the model. The model should have incorporated something as simple as a correction factor, similar to the ones used for the thermal conductivity of the macerate. This would have a relative change based on an initial assumed value, therefore allowing for comment and comparison to literature on similar topics.

As previously stated, there were troubles when trying to position the probes within the macerate. Which could have caused the top, empirical, data to be not as sharp as the mathematical model for the top of the macerate. The probes were tested for consistency and measuring accuracy at the operation temperature as well. Due to the nature of the process and the probes themselves, the probes tended to sink slightly in the macerate while traversing through the tunnel freezer. This sinking was attributed to the stainless-steel trays being slightly concaved in shape. Combining this concave nature with vibrations from the moving belts it was assumed that this was enough to move the probe support to the lowest point within the tray. Which would help explain why there is a softer curve seen at the top of the macerate rather than the sharp inflection point, similar to that seen on the bottom. The concaved nature of the tray has been explained in more depth in Section 6.2.1 .

The thermal center of the macerate was investigated in two ways the first of which was through matching a mathematical model to some empirical data and the second was through solving a balanced heat flux equation. Where the model needed to be matched first so that an estimate for the thermal conductivity of the macerate could be found. Using the thermal conductivity estimate found after fitting the mathematical model to the empirical data, the heat flux equation gave the same value for the thermal center as the fitted model. Having both the numerical integration and the excel solved solution come out with the same value for the thermal center, 5 mm, adds to the accuracy of the solution.

It also interesting that the thermal center of the macerate is located closer to the bottom of the macerate. As it is generally considered that conductive heat transfer is faster than convective transfer and therefore it was first thought that the thermal center would be located closer to the top of the macerate rather than the bottom. This could be influenced by the conduction of heat through the plastic rails being poor and inhibiting heat transfer enough to bring the thermal center down to the bottom of the macerate.

### 6.2.3 Empirical Absorbent Pad Thermal Profiles

When removing the absorbent pad from the macerate, the pad came off the semi-solid areas of the macerate with little to moderate effort. This process of removing the absorbent from the semi-solid areas of the macerate was made easier due to the absorbent being attached to a solid backbone that held the absorbent layer together during removal. Whereas, in frozen areas the pad removal was exceedingly difficult, with the pad and the macerate becoming a single object. These frozen areas were located around the edges of the absorbent pad. In an industrial scale application of this particular material to the macerate would require, at least, one dedicated worker to remove the absorbent pad from the bottom of the macerate before freeze drying. This worker would have to remove the macerate-absorbent-plastic mass from the tray, remove the plastic sheet and re-position it back in the tray. Then they would have to spend 10-15 minutes per tray removing the absorbent pad, assuming that they were positioned directly after the freezer and the slurry was in the optimal semi-solid condition for pad removal. At this removal

rate, a new bottleneck would be created within the system. This would also conflict with the 6<sup>th</sup> constraint laid out in Section 1.4.2 with the new bottleneck slowing down overall throughput through the plant. To achieve the required throughput with this new absorbent removal process, it would require a team of laborers even under optimal conditions. The optimal conditions for removal are defined as having the macerate in a semi-solid state across the whole tray.

Instead of removing the absorbent pad from the frozen macerate slab, it may be more practical to freeze dry the slab and absorbent as a singular piece and remove the absorbent after the drying process. Even though this initially sounds contradicting, as this study is aimed at removing water prior to the freeze-drying process, the water absorbed by the absorbent pad may not be removed during the drying process due to the bonds formed between the absorbent and the water.

There is the possibility that there was extra absorption occurring during the removal process. This could invalidate the mass gain stated in Chapter 5. It would take 10-15 minutes to remove the absorbent pad from the macerate, which is equivalent to 22-33% increase in absorption time compared to the retention time of the tunnel freezer. The combination of, the time increase, and the semi-solid state of the macerate allows for the possibility of extra fluid transport between the absorbent and the macerate after traversing the tunnel freezer.

When removing the absorbent pad from the frozen portions of the macerate the absorbent would stick to the macerate, thus making separation of the absorbent and the macerate difficult. In these areas the absorbent pad had to be scraped off the macerate with a sharp tool. There was extra care taken around these particular areas to remove any frozen portions of the macerate from the absorbent because the absorbent would turn translucent once absorption started occurring. This translucent color change of the absorbent made the extra attention to detail needed as it would be easy to miss parts of macerate if care were not taken in this step. If the addition of the absorbent pad was chosen to be taken to industrial scale with the same pads used in this study, then the operators actively removing the pad would have to take great care not to leave any absorbent on the macerate. This would be a hazard that would have a relatively large probability of occurring and should be considered as a possible scenario in a HAZOP.

There was an uncertainty, of  $\pm 1$  g per 100 g, associated with the consistency of the macerate's composition, which has been attributed to inadequate mixing within the system. This uncertainty could be minimized by implementing a mixing tank that contains an agitator specifically designed for mixing medium-high viscosity liquids.

### 6.2.1 Mass Change of the Absorbent Pad

The mass change of the absorbent pad  $584 \pm 5$  g represents a significant change in mass (10%) and contained little of the valuable content. The results from Cawthron showed that there was a difference of 0.1% in the oil content between the control and absorbent treated macerate. The crux of this method is the application and removal of the absorbent layer.

### 6.2.2 Absorbent Pad Thermal Modelling

As previously stated, in Chapter 5, the thermal conductivity correction factor for the liquid macerate was halved whereas the thermal conductivity correction factor for the frozen macerate increased by a factor

of 5. It can be seen in the texts by Caldwell (Caldwell, 1973) and Sharqway (Sharqawy, 2012) that an increasing salt concentration in a salt-water solution decreases the thermal conductivity of the mixture. Increasing the salt content of a salt-water solution also changes other thermal properties, such as the heat capacity and the latent heat of fusion (Kousksou, Jamil, & Zeraoui, 2012). The possible changes in these two particular thermal properties, latent heat of fusion and heat capacity, were not mathematically considered in the modeling process. This could be a possible explanation for the softening of the inflection point seen in the empirical data for the bottom of the macerate (Figure 27). It is thought that there was also a decrease in both the heat capacity and the latent heat of fusion for the macerate and this decrease in these particular thermal properties caused the aforementioned softening of the inflection point. Although it should be noted that this perspective was taken from the standing of a binary salt-water system. Whereas the system at hand was composed of various organic molecules as well as salt and water. It is unknown how the organic molecules effected the thermal properties of the mixture. Although from the data acquired, and through comparison with literature on binary salt-water systems, it is thought that the addition of the organic molecules embellishes the decreasing trend for the thermal properties of salt-water systems. This is to say the decreases in thermal properties due to increasing salt concentration was far smaller than that of the 50% decrease seen in this study.

Other than the inflection point, the mathematical model fit the empirical data very well considering that the possible changes in the heat capacity, time taken to freeze the macerate and latent heat of fusion were not incorporated into the model.

One of the ways that the model differed from reality is that the thermal heat conductivity of the absorbent pad was modeled as a constant. Whereas, in reality the absorbent pad is taking on water and therefore would have a varying thermal conductivity. The thermal conductivity of the absorbent pad would be expected to get closer to that of water as it became saturated. The saturation of the absorbent pad would also dynamically change the thickness of the absorbent pad and the macerate. Even though the change may be limited to one or two millimeters, this is a relatively large change given the scale of the system.

## Chapter 7 Conclusions and Recommendations

### 7.1 Summary

As an overview of the investigated solutions, the absorbent pad option is more difficult to implement, contains a lower level of savings assuming that two fulltime employees would be needed to apply/remove the absorbent pads, but otherwise fits within the constraints and provides a greater water removal rate ( $66.92 \text{ kg h}^{-1}$ ) than the centrifugal solution. Whereas the centrifugal solution would be easier to implement but has a significantly lower water removal rate ( $14.06 \text{ kg h}^{-1}$ ). No comment can be made on the oil content of the centrifuge extracted fluid because there was no centrifugation conducted and therefore no extract produced.

There are many avenues for further research on all the topics touched on in this report. With possible investigations into:

- Construction and testing of the proposed centrifugation unit so that the estimated water removal and extracted water contents can be verified.
- Designing the control systems for the installation of the set of centrifuges or the implementation of the absorbent pad application and removal, if an automated approach was approved.
- The cost of implementation, on an industrial scale, for both solutions. This would need to include the cost of the control systems as well as raw material use analysis and disposal analysis.

These areas of investigation would build on top of what has been done in this report but there are also many areas of improvement that could be made in this report to make it more robust. Some of these areas would include:

- More experiments run on a static pressure vessel like setup using only grade D mussels.
- More experimentation into the how the bed dynamics change over varying mussel sizes.
- Building and testing the proposed centrifuge and verification of the estimated water removal rate. When the proposed centrifuge is built the water removed should also be analyzed for fatty acid content.
- More research into different types of absorbent materials to find out if there is a pad type that will have the same water removal rate but has easier application and removal properties.

### 7.2 Pre-Homogenization

The pre-homogenization solution, or the centrifugation solution, did not remove as much water as the post-homogenization method, only  $14.06 \text{ kg h}^{-1}$ . This water removal rate is based on the known surface water levels on the mussels and an estimated removal efficiency.

For this concept to be taken to an industrial scale, the effect of the differing sizes of mussels would need to be thoroughly investigated. A very specific size of mussels, grade D, was chosen for the static bed experiments due to experimental consistency. A series of experiments into the different grades of mussels (A through D) would need to be conducted to gain an understanding into how the size of the mussels affects the flow of water through the bed as well as the maximum force that can be applied to the bed before the pores close. In addition to the varying grades of mussels, there are producers that provide an ungraded product. Ungraded product is a mixed combination of all the grades (A through D) so it is

assumed that the ungraded water flow rate and maximum allowable force will lie between the results for the A grade and D grade product. Although the heterogeneous nature of the ungraded mussels could invoke more turbid flow patterns in the bed and the hypothesis that the ungraded mussels can be defined as being confined between the grade A and grade D, results would need to be confirmed.

To be able to design a centrifuge, the size and the speed of the centrifuge needed to be defined. The size of the centrifuge mostly impacted the flowrate through the centrifuge whereas, the speed of rotation affected the force that is applied to the mussels. It was hypothesized that the water would flow through the pores between the mussels up until the applied pressure went above a critical value. At this critical value, the pores between the mussels would begin to close because of the compressible nature of the mussels. The centrifugal equations could not be solved directly because of the lumped drag coefficient term ( $C'_D$ ). To gain a correlation between the applied pressure and the fluid velocity through the bed a simplistic approach was taken. The static beds experiments allowed for the correlation to be drawn and, in turn allowed for a solution to the momentum balance equations (Section 3.1 ) that were being used to describe the centrifugal system. Once the balance equations were in a position where they could be solved, the centrifuge parameters could be investigated relative to the force applied to the mussels. It was essential that the applied force did not start to restrict water movement through the bed. This critical force was found to be 12.7 kN and was calculated from the results of the static bed experiments. The throughput per centrifuge was not a major concern when designing the centrifuge as a number of the units can be used in parallel to achieve the desired throughput. A basket weight of 15.63 kg was chosen per centrifuge. At this weight, the optimum bed height was 0.58 m with an outer radius of 0.25 m. Combining these dimensions with an angular velocity of  $20 \text{ rad s}^{-1}$  meant that the applied force at the outer edges of the centrifuge, where the force is the greatest, will be equal to the critical pore closing force (12.7 kN). These should be the optimum operating conditions for a centrifuge that removes surface water from mussels of grade D size.

The critical force (12.7 kN) carries some doubt as the static bed experimental apparatus failed before a confident number of experiments could be run. All the experiments that were run over 80 kPa showed a decline or stagnation of the water velocity through the bed. Although it would be interesting to re-run the static bed experiments with a sturdier pressure vessel over a pressure range of 50 to 200 kPa in 10 kPa increments. This would help to solidify the understanding of what happens after the critical pressure (80 kPa) is met, as well as giving confidence to the aforementioned critical force (12.7 kN). It would be recommended that the static bed experiments be reconducted to assure the repeatability of the critical force as this is the basis for the centrifuge design. A complete static bed system, with its own in-line pump, would cost approximately \$15,000 and would provide a greater degree of confidence in the centrifuge design. Along with the increased confidence, this static bed apparatus could also double as a platform to investigate how the bed dynamics change with varying mussel grades. The combination of the increased confidence in the critical force (12.7 kN) and the increased understanding of the range of bed dynamics that are seen in industry means that the static bed experiments need further investigation before any large-scale capital investment is made.

The lumped drag coefficient ( $C'_D$ ) did not correlate with the Carman theory (Figure 15). This could have been because the Carman theory was designed for incompressible beds whereas, the mussels start compressing even under the smallest pressures. Another influential factor could have been the flow pattern of the water around the mussels and the size of the particulates. The Carman theory was designed for particulates in the micro range and the mussels used in this study were in the macro range.

### 7.3 Post-Homogenization

The post-homogenization method consisted of an SAP that was applied to the liquid macerate and would wick away water from the macerate while it was freezing in the tunnel freezer. The impact on the freezing of the macerate had to be quantified as well as the water removal and any impacts to the oil content of the macerate.

The thermal conductivities of the liquid and frozen macerate needed to be found as there were no literature results for the thermal conductivity of minced mussels. These two values were found by measuring the two surface temperature profiles and then fitting them to a mathematical model (Section 3.2 ). The thermal conductivities for the liquid and frozen macerate were found to be 2.312 and 0.218  $\text{W m}^{-1} \text{K}^{-1}$  respectively. The thermal conductivity of water at 10 °C is 0.578  $\text{W m}^{-1} \text{K}^{-1}$  and the thermal conductivity of ice at -5 °C is 2.18  $\text{W m}^{-1} \text{K}^{-1}$  (Toolbox, Water - Thermal Conductivity, 19). The thermal conductivity of the macerate in a liquid state is more conductive than water and once the macerate freezes it becomes less conductive than that of frozen water.

The freezing point of the macerate was  $-4.15$  °C which is lower than that of pure water. This reduction in freezing temperature is attributed to the biological content of the macerate and was expected to differ.

The superior position for the SAP positioning was found to be on the bottom of the macerate. The modeled thermal profiles through the top and the bottom of the macerate met at the thermal center (5 mm from the bottom of the macerate) which was closer to the bottom of the macerate than the top (Figure 24). This implies that the heat transfer through the top of the macerate was faster than the heat transfer through the bottom of the macerate. With this in mind it was decided that the best position of the SAP would be on the bottom of the macerate. With the SAP in this position the addition of the absorbent pad would not affect the fastest heat transfer rate and would therefore have the least impact on the freezing process. The addition of the SAP greatly inhibited the heat transfer rate through the bottom of the macerate (Figure 28). The new thermal center of the macerate, with the addition of the absorbent pad changed from 5 mm to 1 mm above the bottom of the macerate. The time to freeze the macerate changed from 1800 s to 2000 s, which is an increase of 200 s. With the absorbent pad added to the freezing process the time taken for the macerate to start freezing increased by 67%. This increase in freezing time is also associated with a 5°C increase in the exit temperature of the macerate. This combination of an increased freezing time and exit temperature would indicate that an industrial scale implementation of this absorbent pad idea would result in an increased bottleneck effect over the tunnel freezer process.

This is not the only detrimental effect seen as a result of the absorbent pad. The removal of the absorbent pad from the frozen areas of the macerate proved time consuming. Where the macerate was semi-frozen the pad was removed with relative ease, although it still requires about 5 minutes to remove a pad from a completely semi-solid tray. The boundary where the SAP ended, and the macerate started became blurred as the SAP took on the color of the SAP and the fact the macerate was frozen to the SAP made the separation complicated. Not having clean removal of the SAP from the macerate also poses a quality issue where some of the SAP could be left on the macerate through the drying process. Having any other contaminants in the macerate would be considered unacceptable. Trying to remove an SAP from every

frozen macerate slab would take a team of people which is another significant point of failure for this method.

The attributes of the absorbent pad should not be readily dismissed as this study has also found that *Sirane's Dri-Fresh* product range has the capacity to remove 20% of the water from the macerate. This 20% water removal from the absorbent pad could be used in another area of the process that also allows for easy removal from the product. The aforementioned issues of the SAP-macerate separation and the effect on the freezing time could possibly be overcome through the use of a different type of SAP or use of an SAP in another area of the process.

It is also important that the SAP does not contain oil post-absorption. The experimental results for the composition of the macerate did not exceed the  $\pm 1$  g per 100 g uncertainty attributed to the variation in the raw feed product. This information is enough to conclude that the absorbent material does not have a measurable affinity to the valuable oil content of the macerate.

The data collected in this study would be enough to start an economic investigation into the viability of the absorbent pads, but the following issues should be considered first:

- it is highly probable that there may be residues of the SAP left in the macerate after SAP removal,
- the physical removal of the SAP is a difficult, time consuming process,
- and the addition of the SAP to the freezing process increases the freezing time of the macerate by 200 s

The type and position of SAP should be reevaluated before any economic studies are undertaken.

One should especially scrutinize the empirical data. With the macerate being composed of many individual particulates that all vary individually in biological composition. The thermal profiles seen in this study could vary depending on harvesting area, harvest time and the time between harvesting and processing. The biological composition of the mussels can vary depending on the region where the mussels were harvested from and the time of year of the harvest. Different harvesting areas have variations in available nutrients and temperatures. In addition, the time of year of the harvest is important because GSM's have been known to lose condition during spawning (Robert Stack, Personal Communication, 2018). The time between harvesting and processing could affect the salinity of the batch and therefore, impact the thermal properties and how they vary with temperature. These are just some of the variables within the process that were unrestrained but are thought to have some impact on the results of this study compared to future studies in this area.

In conclusion, the addition of the absorbent pad has the potential to remove 20% of the water content from the macerate and thus, increasing the solid content of the macerate and achieving the main aim of this study. The aim of this study also states that the additional processing methods must fall within the constraints laid out in Section 1.4.2, which is where this process falls short. The addition of the absorbent pad adversely affects the freezing of the macerate within the tunnel freezer and there is a high possibility of SAP residue remaining in the macerate due to difficulties removing the absorbent from the macerate. These two negative factors directly relate to the 6<sup>th</sup> and the 4<sup>th</sup> constraints respectively and therefore, the proposed absorbent solution fails to meet the success criteria outlined in Section 1.4.1. It is recommended that further investigation is taken towards finding an area within the process that the

absorbent pad technology can be utilized without impacting the existing plant processes or have the potential to stay with the macerate through the process.

#### 7.4 Method Comparison

The removal efficiency of 100% ( $18.75 \text{ kg h}^{-1}$ ) still provides a significantly smaller water removal rate than that of the post-homogenization solution ( $66.92 \text{ kg h}^{-1}$ ). Purely from a water removal perspective, it is recommended that the absorbent pad route be furthered. There could be a position in the processing line where the application and the removal of the absorbent pad could be easier to implement.

The post-homogenization solution, of adding an absorbent pad to the macerate to wick water away from the macerate while it is freezing, was found to remove a sizeable amount of water from the macerate during freezing despite impacts to the freezing profile of the macerate.

The results for the post-homogenization method needed to have both the thermal and mass effects of adding an absorbent pad investigated. The thermal implications of adding an absorbent sheet to the macerate are important because the addition of an absorbent layer could impede the freezing of the macerate and therefore encroach on the 6<sup>th</sup> constraint laid out in Section 1.4.2 . It was determined that the thermal profile across the macerate needed to be understood in order to know how the absorbent pad should be applied to the macerate to least impact the freezing time of the macerate. To achieve this goal the thermal profile across the macerate was measured and by fitting a mathematical model to the empirical data the thermal conductivity of the macerate could be found and used to solve the thermal equilibrium equation (Eq. 34). This then provides two methods for finding the thermal center of the macerate and therefore indicating where the absorbent pad should be placed relative to the macerate.

The effects that the absorbent pad has on the change in mass of the macerate is arguably the more important aspect of the post-homogenization experiments as the primary goal of this study is to investigate methods of water removal from GSMs. Modelling the mass transfer across the absorbent pad is substantially harder due to the temperature change across the system. It is expected that the mass transfer was inhibited by the water freezing within the pores of the absorbent pad. Therefore, the mass change was measured, rather than being modelled mathematically. The mass change of the absorbent pad was measured by weighing the pad before and after the freezing process, indicating the level of saturation within the pad. Whereas the thermal profile was measured and modelled across the macerate to ensure that the freezing of the macerate is not severely impacted by the addition of the absorbent pad.

The absorbent pad used was able to remove  $195 \text{ g}$  of water per  $\text{kg}$  of macerate which equates to about 20% mass reduction over each tray.

In terms of validity of the experimentation and results taken the post-homogenization solution, again, trumps the centrifugal solution, given that the water removal rate for the centrifugal solution is only an estimate. Whereas the absorbent pad water removal rate is an empirical parameter. This would also direct further study down the absorbent line. There is the possibility that the estimated water removal parameter used for the centrifugal solution could be less than what is seen when tested. There are two possible ways the centrifugal water removal rate would be lower than that of the absorbent pad: either the removal efficiency is greater than predicted (75%); or the applied force is great enough to start removing inter-cellular water. If the applied force is great enough to tap into the inter-cellular water, then

there is greater risk that the valuable fatty acid content could be removed along with the water. Considering that the fatty acid content, for the centrifuge solution, has not been tested, there is a very real possibility that the valuable fatty acid content could also be centrifuged out with the water. Especially if the applied forces are great enough to access the inter-cellular water.

The absorbent pad solution starts to lose momentum when it comes to implementing on an industrial scale. The initially proposed implementation of adding the absorbent sheet to the trays before the macerate is poured on to the absorbent pad, would not be applicable as the process currently stands. There would be far too much work involved in the removal of the absorbent from the frozen macerate. Since the absorbent pad that was being used was similar to a fabric mesh, the macerate would adhere to the mesh making even differentiation between the fabric and the macerate difficult.

There were initial tests using the same fabric type absorbent, where the fabric was sealed inside a plastic sleeve, but this option had a far lower absorption rate ( $26.67 \text{ g h}^{-1}$ ) than the open fabric alternative ( $778.67 \text{ g h}^{-1}$ ). Initially it was thought that there were capillary type forces prohibiting the flow of water from the macerate to the absorbent pad as the only difference between the two pads was that one was in a perforated plastic sleeve and the other wasn't. The supplier of the absorbent pad was not able to supply plastic sleeve versions of the absorbent pad that had larger perforations. This would have been a good test to indicate if capillary action was inhibiting the flow of water to the absorbent material. Seeing as the larger perforations could not be achieved, it was decided that the non-sleeved alternative would be studied.

The centrifuge solution would be far easier to implement on an industrial scale, but it would still have its own issues. The main issues that would arise from the centrifuge implementation would be working around the batch nature of the centrifuge, although this could be overcome by using a set of centrifuges that feeds the system while one is being spun.

## Chapter 8 Bibliography

- /su\_accordion. (2020, 03 09). *Fanning Friction Factor*. Retrieved from <https://www.nuclear-power.net/https://www.nuclear-power.net/nuclear-engineering/fluid-dynamics/major-head-loss-friction-loss/fanning-friction-factor/>
- Aquaculture New Zealand. (2010). *New Zealand Aquaculture Farm Facts*. Retrieved from <https://www.parliament.nz/https://www.parliament.nz/resource/0000149427>
- Armengol, J., Calbo, J., Pujol, T., & Roura, P. (2008). *Bernouli Correction to Viscous Losses. Radial Flow Between Two Parallel Discs*. Spain: American Journal Of Physics.
- B, & Chu, T. (1959). *Physics of Fluids*.
- Bacia, K., Schwille, P., & Kurzchalia, T. (2005). *Sterol Structure Determines the Separation of Phases and the Curvature of the Liquid-Ordered Phase in Model Membranes*. US National Library of Medicine.
- Barriuso, B., Astiasaran, I., & Ansorena, D. (2015). *Unsaturated Lipid Matricies Protect Plant Sterols from Degradation During Heating Treatment*. Journal of Food Chemistry.
- Bird, R., Stewart, W., & Lightfoot, E. (n.d.). *Transport Phenomena*. Madison: University of Wisconsin.
- Breil, C., Vian, M. A., Zemb, T., Kunz, W., & Chemat, F. (2017). *"Bligh and Dyer" and Folch Methods for Solid-Liquid-Liquid Extraction of Lipids from Microorganisms. Comprehension of Solvation Mechanisms and towards Substitution with Alternative Solvents*. Avignon: Internation Journal of Molecular Sciences .
- Caldwell, D. (1973). *Thermal conductivity of seawater*. Deep-Sea Research.
- Cameron, S., Nikora, V., & Marusic, I. (2019). *Drag forces on a bed particle in open-channel flow: effects of pressure spatial fluctuations and very-large-scale motions*. Melbourne: Journal of Fluid Mechanics.
- Carman, P. (1956). *Flow of Gases Through Porous Media*. London: Butterworths Scientific Publications.
- Choe, E., & Min, D. (2006). *Mechanisms and Factors for Edible Oil Oxidation*. Comprehensive Reviews in Food Science and Food Safety.
- Cuddon. (2018, 11 30). *FD1000 Freeze Drier*. Retrieved from <https://www.cuddonfreezedry.com/https://www.cuddonfreezedry.com/products/fd1000-freeze-dryer/>
- Dyson. (2018). *Dyson Airblade V*. Dyson.
- Echarte, M., Zulet, M., & Astlasaran, I. (2001). *Oxidation Process Affecting Fatty Acids and Cholesterol in Fried and Roasted Salmon*. Journal of Food Chemistry.
- Fat. (2017). Retrieved from <http://know-facts.com/http://know-facts.com/about-fat.html>
- Gao, Y. (2011). *Simple Theoretical Model for Ion Cooperativity in Aqueous Solutions of Simple Organic Salts and Its Effect on Water Surface Tension*. The Journal of Physical Chemistry.

- Groot, C., Velikov, K., & Bakker, H. (2016). *Structure and Dynamics of Water Molecules Confined in Triglyceride Oils*. Royal Society of Chemistry.
- Hara, T., Kashihara, D., Ichimura, A., Tsujimoto, G., & Hirasawa, A. (2014). *Role of free fatty acid receptors in the regulation of energy metabolism*. *Biochimica et Biophysica Acta*.
- Hermann Esterbauer, G. J., Quehenberger, O., & Koller, E. (2018). *Autoxidation of human low density lipoprotein: loss generation of aldehydes of polyunsaturated fatty acids and vitamin E and*. Austria: *Journal of Lipid Research* .
- Hyperphysics. (19, 03 22). *Thermal Conductivity*. Retrieved from <http://hyperphysics.phy-astr.gsu.edu: http://hyperphysics.phy-astr.gsu.edu/hbase/Tables/thrcn.html>
- Kousksou, T., Jamil, A., & Zeraouli, Y. (2012). *Enthalpy and apparent specific heat capacity of the binary solution during the melting process: DSC modeling*. Morocco: *Thermochimica Acta*.
- Law, K.-Y. (2015). *Water–surface interactions and definitions for hydrophilicity, hydrophobicity and superhydrophobicity*. *Pure and Applied Chemistry*.
- Leys, J., Losada-Perez, P., Glorieux, C., & Thoen, J. (2017). *The melting behaviour of water and water-sodium chloride solutions being studied by high resolution Peltier-element-based adiabatic scanning calorimetry*. Budapest: Springer.
- Luke Schneider Personal Communication. (2018). *Personal Communication*.
- Luo, J., Ding, L., Wan, Y., Paullier, P., & Jaffrin, M. (2011). Fouling behavior of dairy wastewater treatment by nanofiltration under. *Separation and Purification Technology*.
- Lyprinol. (2017). *What is Lyprinol?* Retrieved from <http://www.lyprinol.com: http://www.lyprinol.com/index.php/about-lyprinol/what-is-lyprinol>
- McKetta, J., & Cunningham, W. (1992). *Fire Extinguishing Chemicals to Fluid Flow, Slurry Systems and Pipelines*. *Encyclopedia of Chemical Processing and Design*.
- Miller, M. (2014). *Oxidation of Food Grade Oils*. Nelson: Plant and Food Research.
- Miller, M. R., Pearce, L., & Bettjeman, B. (2014). *Detailed Distribution of Lipids in Greenshell™ Mussel (Perna canaliculus)*. *Nutrients*.
- Moros, J., Roth, M., Garrigues, S., & Guardia, M. D. (2009). *Preliminary Studies About Thermal Degradation of Edible Oils Through Attenuated Total Reflectance Mid-Infrared Spectrometry*. Valencia: *Food Chemistry Journal*.
- Nimbkar, N., & Rajvanshi, A. (2013). *Simple Filtration and Low Temperature Sterilization of Drinking Water*. *Current Science Journal (JSTOR)*.
- Pallu Reddanna, J. W., Burgess, J. R., Eskew, M. L., Hildenbrandt, G., Zarkower, A., Scholz, R. W., & Reddy, C. C. (1989). *The Role of Vitamin E and Selenium on Arachidonic Acid Oxidation by way of the 5-Lipoxygenase Pathway*. Pennsylvania: Department of Veterinary Science and Environmental Resources Research Institute.

Personal communication. (2018). Nelson.

PharmacyDirect. (2018, 08 8). *Lyprinol*. Retrieved from <http://www.pharmacydirect.co.nz/>:  
[http://www.pharmacydirect.co.nz/Lyprinol-Green-Lipped-Mussel/?gclid=CjwKCAjwhqXbBRAREiwAucoo-wXp4IPtvopoN7Dzb0BCJfMrJeAtW5m6mVUTIWlaKwm894tGltcCDhoCcHwQAvD\\_BwE](http://www.pharmacydirect.co.nz/Lyprinol-Green-Lipped-Mussel/?gclid=CjwKCAjwhqXbBRAREiwAucoo-wXp4IPtvopoN7Dzb0BCJfMrJeAtW5m6mVUTIWlaKwm894tGltcCDhoCcHwQAvD_BwE)

Rides, M., Morikawa, J., Halldahl, L., Hay, B., Lobo, H., Dawson, A., & Allen, C. (2009). *Polymer Testing*. NY: Elsevier Ltd.

Rinnai. (2016, September 1). *5 Reasons to Switch to Mains*. Retrieved from <https://rinnai.co.nz/>:  
<https://rinnai.co.nz/blog/3/5-reasons-to-switch-to-mains>

Robert Stack, Personal Communication. (2018).

Sharqawy, M. (2012). *New correlations for seawater and pure water thermal conductivity at different temperatures and salinities*. Saudi Arabia: Desalination.

Sigma-Aldrich. (2020). *Glycerol Safety Data Sheet*. Retrieved from <https://www.sigmaaldrich.com/>:  
<https://www.sigmaaldrich.com/MSDS/MSDS/DisplayMSDSPage.do?country=NZ&language=en&productNumber=G9012&brand=SIAL&PageToGoToURL=https%3A%2F%2Fwww.sigmaaldrich.com%2Fcatalog%2Fproduct%2Fsial%2Fg9012%3Flang%3Den>

Sirane. (2018). *Dri-Fresh*. Retrieved from <http://www.sirane.com/>: <http://www.sirane.com/dri-fresh/dri-fresh-absorbent-pads.html>

Sirane. (2020, 5 14). *Dri-Fresh Absorbent Meat Pads*. Retrieved from <https://www.sirane.com/>:  
<https://www.sirane.com/food-packaging-products/dri-fresh/dri-fresh.html>

Spargue, M., Cooper, S., Tocher, D., & Betancor, M. (2018). *Encapsulated Fish Oil Products Available in the UK Meet Regulatory Guidelines With Respect to EPA and DHAContents and Oxidative Status*. European Journal of Lipid Science and Technology.

Stickel, J. J., & Fotopoulos, A. (2001). *Pressure-Flow Relationships for Packed Beds of Compressible Chromatography Media at Laboratory and Production Scale*. Massachusetts: Biopharmaceutical Process Sciences.

Sweet, Roth, & Moss. (1987). *Thermal Conductivity of Inconel 718 and 304 Stainless Steel*. International Journal of Thermophysics.

TempRecord. (2018, 10 16). *MULTITRIP - General Multi Use*. Retrieved from <http://temprecord.com/>:  
<http://temprecord.com/wp-content/uploads/2017/11/MultiTrip-C-LR.pdf>

Toolbox, E. (19, 03 22). *Water - Thermal Conductivity*. Retrieved from [Engineeringtoolbox.com](http://www.engineeringtoolbox.com/):  
[https://www.engineeringtoolbox.com/water-liquid-gas-thermal-conductivity-temperature-pressure-d\\_2012.html](https://www.engineeringtoolbox.com/water-liquid-gas-thermal-conductivity-temperature-pressure-d_2012.html)

Toolbox, E. (2019, 08 16). *Convective Heat Transfer*. Retrieved from <https://www.engineeringtoolbox.com/>: [https://www.engineeringtoolbox.com/convective-heat-transfer-d\\_430.html](https://www.engineeringtoolbox.com/convective-heat-transfer-d_430.html)

Theo Palmer  
(67989595)

University of Canterbury  
CAPE Department

Yang, Y., & Daido, A. (1993). *Evaluation of Open Channel Flow With Varying Aspect Ratio and Roughness Ratio*. JSCE.

Zangar, C. (1953). *Theory and Problems of Water Percolation*. Denver: Engineering Monographs.

Zhang, X., Xu, Y., Cao, K., & Zhang, Q. (2015). *Structure–activity relationships of functional absorbents: Effects of Absorption Capacity, Selective and Retention Behavior*. China: Materials and Design Journal.

## Appendix

### 8.1 Static Pressure Vessel

- 8.1.1 Equipment List
- 8.1.2 Raw Data
- 8.1.3 Record Sheet Template

Table 6 Layout of the Static Bed Experimental Workbook

<b>Author:</b>	Theo Palmer							
<b>Purpose:</b>	Create a workbook that will record the data from the "Static Bed" experiments.							
<b>Constants</b>								
<b>Vessel Diameter</b>	0.45	[m]						
<b>Vessel Area</b>	0.16	[m <sup>2</sup> ]						
<b>Mass of Mussels Used:</b>								
<b>Bed Height</b>	<b>PI<sub>101</sub></b>	<b>PI<sub>102</sub></b>	<b>Pressure Drop</b>	<b>Volume Captured</b>		<b>Time</b>	<b>Flowrate</b>	<b>Fluid Velocity</b>
[m]	[kPa]	[kPa]	[kPa]	[L]	[m <sup>3</sup> ]	[s]	[m <sup>3</sup> /s]	[m/s]
			0		0		#DIV/0!	#DIV/0!
			0		0		#DIV/0!	#DIV/0!
			0		0		#DIV/0!	#DIV/0!
			0		0		#DIV/0!	#DIV/0!
			0		0		#DIV/0!	#DIV/0!
			0		0		#DIV/0!	#DIV/0!
			0		0		#DIV/0!	#DIV/0!
			0		0		#DIV/0!	#DIV/0!
			0		0		#DIV/0!	#DIV/0!
			0		0		#DIV/0!	#DIV/0!
			0		0		#DIV/0!	#DIV/0!
			0		0		#DIV/0!	#DIV/0!

#### 8.1.4 MATLAB Code Used in Centrifuge Design

```

clc
clear all
close all

dP = 90000; %Max allowable pressure [Pa]
Multi = 25; %Multiplier for the angular velocity.
omega = 10; %Angular velocity [Rad s^-1]
rho = 1100; %Mussel Density [kg/m^3]
dr = linspace(0,2); %Radial change array [m]

Pressure_Func = @(r,o) (0.5.*rho.*(o^2).*r.^2)/1000; %Function that calculates omega
m = @(r,H) rho*H*pi()*r.^2; %Mass function

hold on

```

```
for i = 1:6
    plot(dr,Pressure_Func(dr,(i*Multi))); xlabel('Radial Outside [m]'); ylabel('Pressure Drop [kPa]'); %title('Centrifugal Contribution to the Total Pressure Drop');
    legendInfo{i} = ['Omega = ' num2str((i*Multi)) ' [Rad s^-1]'];
end
% x=0:2;
% y=85;
% plot(x,y*ones(size(x)),'k--')
% x=0:2;
% y=90;
% plot(x,y*ones(size(x)),'k--')
% x=0:2;
% y=95;
% plot(x,y*ones(size(x)),'k--')
axis([0 0.25 0 120])
legend(legendInfo,'Location','NorthEastOutside')
hold off

N2 = 40;

figure (2)
hold on
for i = 1:6
    plot(dr,m(dr,(i/1000))*N2); xlabel('Radial Change [m]'); ylabel('Mussel Mass [kg]');
    %title('Mussel Mass as a Function of Radial Change');
    legendInfor{i} = ['Bed height = ' num2str((i/1000)*N2) ' [m]'];
end
x=0:2;
y=15.63;
plot(x,y*ones(size(x)),'k--')
axis([0 0.25 0 20])
legend(legendInfor,'Location','NorthEastOutside')
```

[Published with MATLAB® R2016a](#)

### 8.1.5 Code Used Centrifuge Solutions

```
%Dry Bed Model
clc
clear all
close all
%Constants
H = 0.58; %Bed height [m]
rho_m = 1100; %Mussel density [kg/m^3]
Ri = 0.01; %Inner radius [m]
x2 = 0.25;
y2 = 0:12700;

%Variables
r = linspace(0,1);
```

```
Angular_Multiplier = 3;

%Equations
F = @(r,omega) pi.*r.*H.*rho_m.*(omega.^2).*((r.^2)-(Ri.^2));
hold on
for i = 1:6
    plot(r,F(r,(i*Angular_Multiplier))); xlabel('Radial Distance fromCenter [m]'); ylabel('Force [N]');
    legendInfo{i} = ['Omega = ' num2str((i*Angular_Multiplier)) ' [Rads^-1]'];
end
x=0:1;
y=12720;%Max Force
plot(x,y*ones(size(x)), 'k--')
plot(x2*ones(size(y2)),y2, 'k--')
axis([0 0.5 1 100000])
legend(legendInfo,'Location','NorthEastOutside')
set(gca,'yscale','log')
hold off

%Wet Bed Solution

%Constants
H = 0.58; %Bed height [m]
rho_m = 1100; %Mussel density [kg/m^3]
Ri = 0.01; %Inner radius [m]
rho_w = 998; %water density [kg/m^3]
A = 2.437*10^6; %Lumped drag term coefficient
%Variables
r = linspace(0,1);

%Equations
F = @(r,omega) ((2.*pi.*r.*H.*omega.^2.*(rho_m-rho_w).*(r.^2 - Ri.^2))./2)+((2.*pi.*r.*H.*A.*rho_w.*(r.^2 - Ri.^2).*(A - (A.^2 - 4.*omega.^2).^1/2))./4);

figure(2)
hold on
for i = 1:6
    plot(r,F(r,(i*Angular_Multiplier))); xlabel('Radial Distance fromCenter [m]'); ylabel('Force [N]');
    legendInfo{i} = ['Omega = ' num2str((i*Angular_Multiplier)) ' [Rads^-1]'];
end
x=0:1;
y=12720;%Max Force [N]
plot(x,y*ones(size(x)), 'k--')
plot(x2*ones(size(y2)),y2, 'k--')
axis([0 0.5 1 100000])
legend(legendInfo,'Location','NorthEastOutside')
set(gca,'yscale','log')
hold off
```

## 8.2 Absorbent Pad

### 8.2.1 Preliminary Testing (Capillary Action Significance)

There were two different Sirane products that were trialed. The first of which was a sodium polyacrylate absorbent that was encased in a plastic sleeve that had perforations on one side of the sleeve. The second product was a similar absorbent, but the absorbent was attached to a foam like backbone in order to increase the rigidity of the material and allow for SAP-product contact.

The first product was tested for its maximum absorbency and possible applied absorbency. The maximum absorbency was tested by submerging the SAP in a bucket of water until all the SAP had contacted the water. Once the SAP contacted water it would change from an opaque white color to a clear, transparent semi-fluid. The possible applied absorbency was tested by layering the SAP onto/beneath a tray of macerated mussels. This SAP was left to sit on/below the macerate for the same duration as the residence time of the tunnel freezer (40 mins). As seen on the table below (Table 7) the SAP performed twice as well when it was positioned on the bottom of the macerate compared to when it was positioned below the macerate and there was only a 2.63% utilization of the SAP capacity.

*Table 7 Preliminary Testing Results*

<b>Test Type</b>	<b>Value</b>	<b>Units</b>
Water Removed with SAP on Bottom	20	[g]
Water Removed with SAP on Top	9	[g]
Maximum Absorbency	0.76	[kg]

### 8.2.2 Record Sheet Template

*Table 8 Absorbent Pad Record Sheet*

<b>Absorbent Pad Type:</b>			
<b>Test Number</b>	<b>Initial Weight</b>	<b>Final Weight</b>	<b>Water Gained</b>
[#]	[g]	[g]	[g]
1			0
2			0
3			0
4			0
5			0

## 8.3 Auxiliary Probe Support Designs

The first design for the temperature probe support can be seen on the figure below (Fig. 31 ). This design consisted of an angular support that would allow for 28 mm of the temperature probe to be exposed to the macerate. Due to the shape of the support there was only space for two holes, one at 5 mm above the tray and another at 11 mm above the tray. These two heights would allow for temperature measurements at the surface and in the center of the macerate. These two measurement areas would be

essential in calculating the thermal flux through the macerate, although the interface between the tray and the macerate is missing from this design. Another flaw in this design is that there is a large plate that is either acting as an insulator or conductor, depending on the construction material. Having this large area for either conduction or insulation is not ideal as another term would have to be added into the heat transfer equation to compensate for the extra material. This particular flaw was minimized by reducing the thickness of the base. Reducing the thickness of the base decreases the thermal influence that it has on the system but, it also decreases the strength of the structure. This design could be improved through reducing the bottom plate surface area. This reduction in surface area would be achieved by removing the center portion of the base of the support, thus having the sloped portion of the support sitting on two prongs instead of a plate. This would bring up concerns about the strength of the support. If the prongs were too small and made of plastic then they would break easily, rendering the support useless.

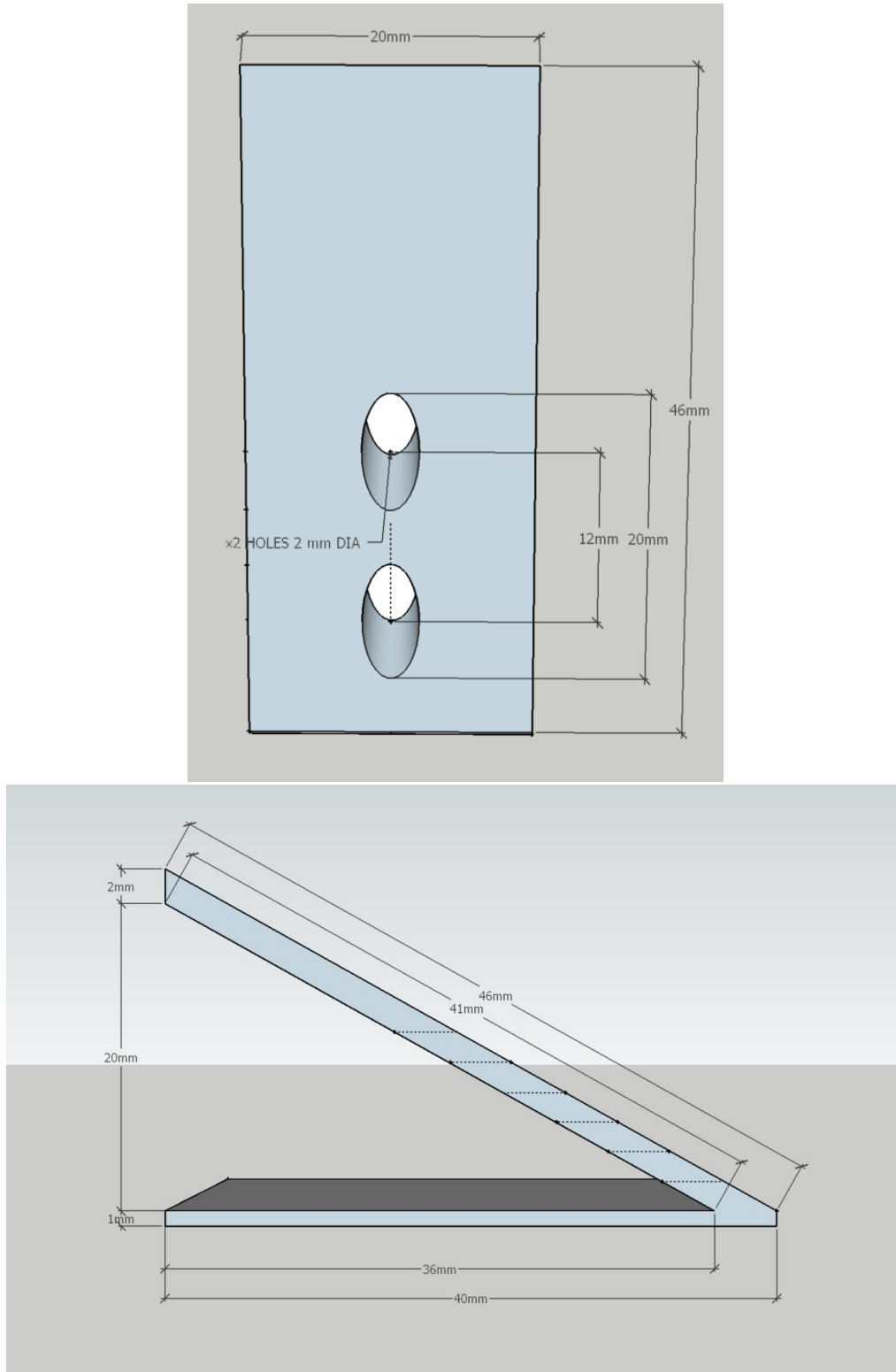


Figure 31 Auxiliary Probe Support Design #1 Side (Bottom) and Top (Top) View

The second support design consisted of two rectangular pieces of 1 mm plastic connected by two 5x5x25 mm plastic square bar as seen in the side elevation below (Fig. 32 ). This design would have been created

using a 3D printer as the machining of such small spaces would be difficult. The two plates are spaced 25 mm from each other, which will allow for the end of the probe to sit 5 mm away from the plate. The end of the probe needs to be some distance away from the plate in order to minimize any conductive heat transfer from the plate to the probe. The two front plates will have four holes drilled down the centerline of the plate. These holes were located at 0, 5, 8, and 11 mm from the bottom of the support. These holes will allow the probe to held horizontally at the heights previously stated, the significance of these particular heights are stated in the list below:

- The macerate-tray interface temperature is located at 0 mm from the bottom of the support. This interface temperature can be used to solve individual heat transfer equations. This information is useful when verifying the thermal conductivity of the stainless steel.
- The midpoint of the macerate is located at 5.5 mm from the bottom of the support and was used to verify the equilibrium point within the macerate.
- The macerate is 11 mm thick which is why the macerate-air interface is found 11 mm from the bottom of the support. This interface is important because the information found at this point is used in heat transfer equations to help verify the thermal conductivity of the macerate.

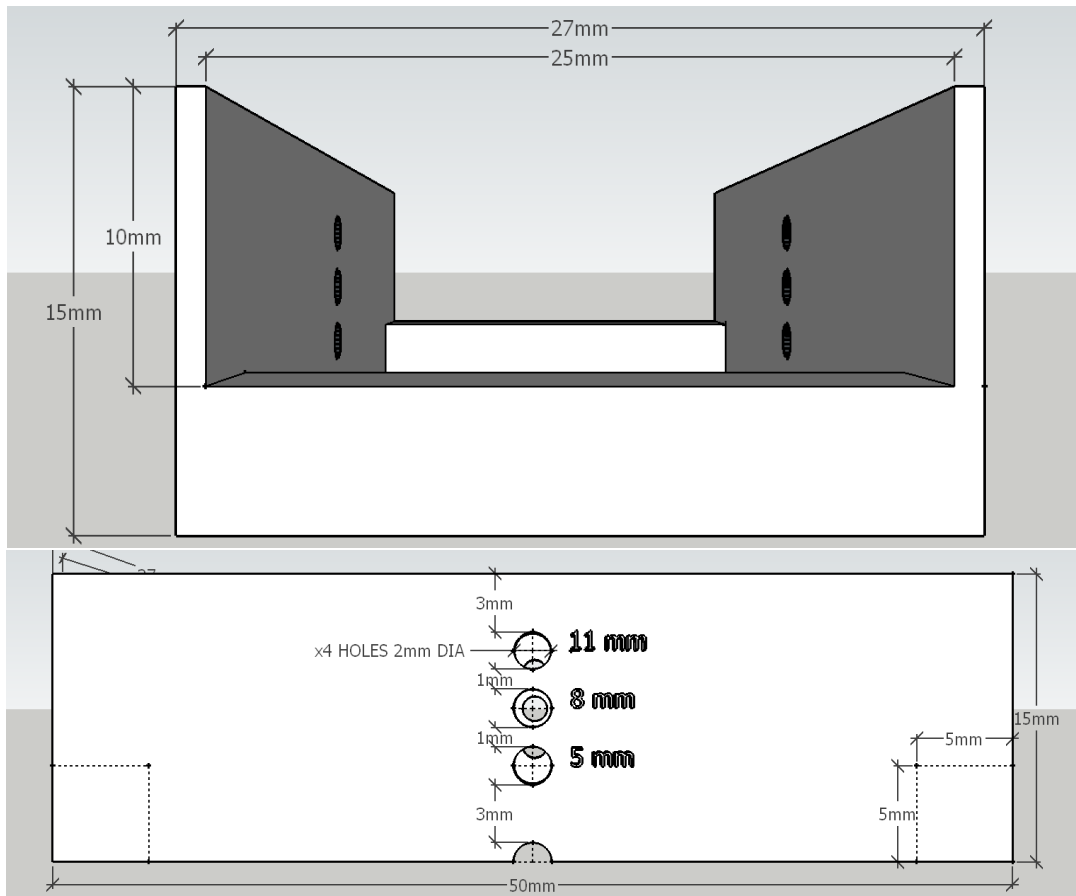


Figure 32 Front (Bottom) and Side (Top) Elevation View of Auxiliary Support #2

## 8.4 Numerical Integration Method for Current Thermodynamic Layout

### 8.4.1.1 Dimensionless Numerical Integration

$$\varphi'(\tau) = \frac{1}{Z} \varphi'(Z) + \varphi''(Z)$$

$$\varphi'_i(\tau) = \frac{1}{Z_i} \frac{\varphi(Z_{i+1}) - \varphi(Z_{i-1})}{2\Delta Z} + \frac{\varphi(Z_{i+1}) - 2\varphi(Z_i) + \varphi(Z_{i-1}))}{\Delta Z^2}$$

$$\varphi(\tau_{i+1}) = \varphi(\tau_i) + \Delta\tau \varphi'_i(\tau)$$

$$BC1: \frac{\partial T}{\partial z} = 0 \text{ at } z = 0 \text{ for all } t \therefore \frac{\partial \varphi}{\partial Z} = 0 \text{ at } Z = 0 \text{ for all } \tau$$

$$BC2: k \frac{\partial T}{\partial z} = h(T - T_{Bulk}) \text{ for all } t \text{ and all } z \therefore \frac{\partial \varphi}{\partial Z} = \left(\frac{hZ}{k}\right) \varphi \text{ for all } \tau \text{ and } Z$$

$$IC: T_{Mac} = 14^\circ\text{C for all } z @ t = 0 \therefore \varphi = 1 \text{ at } \tau = 0 \text{ for all } Z$$

### 8.4.2 MATLAB Code Used to Solve Current Dimensioned Numerical Integration

```
%Dimensioned Top Numerical Solution

clc
clear all

%Variables
Correction_Const = 0.1; %Correction Const. for the frozen product
Correction_Const2 = 4; %Correction constant for the liquid product
Freezing_Point = -4.15+273.15; %Freezing point of the macerate [K] ;-3.25 works well
Freeze_Time = 2; %Number of iterations taken for the ice to form

%Constants:
t_step = 1*10^-2; %Time step [s]
t_max = 2500; %Max time value [s]
time_steps = int64(t_max/t_step); %Num of time steps needed
Dist_step = 1*10^-3; %Distance step [m]
Dist_max = 12*10^-3; %Max distance is 12 mm (1*10^-3 m)
Dist_steps = int64(Dist_max/Dist_step); %Number of steps required
z_max = 0.012; %Max achievable z distance [m]
v = 3; %Tunnel wind velocity [m/s]
h = (10.45-v+10*(v^0.5)); %Convective heat transport - wind velocity relation [W/m^2K]
k = (0.578*Correction_Const2); %Thermal conductivity of the liquid macerate
k_ice = (2.18*Correction_Const); %Thermal conductivity of the frozen macerate (Assumed to be
equal to waters)
INV_R_Liquid = 1/k;
INV_R_Ice = 1/k_ice;
INV_R_T = 1/INV_R_Liquid;
INV_R_T2 = 1/INV_R_Ice;
k_T = 1/INV_R_T;
k_T2 = 1/INV_R_T2;
```

```

k=k_T;
k_ice=k_T2;
rho_ice = 917; %Density of ice [kg/m^3]
H_fus = 334*10^3; %notEnthalpy of fusion [J/kg]
rho = 999; %Density of water [kg/m^3]
C_p = 4.18*10^3; %Heat Capacity of water [J/kgK]
C_p_ice = 2.108*10^3; %Heat Capacity of ice [J/kgK]
T_max = 14+273.15; %Max temperature [K]
T_Bulk = -25+273.15; %Min temperature [K]
Gen = ((H_fus)/(C_p)); %Heat generation term
TFT = 2*10^-5; %Estimate for the theoretical film thickness
C = 12;

% Dimmensionless Array's
t_Array = zeros(1,time_steps); %Empty time array
T_Array = zeros(Dist_steps,time_steps); %Empty temperature array
dT_dt = zeros(Dist_steps,time_steps); %Empty temperature derivative array
Dist_Array = zeros(Dist_steps,2); %Empty distance array
P_Array = zeros(12,4); %Empty array that stores distance and time of frozen front propogation

for i = 2:time_steps
    t_Array(1,i) = t_Array(1,i-1)+t_step; %For loop that makes sure that
    %the t_Array contains the correct values
end
for i = 2:Dist_steps
    Dist_Array(i,1) = Dist_Array(i-1,1)+Dist_step;
end

for t = 1:time_steps
    if t == 1
        %For the first iteration I want to set T_o to the IC
        for z = 1:Dist_steps
            T_Array(z,t) = T_max; %Initial Condition (T = T_max for all z)
        end

        %After I have set all the T, I can then calculate the dT/dt
        for z = 1:Dist_steps
            if z == 1 %Start of matrix Z=0
                dT_dt(z,t) = (k/(rho*C_p))*((2*T_Array(z+2,t)-2*...
                    T_Array(z+1,t)+T_Array(z,t))/(Dist_step^2));
            elseif z == Dist_steps %End of matrix Z=1
                dT_dt(z,t) = -(h/k)*(T_Array(z,t)-T_Bulk)*(TFT); %Boundary Condition
            else
                dT_dt(z,t) = (k/(rho*C_p))*((T_Array(z+1,t)-(2*...
                    T_Array(z,t))+T_Array(z-1,t))/Dist_step^2);
            end
        end
    else
        %For the iterations after t=1 (time zero) we can calculate the new
        %temperature from the derivative (dT/dt).
        for z = 1:Dist_steps
            T_Array(z,t) = T_Array(z,t-1)+t_step*dT_dt(z,t-1);
            %Should read: T(i-1)+(\Delta t)*dT/dt(@t-1). CHECKED
        end
    end
end

```

```

for z = 1:Dist_steps
    if Dist_Array(z,2)==0
        if T_Array(z,t)>Freezing_Point %Setting condition for pre-ice formation
            if z == 1
                dT_dt(z,t) = (k/(rho*C_p))*((2*T_Array(z+1,t)-2*...
                    T_Array(z,t))/(Dist_step^2));
            elseif z == Dist_steps
                dT_dt(z,t) = -(h/k)*(T_Array(z,t)-T_Bulk)*TFT; %Boundary Condition
            else
                dT_dt(z,t) = (k/(rho*C_p))*((T_Array(z+1,t)-(2*...
                    T_Array(z,t))+T_Array(z-1,t))/Dist_step^2);
            end
        else
            Dist_Array(z,2) = 1; %Tells user if that z value has ever
            %dropped below Freezing_Point
            if z == 1
                dT_dt(z,t) = (k/(rho*C_p))*((2*T_Array(z+1,t)-2*...
                    T_Array(z,t))/(Dist_step^2))+Gen;
            elseif z == Dist_steps
                dT_dt(z,t) = -(h/(k))*(T_Array(z,t)-T_Bulk)*TFT+Gen; %Boundary Condition
            else
                dT_dt(z,t) = (k/(rho*C_p))*((T_Array(z+1,t)-(2*...
                    T_Array(z,t))+T_Array(z-1,t))/Dist_step^2)+Gen;
            end
        end
    elseif Dist_Array(z,2)<Freeze_Time
        if z == 1
            dT_dt(z,t) = (k/(rho*C_p))*((2*T_Array(z+1,t)-2*...
                T_Array(z,t))/(Dist_step^2))+Gen;
        elseif z == Dist_steps
            dT_dt(z,t) = -(h/(k))*(T_Array(z,t)-T_Bulk)*TFT+Gen; %Boundary Condition
        else
            dT_dt(z,t) = (k/(rho*C_p))*((T_Array(z+1,t)-(2*...
                T_Array(z,t))+T_Array(z-1,t))/Dist_step^2)+Gen;
        end
        Dist_Array(z,2) = Dist_Array(z,2)+1; %Changing the Switch value to 2 after 2nd
        "freezing" iteration
    else
        %This area is to house the freezing front propogation
        if z == 1
            dT_dt(z,t) = (k_ice/(rho_ice*(C_p_ice)))*((2*T_Array(z+1,t)-2*...
                T_Array(z,t))/(Dist_step^2));
        elseif z == Dist_steps
            dT_dt(z,t) = -(h/(k_ice))*(T_Array(z,t)-T_Bulk)*TFT; %Boundary Condition
        else
            dT_dt(z,t) = (k_ice/(rho_ice*(C_p_ice)))*((T_Array(z+1,t)-(2*...
                T_Array(z,t))+T_Array(z-1,t))/Dist_step^2);
        end
        if Dist_Array(z,2)<=2
            P_Array(z,1)=z;
            P_Array(C,2)=t*10^-2;
            C=C-1;
        end
        Dist_Array(z,2) = Dist_Array(z,2)+1;
    end
end

```

```
end  
end  
end  
end
```

```
figure (1)  
surf(T_Array);title("Top Simulation")  
colormap(jet);grid on  
shading interp  
ylabel("Distance [m]");zlabel("Temperature [K]");xlabel("Time [s*10^-2]");  
Book2 = readtable('Book2.csv','HeaderLines',3);
```

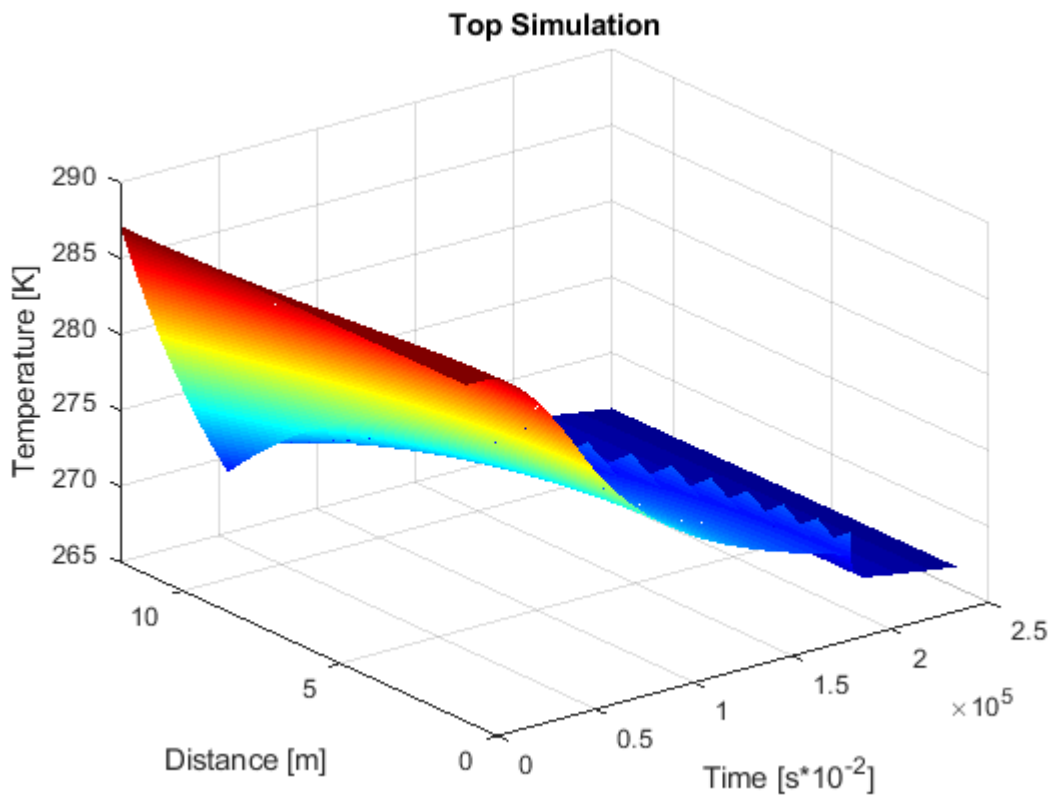


Figure 33 Mathematical Simulation of the Top of the Macerate

```
%Dimensioned Bottom Numerical Solution  
hold all  
  
%Constants:  
t_step2 = 1*10^-2; %Time step [s]  
t_max2 = 2500; %Max time value [s]  
time_steps2 = int64(t_max2/t_step2); %Num of time steps needed  
Dist_step2 = 1*10^-3; %Distance step [m]  
Dist_max = 12*10^-3; %Max distance 6is 12 mm (1*10^-3 m)  
Dist_steps2 = int64(Dist_max/Dist_step2); %Number of steps required
```

```

L_SS = 1.5*10^-3; %Thickness of SS tray [m]
k_SS = 13; %Thermal conductivity of Stainless Steel [W/mk]
L_P = 25*10^-3; %Thickness of the plastic [m]
k_P = 0.2; %Thermal conductivity of the plastic [W/mk]
Alpha = 0.05; %Proportionality constant (area of SS covered by the plastic belt) [%]
k = 0.578*Correction_Const2; %Thermal conductivity of the liquid macerate
k_ice = 2.18*Correction_Const; %Thermal conductivity of the frozen macerate (Assumed to be equal
to waters)

INV_R_Mac = 1/k;
INV_R_Mac2 = 1/k_ice;
INV_R_SS = L_SS/k_SS;
INV_R_P = Alpha*(L_P/k_P);
INV_R_Total = 1/(INV_R_Mac+INV_R_SS+INV_R_P); %The inverse of the total resistance = sum of all
inverted TC (Thermal Conductivities
INV_R_Total2 = 1/(INV_R_Mac2+INV_R_SS+INV_R_P);
k_Total = 1/INV_R_Total; %The overall thermal conductivity is equal to the inverse of the total
resistivity (Liquid)
k_Total2 = 1/INV_R_Total2;
Gen2 = Gen; %Heat generation term
C=1;
z_Comp=12;

% Dimensionless Array's
t_Array2 = zeros(1,time_steps2); %Empty time array
T_Array2 = zeros(Dist_steps2,time_steps2); %Empty temperature array
dT_dt2 = zeros(Dist_steps2,time_steps2); %Empty temperature derivative array
Dist_Array2 = zeros(Dist_steps2,2); %Empty distance array
T_Array_SIM2 = zeros(Dist_steps2,time_steps2);

for i = 2:time_steps2
    t_Array2(1,i) = t_Array2(1,i-1)+t_step2; %For loop that makes sure that
    %the t_Array contains the correct values
end
for i = 2:Dist_steps2
    Dist_Array2(i,1) = Dist_Array2(i-1,1)+Dist_step2;
end

for t = 1:time_steps2
    if t == 1
        %For the first iteration I want to set T_o to the IC
        for z = 1:Dist_steps2
            T_Array2(z,t) = T_max; %Initial Condition (T = T_max for all z)
        end

        %After I have set all the T, I can then calculate the dT/dt
        for z = 1:Dist_steps2
            if z == 1 %Start of matrix Z=0
                dT_dt2(z,t) = (k_Total/(rho*C_p))*((2*T_Array2(z+2,t)-2*...
                    T_Array2(z+1,t)+T_Array2(z,t))/(Dist_step2^2));
            elseif z == Dist_steps2 %End of matrix Z=1
                dT_dt2(z,t) = -(((1-Alpha)*h)/k_Total)*(T_Array2(z,t)-T_Bulk)*(TFT); %Boundary
            Condition
        else

```

```

        dT_dt2(z,t) = (k_Total/(rho*C_p))*((T_Array2(z+1,t)-(2*...
            T_Array2(z,t))+T_Array2(z-1,t))/Dist_step2^2);
    end
end
else
    %For the iterations after t=1 (time zero) we can calculate the new
    %temperature from the derivative (dT/dt).
    for z = 1:Dist_steps2
        T_Array2(z,t) = T_Array2(z,t-1)+t_step2*dT_dt2(z,t-1);
        %Should read: T(i-1)+(\Delta)t*dT/dt(@t-1). CHECKED
    end
    for z = 1:Dist_steps2
        if Dist_Array2(z,2)==0
            if T_Array2(z,t)>Freezing_Point %Setting condition for pre-ice formation
                if z == 1
                    dT_dt2(z,t) = (k_Total/(rho*C_p))*((2*T_Array2(z+1,t)-2*...
                        T_Array2(z,t))/(Dist_step2^2));
                elseif z == Dist_steps2
                    dT_dt2(z,t) = -(((1-Alpha)*h)/k_Total)*(T_Array2(z,t)-T_Bulk)*(TFT);
                %Boundary Condition
            else
                dT_dt2(z,t) = (k_Total/(rho*C_p))*((T_Array2(z+1,t)-(2*...
                    T_Array2(z,t))+T_Array2(z-1,t))/Dist_step2^2);
            end
        else
            Dist_Array2(z,2) = 1; %Tells user if that z value has ever
            %dropped below Freezing_Point
            if z == 1
                dT_dt2(z,t) = (k_Total/(rho*C_p))*((2*T_Array2(z+1,t)-2*...
                    T_Array2(z,t))/(Dist_step2^2))+Gen2;
            elseif z == Dist_steps2
                dT_dt2(z,t) = -(((1-Alpha)*h)/(k_Total))*(T_Array2(z,t)-T_Bulk)*TFT+Gen2;
            %Boundary Condition
        else
            dT_dt2(z,t) = (k_Total/(rho*C_p))*((T_Array2(z+1,t)-(2*...
                T_Array2(z,t))+T_Array2(z-1,t))/Dist_step2^2)+Gen2;
        end
    end
    elseif Dist_Array2(z,2)<Freeze_Time
        if z == 1
            dT_dt2(z,t) = (k_Total/(rho*C_p))*((2*T_Array2(z+1,t)-2*...
                T_Array2(z,t))/(Dist_step2^2))+Gen2;
        elseif z == Dist_steps2
            dT_dt2(z,t) = -(((1-Alpha)*h)/(k_Total))*(T_Array2(z,t)-T_Bulk)*TFT+Gen2;
        %Boundary Condition
    else
        dT_dt2(z,t) = (k_Total/(rho*C_p))*((T_Array2(z+1,t)-(2*...
            T_Array2(z,t))+T_Array2(z-1,t))/Dist_step2^2)+Gen2;
    end
    Dist_Array2(z,2)=Dist_Array2(z,2)+1; %Changing the switch value to 2 initiating
the new cycle
else
    %This area is to house the freezing front propogation
    if z == 1

```

```

        dT_dt2(z,t) =(k_Total2/(rho*(C_p_ice)))*((2*T_Array2(z+1,t)-2*...
            T_Array2(z,t))/(Dist_step2^2));
    elseif z == Dist_steps2
        dT_dt2(z,t) = -(((1-Alpha)*h)/(k_Total2))*(T_Array2(z,t)-T_Bulk)*TFT;
%Boundary Condition
    else
        dT_dt2(z,t) = (k_Total2/(rho*(C_p_ice)))*((T_Array2(z+1,t)-(2*...
            T_Array2(z,t))+T_Array2(z-1,t))/Dist_step2^2);
    end
    if Dist_Array2(z,2)<=2
        z_Comp=z_Comp-1;
        P_Array(z,3)=z_Comp;
        P_Array(C,4)=t*10^-2;
        C=C+1;
    end
    Dist_Array2(z,2) = Dist_Array2(z,2)+1;
end
end
end
end

%Array Conversion
%T_Array2 needs to be flipped about the z axis so that the relative terms
%are the same.
for t=1:time_steps2
    z1=12;
    for z=1:12
        T_Array_SIM2(z,t) = T_Array2(z1,t);
        z1=z1-1;
    end
end

figure(2)
surf(T_Array_SIM2);title("Bottom Simulation")
colormap(jet);grid on
shading interp
ylabel("Distance [m]");zlabel("Temperature [K]");xlabel("Time [s*10^-2]");

Diff_Array = T_Array_SIM2-T_Array; %Difference array that shows where the intersection points are
figure(3)
surf(Diff_Array);title("Temperature Differential Array")
colormap(jet);grid on
shading interp
ylabel("Distance [m]");zlabel("Temperature Difference [K]");xlabel("Time [s*10^-2]");
figure(4)
contour(Diff_Array,30); xlabel("Time [s*10^-2]");ylabel("Distance [mm]")

figure (5)
hold on; grid on; grid minor
plot (Book2{:,4},Book2{:,1},'b')
plot (Book2{:,4},Book2{:,2},'r')
plot (t_Array(1,:),T_Array(11,:),'m') %Denotes the first script (TOP SIM)
plot (t_Array2(1,:),T_Array_SIM2(2,:),'c') %Denotes the second script (Bottom SIM)
legend("Average Top Experimental Data","Average Bottom Experimental Data",...

```

```
"Mathematical Top Data",...  
"Mathematical Bottom Data")  
xlabel ("Time [s]"); ylabel ("Temperature [^{\circ}C]"); hold off  
  
figure (6)  
plot(P_Array(6:12,2),P_Array(6:12,1),P_Array(1:7,4),P_Array(1:7,3));  
grid on  
grid minor  
xlabel("Time [s]");ylabel("Distance [mm]");  
legend("Freezing Front Propagation (TOP)","Freezing Front Propagation (BOT)");
```

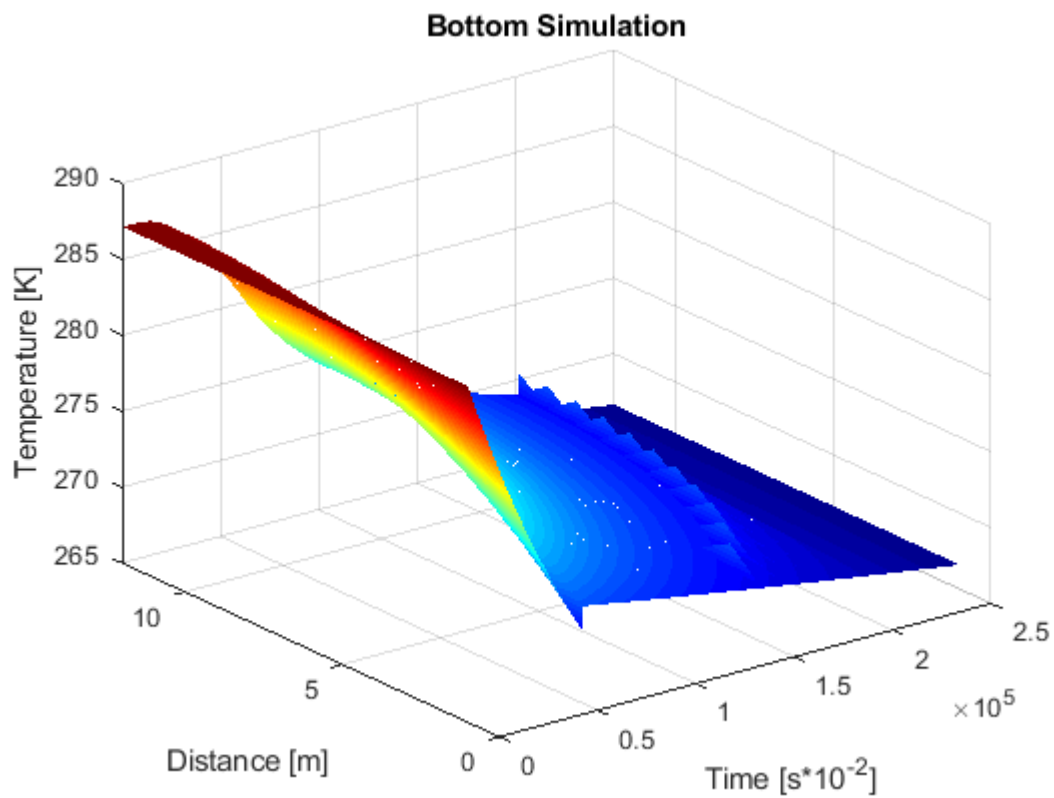


Figure 34 Mathematical Simulation of the Bottom of the Macerate

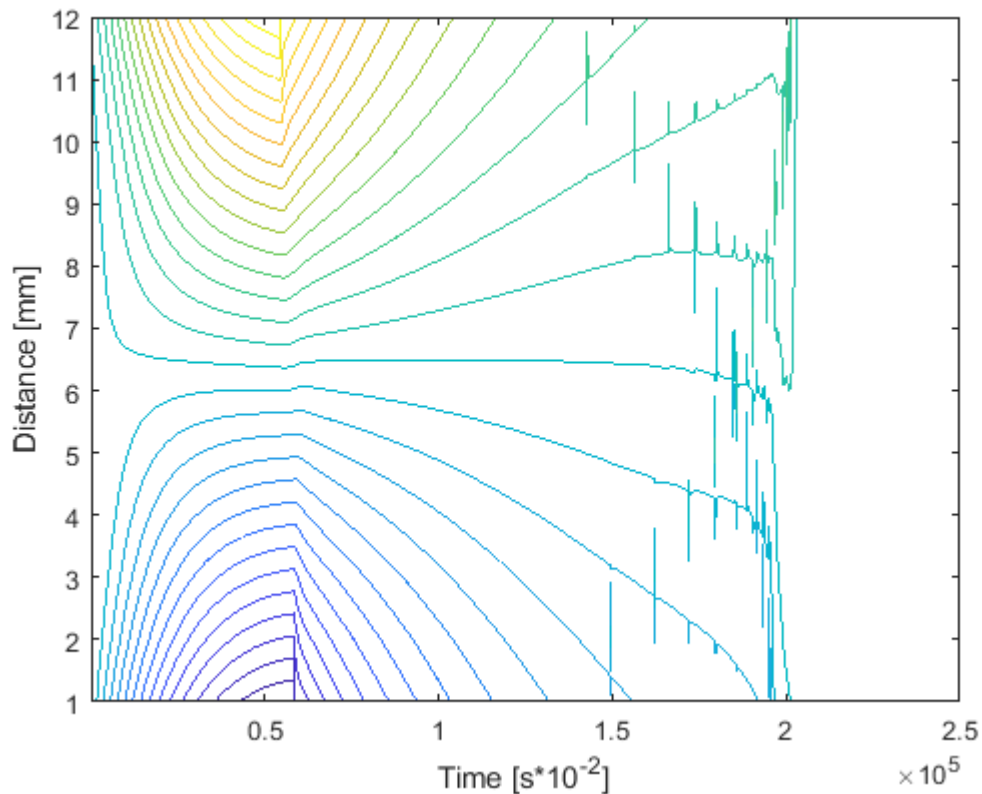


Figure 35 Difference Array of the Two Simulations

Figure 36 Contour Map of the Differential Array

[Published with MATLAB® R2018b](#)

### 8.4.3 MATLAB Code Used to Solve Padded Dimensioned Numerical Integration

```
%Dimensioned Padded Bottom Numerical Solution
hold all

Correction_Const = 0.05; %Correction Const. for the frozen product
Correction_Const2 = 2; %Correction constant for the liquid product
Freeze_Time = 2;

%Constants:
t_step2 = 1*10^-2; %Time step [s]
t_max2 = 2500; %Max time value [s]
time_steps2 = int64(t_max2/t_step2); %Num of time steps needed
Dist_step2 = 1*10^-3; %Distance step [m]
Dist_max = 12*10^-3; %Max distance is 12 mm (1*10^-3 m)
Dist_steps2 = int64(Dist_max/Dist_step2); %Number of steps required
L_SS = 1.5*10^-3; %Thickness of SS tray [m]
```

```

k_SS = 13; %Thermal conductivity of Stainless Steel [w/mk]
L_P = 25*10^-3; %Thickness of the plastic [m]
k_P = 0.2; %Thermal conductivity of the plastic [w/mk]
Alpha = 0.05; %Proportionality constant (area of SS covered by the plastic belt) [%]
L_ABS = 4*10^-3; %Thickness of the absorbent pad [m]
k_ABS = 0.5; %Thermal conductivity of the absorbent pad
T_max = 9.5+273.15;
k = 0.578*Correction_Const2; %Thermal conductivity of the liquid macerate
k_ice = 2.18*Correction_Const; %Thermal conductivity of the frozen macerate (Assumed to be equal
to waters)

INV_R_Mac = 1/k;
INV_R_Mac2 = 1/k_ice;
INV_R_SS = L_SS/k_SS;
INV_R_P = Alpha*(L_P/k_P);
INV_R_ABS = L_ABS/k_ABS;
INV_R_Total = 1/(INV_R_Mac+INV_R_SS+INV_R_P+INV_R_ABS); %The inverse of the total resistance =
sum of all inverted TC (Thermal Conductivities
INV_R_Total2 = 1/(INV_R_Mac2+INV_R_SS+INV_R_P+INV_R_ABS);
k_Total = 1/INV_R_Total; %The overall thermal conductivity is equal to the inverse of the total
resistivity (Liquid)
k_Total2 = 1/INV_R_Total2;
Gen2 = Gen; %Heat generation term
C=1;
z_Comp=12;

% Dimmensionless Array's
t_Array2 = zeros(1,time_steps2); %Empty time array
T_Array2 = zeros(Dist_steps2,time_steps2); %Empty temperature array
dT_dt2 = zeros(Dist_steps2,time_steps2); %Empty temperature derivative array
Dist_Array2 = zeros(Dist_steps2,2); %Empty distance array
T_Array_SIM2 = zeros(Dist_steps2,time_steps2);

for i = 2:time_steps2
    t_Array2(1,i) = t_Array2(1,i-1)+t_step2; %For loop that makes sure that
    %the t_Array contains the correct values
end
for i = 2:Dist_steps2
    Dist_Array2(i,1) = Dist_Array2(i-1,1)+Dist_step2;
end

for t = 1:time_steps2
    if t == 1
        %For the first iteration I want to set T_o to the IC
        for z = 1:Dist_steps2
            T_Array2(z,t) = T_max; %Initial Condition (T = T_max for all z)
        end

        %After I have set all the T, I can then calculate the dT/dt
        for z = 1:Dist_steps2
            if z == 1 %Start of matrix Z=0
                dT_dt2(z,t) =(k_Total/(rho*C_p))*((2*T_Array2(z+2,t)-2*...
                    T_Array2(z+1,t)+T_Array2(z,t))/(Dist_step2^2));
            elseif z == Dist_steps2 %End of matrix Z=1

```

```

        dT_dt2(z,t) = -(((1-Alpha)*h)/k_Total)*(T_Array2(z,t)-T_Bulk)*(TFT); %Boundary
Condition
    else
        dT_dt2(z,t) = (k_Total/(rho*C_p))*((T_Array2(z+1,t)-(2*...
            T_Array2(z,t))+T_Array2(z-1,t))/Dist_step2^2);
    end
end
else
    %For the iterations after t=1 (time zero) we can calculate the new
    %temperature from the derivative (dT/dt).
    for z = 1:Dist_steps2
        T_Array2(z,t) = T_Array2(z,t-1)+t_step2*dT_dt2(z,t-1);
        %Should read: T(i-1)+(\Delta)t*dT/dt(@t-1). CHECKED
    end
    for z = 1:Dist_steps2
        if Dist_Array2(z,2)==0
            if T_Array2(z,t)>Freezing_Point %Setting condition for pre-ice formation
                if z == 1
                    dT_dt2(z,t) =(k_Total/(rho*C_p))*((2*T_Array2(z+1,t)-2*...
                        T_Array2(z,t))/(Dist_step2^2));
                elseif z == Dist_steps2
                    dT_dt2(z,t) = -(((1-Alpha)*h)/k_Total)*(T_Array2(z,t)-T_Bulk)*(TFT);
%Boundary Condition
                else
                    dT_dt2(z,t) = (k_Total/(rho*C_p))*((T_Array2(z+1,t)-(2*...
                        T_Array2(z,t))+T_Array2(z-1,t))/Dist_step2^2);
                end
            else
                Dist_Array2(z,2) = 1; %Tells user if that z value has ever
                %dropped below Freezing_Point
                if z == 1
                    dT_dt2(z,t) =(k_Total/(rho*C_p))*((2*T_Array2(z+1,t)-2*...
                        T_Array2(z,t))/(Dist_step2^2))+Gen2;
                elseif z == Dist_steps2
                    dT_dt2(z,t) = -(((1-Alpha)*h)/(k_Total))*(T_Array2(z,t)-T_Bulk)*TFT+Gen2;
%Boundary Condition
                else
                    dT_dt2(z,t) = (k_Total/(rho*C_p))*((T_Array2(z+1,t)-(2*...
                        T_Array2(z,t))+T_Array2(z-1,t))/Dist_step2^2)+Gen2;
                end
            end
        elseif Dist_Array2(z,2)<Freeze_Time
            if z == 1
                dT_dt2(z,t) =(k_Total/(rho*C_p))*((2*T_Array2(z+1,t)-2*...
                    T_Array2(z,t))/(Dist_step2^2))+Gen2;
            elseif z == Dist_steps2
                dT_dt2(z,t) = -(((1-Alpha)*h)/(k_Total))*(T_Array2(z,t)-T_Bulk)*TFT+Gen2;
%Boundary Condition
            else
                dT_dt2(z,t) = (k_Total/(rho*C_p))*((T_Array2(z+1,t)-(2*...
                    T_Array2(z,t))+T_Array2(z-1,t))/Dist_step2^2)+Gen2;
            end
        end
        Dist_Array2(z,2)=Dist_Array2(z,2)+1; %Changing the switch value to 2 initiating
the new cycle

```

```

else
    %This area is to house the freezing front propogation
    if z == 1
        dT_dt2(z,t) =(k_Total2/(rho*(C_p_ice)))*((2*T_Array2(z+1,t)-2*...
            T_Array2(z,t))/(Dist_step2^2));
    elseif z == Dist_steps2
        dT_dt2(z,t) = -(((1-Alpha)*h)/(k_Total2))*(T_Array2(z,t)-T_Bulk)*TFT;
%Boundary Condition
    else
        dT_dt2(z,t) = (k_Total2/(rho*(C_p_ice)))*((T_Array2(z+1,t)-(2*...
            T_Array2(z,t))+T_Array2(z-1,t))/Dist_step2^2);
    end
    if Dist_Array2(z,2)<=Freeze_Time
        z_Comp=z_Comp-1;
        P_Array(z,3)=z_Comp;
        P_Array(C,4)=t*10^-2;
        C=C+1;
    end
    Dist_Array2(z,2) = Dist_Array2(z,2)+1;
end
end
end

%Array Conversion
%T_Array2 needs to be flipped about the z axis so that the relative terms
%are the same.
for t=1:time_steps2
    z1=12;
    for z=1:12
        T_Array_SIM2(z,t) = T_Array2(z1,t);
        z1=z1-1;
    end
end
for i=1:11
    P_Array(i+1,3)=i;
    if P_Array(i,4)~=0 || P_Array(i,4)>2000
        Index=i;
    end
end
N_A=zeros(Index,2);
for i=1:Index
    N_A(i,1)=P_Array(i,3);
    N_A(i,2)=P_Array(i,4);
end
figure(2)
surf(T_Array_SIM2);title("Bottom Simulation")
colormap(jet);grid on
shading interp
ylabel("Distance [m]");zlabel("Temperature [K]");xlabel("Time [s*10^-2]");
%
Diff_Array = T_Array_SIM2-T_Array; %Difference array that shows where the intersection points are
figure(3)
surf(Diff_Array);title("Temperature Differential Array")

```

```

colormap(jet);grid on
shading interp
ylabel("Distance [m]");zlabel("Temperature Difference [K]");xlabel("Time [s*10^{\wedge}2]");
figure(4)
contour(Diff_Array,30); xlabel("Time [s*10^{\wedge}2]");ylabel("Distance [mm]")

figure (5)
hold on; grid on; grid minor
% plot (Book2{:,4},Book2{:,1},'b')
% plot (Book2{:,4},Book2{:,2},'r')
plot (Book2{:,4},Book3{:,4},'k')
% plot (t_Array(1,:),T_Array(11,:), 'm') %Denotes the first script (TOP SIM)
plot (t_Array2(1,:),T_Array_SIM2(2,:), 'c') %Denotes the second script (Bottom SIM)
legend("Bottom (w) Absorbent Pad Experimental Data","Mathematical Bottom (w) Absorbent Pad Data")
xlabel ("Time [s]") ; ylabel ("Temperature [\wedge]C");hold off

figure (6)
plot(P_Array(6:12,2),P_Array(6:12,1),N_A(1:7,2),N_A(1:7,1));
xlim([0,2000]);ylim([0,12]);
grid on
grid minor
xlabel("Time [s]");ylabel("Distance [mm]");
legend("Freezing Front Propagation (TOP)","Freezing Front Propagation (BOT)");

```

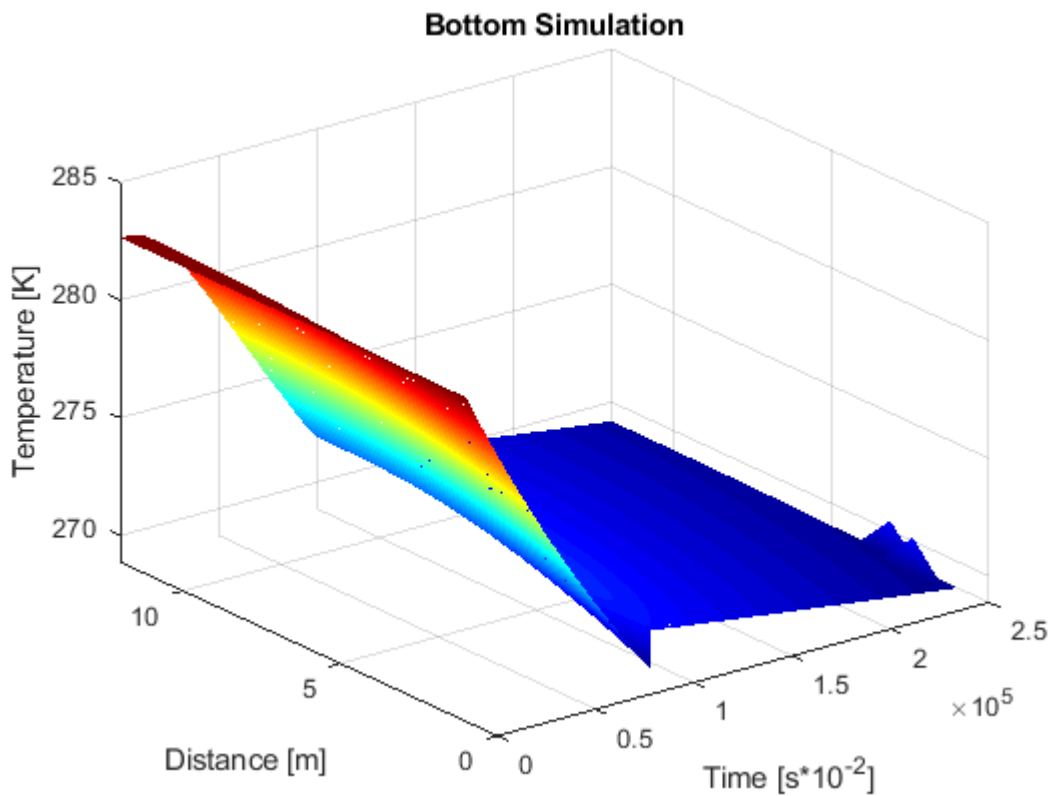


Figure 37 Bottom Temperature Profile with Absorbent Pad

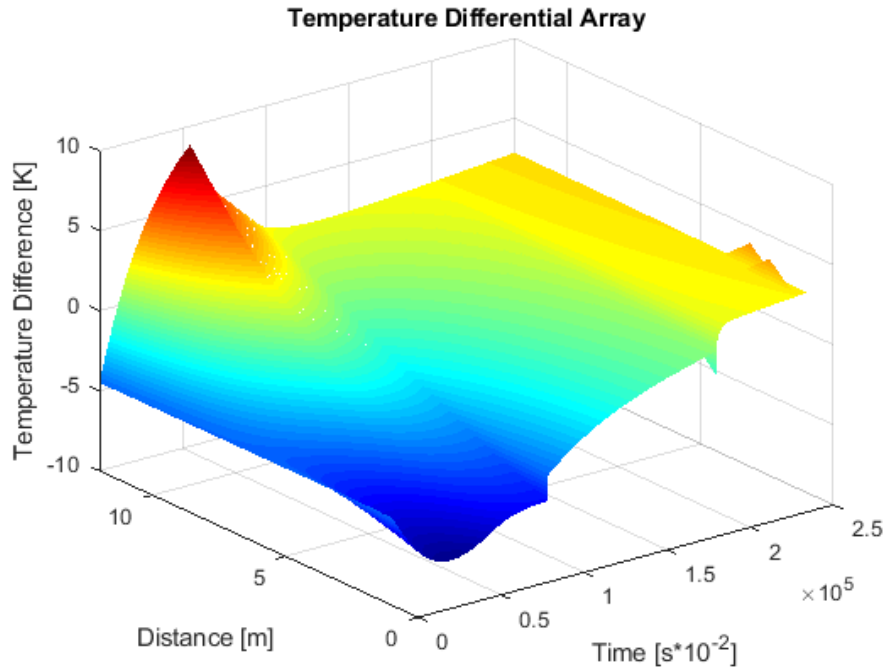


Figure 38 Temperature Differential Array with Absorbent Pad

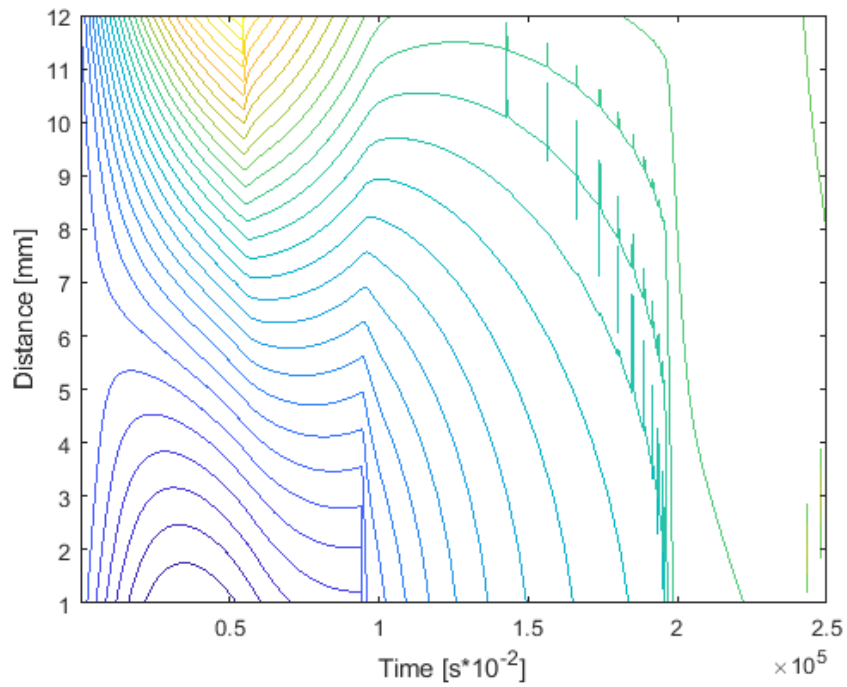


Figure 39 Contour Map of the Differential Array with Absorbent Pad

[Published with MATLAB® R2018b](#)